OPEN ACCESS

EUROPEAN MECHANICAL SCIENCE

ISSN: 2587-1110

Volume 4
Issue 2
June 2020

Editor in Chief: M. Ozcanli

EUROPEAN MECHANICAL SCIENCE

Indexed / Abstracted in:

TR-Dizin, CrossRef, Index Copernicus, Journal Factor, Rootindexing, ResearchBip, JournalFactor, JIFACTOR, Google Scholar, I2OR, Cosmos Impact Factor, International Innovative Journal Impact Factor (IIJIF), Scientific Indexing Services, InfoBase Index, Scientific Journal Impact Factor

Aims and Scopes

European Mechanical Science (EMS) is an international, peer reviewed journal which publishes full length original research papers, reviews related to all areas of Mechanical Engineering such as: Solid Mechanics, Materials Engineering, Automotive Engineering, Fluid Mechanics, Thermal Engineering, Engine and Power Engineering, Dynamics & Control, Robotics & Mechatronics, Transportation Engineering, Computational Mechanics, Design, Systems, Manufacturing, Bio-Medical Engineering; Process Engineering, Aerospace Engineering. No charges are required from the Authors to publish the articles.EMS is a quarterly published journal operating an online submission and peer review system. It allows authors to submit articles online and track their progress via its web interface.

http://dergipark.gov.tr/ems

EUROPEAN MECHANICAL SCIENCE

Contents

EUROPEAN MECHANICAL SCIENCE
e-ISSN: 2587-1110

Research Paper

Effect of Orientation Angle on Surface Quality and Dimensional Accuracy of Functional Parts Manufactured by Multi Jet Fusion Technology

Binnur Sağbaş*

Yildiz Technical University, Mechanical Engineering Department, Istanbul, Turkey

Abstract

Multi Jet Fusion is one the new Additive Manufacturing method which belongs to powder bed fusion technology class and used for additive manufacturing of polymer based parts. There are restricted number of research about this developing technology. In this study, it is aimed to investigate the effect of build orientation angle on surface quality and dimensional accuracy of the printed bolts as functional parts. Samples were manufactured in two different build orientations such as 90 and 45 degrees. Surface quality and dimensional properties of the bolt tooth such as tooth height, tooth angle and distance between two teeth were inspected by optical and tactile precision measurement systems. The results were evaluated by comparing the measurement data with each other for two different sample groups and also with nominal design data. For determining the significance of the difference between two sample groups and nominal data the results were also evaluated by Student's t-test statistical analysis. The results revealed that, orientation angle had significant effect on surface roughness, tooth height and tooth angle but it didn't affect the distance between two teeth.

Keywords: Additive Manufacturing, Multi Jet Fusion, Optical Metrology, Polyamide, Precision Metrology.

INTRODUCTION

Additive Manufacturing (AM) is a novel and rapidly developing technology that builds up physical three dimensional (3D) geometries from a computer-aided 3D model (CAD) data without any usage of molds, tools or fixtures [1]. Multi Jet Fusion (MJF) is one the new AM method which works with the principle of powder bed fusion (PBF) technology and used for polymer based AM part manufacturing [2]. It was developed by HP and commercially available since 2016 [3]. MJF system consists of two main stations such as build unit and post processing unit. In build unit 3D geometry of the part generated by fusing the polymer powder together near about material melting temperature [4]. The desired geometry is defined by the fusing and detailing agents deposited by ink print heads in precise locations. After spreading the first layer of the polymer powder over the build platform, it is heated near about sintering temperature and fusing agent deposited precisely on to the powder by inkjet nozzles in accordance with 3D geometry of manufactured part. Then detailing agent is deposited near the edge of the part for inhibiting sintering. Lastly, IR energy source passes over the powder on the build pad across a line based path and sinters the areas where the fusing agent was deposited and leaves the rest of the powder unaltered. The process repeats until all parts are completed [5] Thirty million drops per second can be printed by these print heads that provide to obtain highly accurate dimensional precision compared with other technologies [6]. The geometry is built up in powder so there is no need to support structure. After building step the cooling and unpacking of the manufactured part is applied in post processing unit. These two unit system provide continuing the manufacturing process and save time [4].

Polyamide (PA) is most widely used polymer in MJF technology so as in powder bed fusion additive manufacturing techniques [5]. According to the commercial suppliers it can take different names such as PA2200 for EOS and PA12 for HP. By combining the PA powder with glass beads, carbon nano tubes, silicon carbide, aluminum and nanofibers, mechanical properties of printed parts can be increased [7]. Beside PA12 powder, PA11 and PA12 with glass beads are also suitable for the usage in MJF technique [8].

In literature studies, there are restricted number of research about MJF and they have been generally focused on mechanical properties and surface qualities. Riedelbauch et al. [3]

* Corresponding authour
Email: bsagbas@gmail.com

European Mechanical Science (2020), 4(2): 47-52
doi: https://doi.org/10.26701/ems.678901
Received: January 2, 2020, Revised: January 25, 2020
Accepted: January 27, 2020, Published: February 15, 2020

studied about aging effects of reused PA12 powder on mechanical properties of MJF manufactured parts. The samples were manufactured in Z and Y orientations. They concluded that, thermal aging didn't affect the mechanical properties of the samples. Moreover, slightly higher mechanical properties were recorded for Z orientation than Y oriented parts. In another study, O'conor at al.[7] focused on the investigating mechanical properties of the PA samples manufactured by MJF technique in X,Y and Z orientations. They reported that the samples exhibited isotropic behavior in terms of tensile tests while the build orientations had significant effect on flexural strength. Palma et al. [9] studied about effect of print orientation on mechanical and tribological properties of MJF manufactured PA12 samples. They built up the tensile tests samples in horizontal and vertical directions and they concluded that mechanical and tribological properties of the samples depend on print orientation.

In this study, it is aimed to define effect of orientation angle on the surface quality and dimensional accuracy of the functional parts such as bolt teeth, manufactured by MJF technology. As far as the author know, there is no detail previous study that characterizing angular, dimensional, form and roughness deviation of bolt teeth manufactured by MJF method with different orientation angle. Moreover, the study provides a comparative assessment of tactile and optical precision metrology systems for inspection of additive manufactured parts. So, it is expected that this study would be a useful reference for further studies and development of AM processes.

2. MATERIALS AND METHODS

2.1 Sample Preparation

In this study bolt samples were designed by Autodesk Fusion 360 program, converted STL file format and manufactured by HP 3D Multi Jet Fusion 4200 printer. HP 3D High Reusability PA12 powder, with 60 µm particle size, 187 °C melting point, 0.425 g/cm^3 powder bulk density, 1.01 g/cm^3 print density [10]. Samples were oriented 90° perpendicularly (named as Sample-90) and 45° inclined (named as Sample-45) in Z axis, on to the build platform. The design data and layout of the print table can be seen in Figure 1.

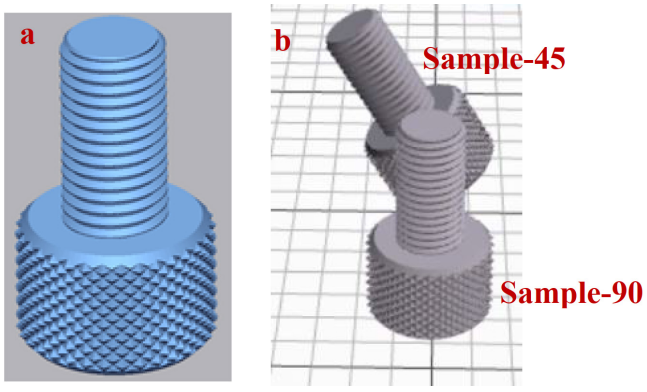

Figure 1. Design data (a) and print table layout of the samples (b)

"Balanced print mode", which provides good compromise between dimensional accuracy, mechanical properties, surface roughness and printing speed, was chosen for building up the 3D geometries [11]. All printed parts were placed with a distance of 10 mm from each other. After printing process, time is needed for cooling down of the built parts before taking them out. While the temperature reached about 45 °C, the built unit was taken to the post-processing station. Because the printed parts were encapsulated by powder, support structures were not necessary in the MJF process. So, just excessive powders were removed and then glass bead blasting were applied under 5 bars pressure. Before the surface measurements, the samples were washed in deionized water in ultrasonic bath for about 20 minutes and then dried in ambient condition.

2.2 Optical and Tactile Profile Measurements

For defining the dimensional and profile deviations of bolt teeth, Keyence VR5000 series optical scanning system was used. Dimensional measurements were taken in automatic mode with 12X magnification. Tooth angles and the distance between two teeth were defined by scanning the surface of the bolt in profile measurement mode with 40X magnification. Deviations of the heights, distance and angles of the teeth were defined by comparison of measured data with nominal CAD data as reference. 2D and 3D surface roughness values were define with precision scanning mode of the same system. At least three repeated measurements were taken from different regions of the samples and the mean values and standard deviations were calculated. The results were compared for two different build orientation and significance of the difference between the results were evaluated statistically.

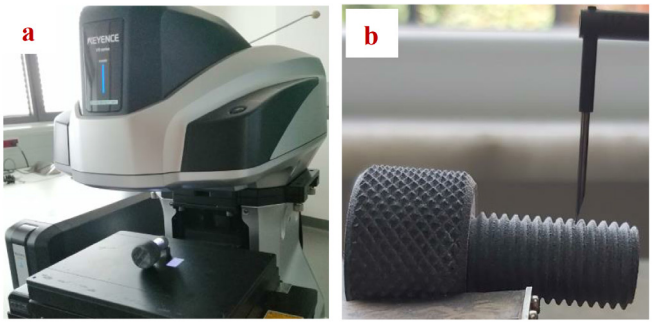

Figure 2. Optical (a) and tactile (b) measurement of the samples.

Tactile profile measurements of the samples' teeth were taken by Taylor Hobson Form Talysurf Intra. After testing different tips, chisel type tip with 1125445 code was chosen. The tip radius was 20 µm and tip angle was 15°. Measurement evaluation length was 27 mm and measurement speed was 0.25 mm/s. The used optical and tactile systems can be seen in Figure 2.

3. RESULTS AND DISCUSSION

3.1. Surface Roughness Results

Roughness measurements were taken from different regions of the bolts teeth. ISO 4287 [12] 2D line Ra, Rz and ISO

25178 [13] 3D areal Sa, Sz roughness parameters were defined. Ra and Sa represent the arithmetic mean roughness values while Rz and Sz represent the maximum height of the profile deviations such as the absolute vertical distance between the maximum profile peak height and the maximum profile valley depth along the sampling length for Rz and defined area for Sz. 2D and 3D average roughness values and standard deviations (SD) of the measurement results have been reported in Table 1.

Table 1. 2D and 3D surface roughness values of the samples.

Roughness Parameter	Sample-45		Sample-90	
	Av.Roughness (µm)	SD (µm)	Av.Roughness (µm)	SD (µm)
Ra	10.714	0.633	6.508	0.356
Rz	54.000	10.500	38.400	8.850
Sa	20.039	0.333	19.620	1.180
Sz	276.500	20.800	211.500	14.000

Roughness results were evaluated by two-sample t-test statistical analysis for determining if there was statistically significant difference between two sample groups. Test results revealed that the difference between average surface roughness, Ra, Rz and Sz values of the samples were statistically significant (p=0.002, 0.036 and 0.021 respectively) at α=0.05 confidence level while the difference between Sa parameters were not significant. The approach of the 2D and 3D roughness calculations models of surface measurement system are different. So there is no a general linear relation between 2D and 3D roughness parameters [14]. Therefore difference may occur between these two parameter groups. In overall evaluation of the roughness for both samples, all surface roughness values of the teeth on the Sample-90 were lower than Sample-45. Therefore, it can be concluded that perpendicular orientation provides better surface quality for bolt teeth. For achieving better surface quality the print part

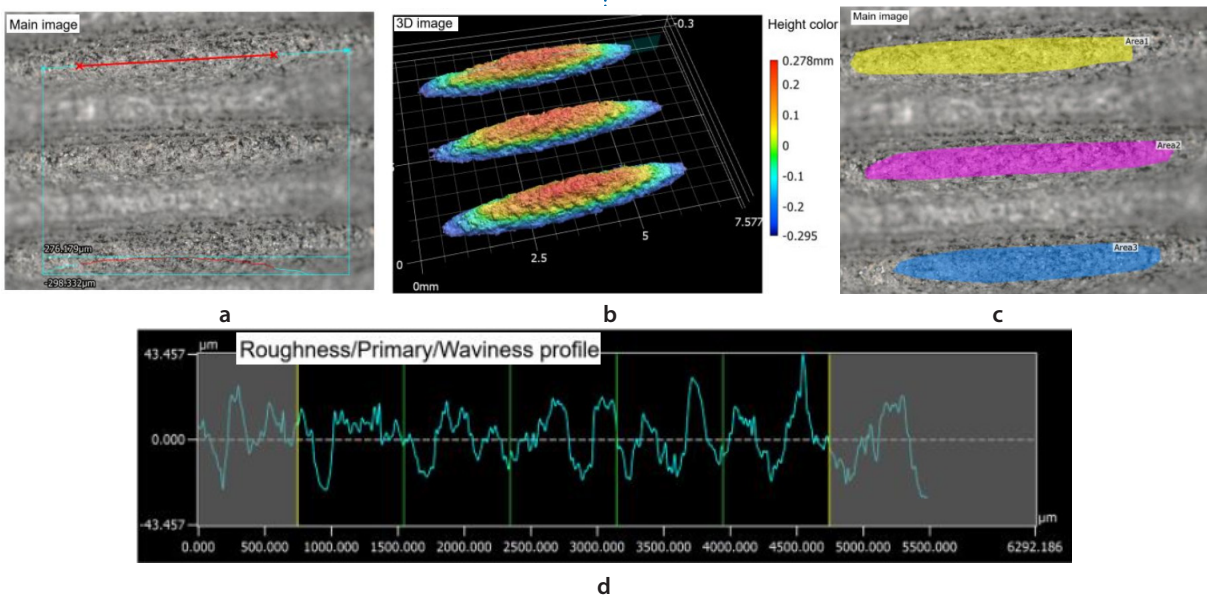

Figure 3. Measurement procedure and results for Sample-45; defining 2D lines on main scanned image of the teeth for investigating 2D roughness parameters (a), 3D areal surface roughness measurement image (b), definition of measurement area on main image of the teeth for investigating 3D roughness parameters (c), graph of the roughness, primary and waviness profile of the teeth (d).

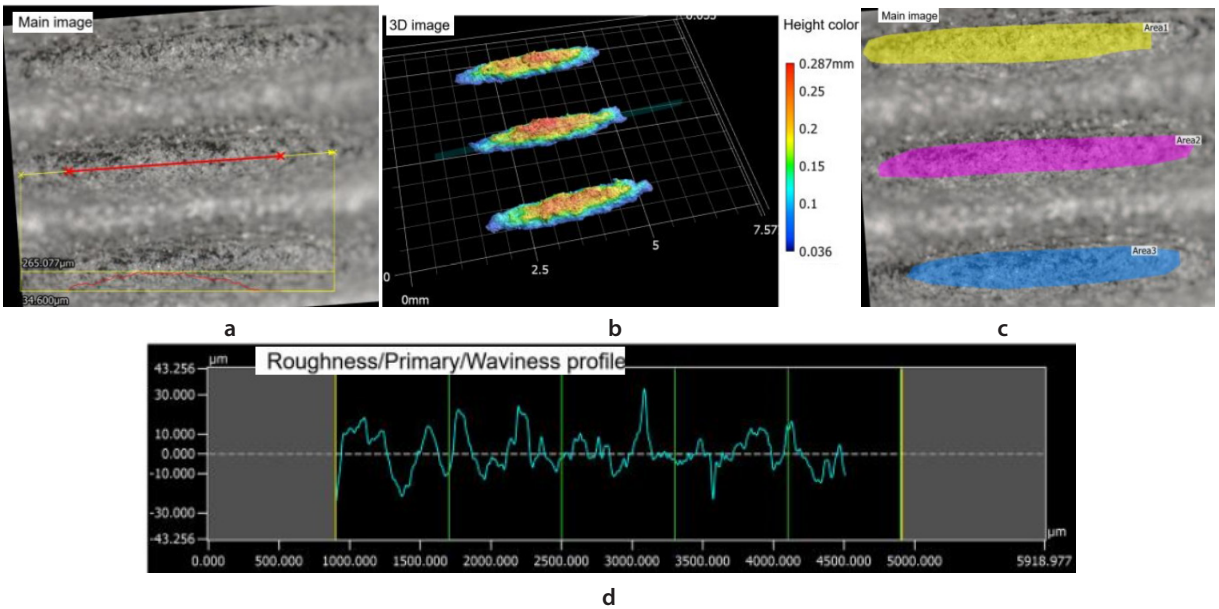

Figure 4. Measurement procedure and results for Sample-90; defining 2D lines on main scanned image of the teeth for investigating 2D roughness parameters (a), 3D areal surface roughness measurement image (b), definition of measurement area on main image of the teeth for investigating 3D roughness parameters (c), graph of the roughness, primary and waviness profile of the teeth (d).

must be placed upside down in built chamber. Moreover, for avoiding stair-stepping which was defined as the geometric step formation between the successive layers and consequently a decrease in surface quality [15], the print part should be placed more than 20 degrees to the horizontal plane [16]. While the printed bolt placed perpendicularly, the teeth positions were inclined. So, better surface quality was obtained for Sample-90 than Sample-45. Measurement procedure and results can be seen in the Figure 3 and Figure 4 for Sample-45 and Sample-90 respectively.

3.2. Dimensional Measurement Results

Dimensional properties such as height of tooth, angle of tooth and distance between two teeth were measured by tactile and optical precision metrological systems. The nominal tooth height in CAD model was 1.11 mm. Mean height value of Sample-45 teeth were recorded as 1.1083 mm while it was 1.1263 mm for Sample-90 teeth by tactile method. There was no significant difference between two samples tooth height and nominal value. Optical measurement data was compared with CAD model as reference geometry and mean deviations from the nominal height values were recorded as 0.1047 mm with SD 0.0279 mm and 0.1360 mm with SD 0.0266 mm for Sample-45 and Sample-90 respectively. Tooth height deviation of Sample-90 was higher than Sample-45. Measurement results can be seen in Figure 5 and Figure 6.

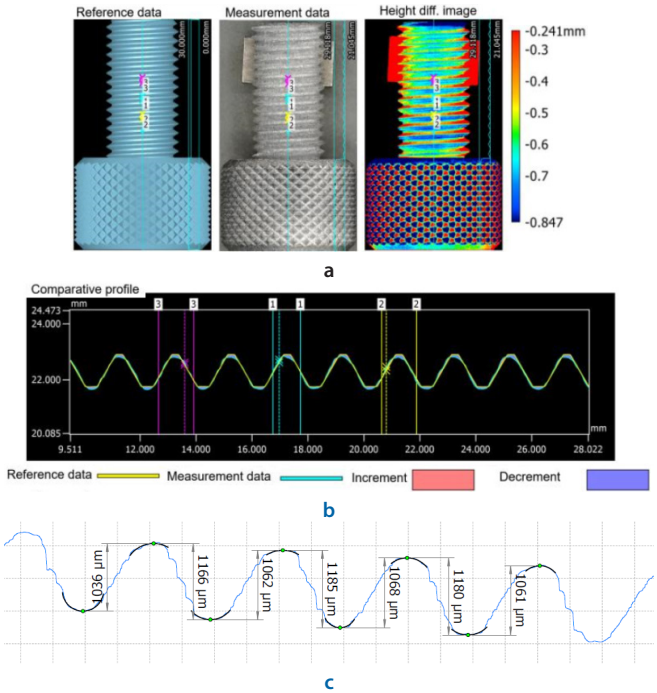

Figure 5. Comparison of the tooth height measurements for Sample-45 bolt teeth with reference CAD data (a), Comparative profile obtained by optical measurement (b), Bolt teeth profile obtained by tactile measurement (c).

For comparing the height difference of each tooth of the Sample-45 and Sample-90, the two measurement geometries, obtained by optical method, were compared to each other by defining Sample-45 as reference data and Sample-90 as measurement data. While these two geometries were match together, height difference image and comparative profile were obtained as in the Figure 7. Maximum difference was defined between the teeth near about the top edge and it was recorded as 0.779 mm which was very high and statistically significant. The difference became 0.090 mm and 0.063 mm while going from top to down of the geometries. The deviation at the top surface of Sample-90 may aroused by capillary effect which occurs when the fused polymer powder in an area acts as a fluid and tends to raise up along its borders. So, side edges of the part would be high and center of the top surface would be low. That is why top surface deviation of the Sample-90 was recorded as

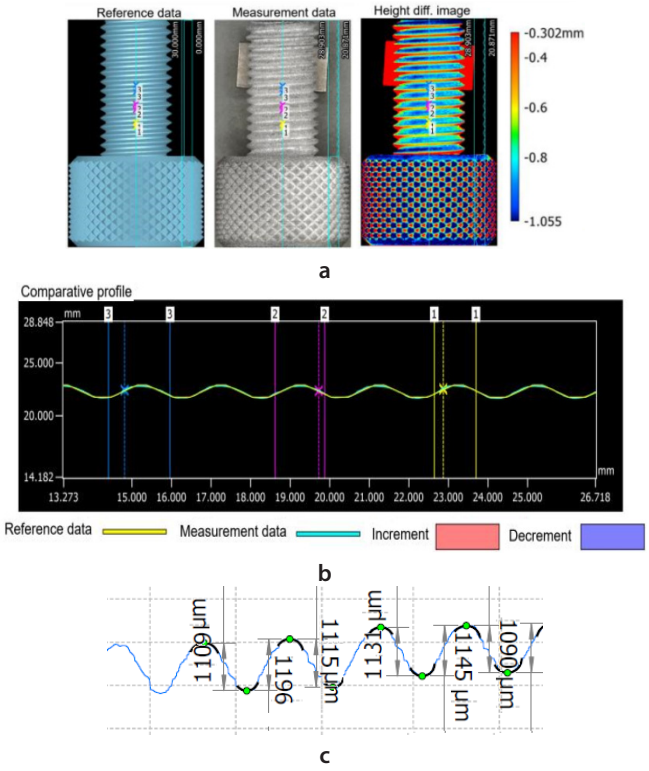

Figure 6. Comparison of the optical tooth height measurements of the Sample-90 with reference CAD data (a), Comparative profile obtained by optical measurement (b), Bolt tooth height measurements by tactile method (c).

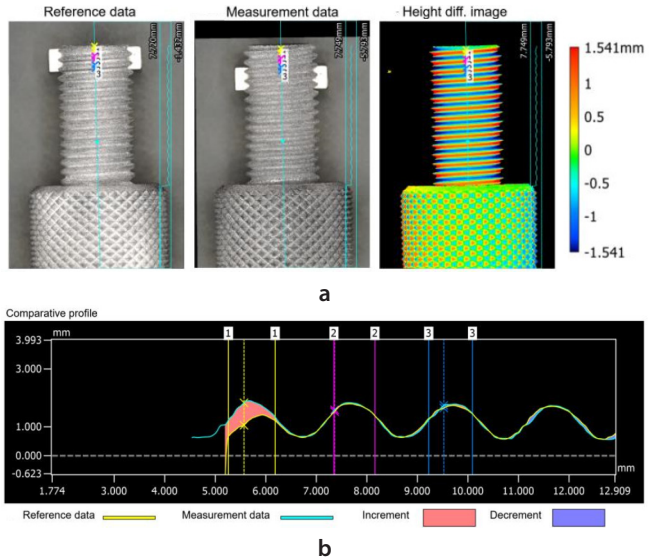

Figure 7. Comparison of two samples measurement data. Matching the two samples geometries (a), Comparative profile, shows the teeth height difference of Sample-90 and Sample-45 (b).

higher than the Sample-45. For improving the quality of the last layer it must be avoided to finish the printed parts with a large area to fuse [16].

Beside the height measurements, tooth angle and distance between the two teeth were also inspected for detailed evaluation of the bolt teeth profiles. Nominal tooth angle was 60° while the nominal distance between two teeth was 2 mm. The whole geometry and each tooth of the bolts were measured for defining average angular deviations and distance between each tooth precisely. Measurement procedures and results can be seen in Figure 8 and Figure 9.

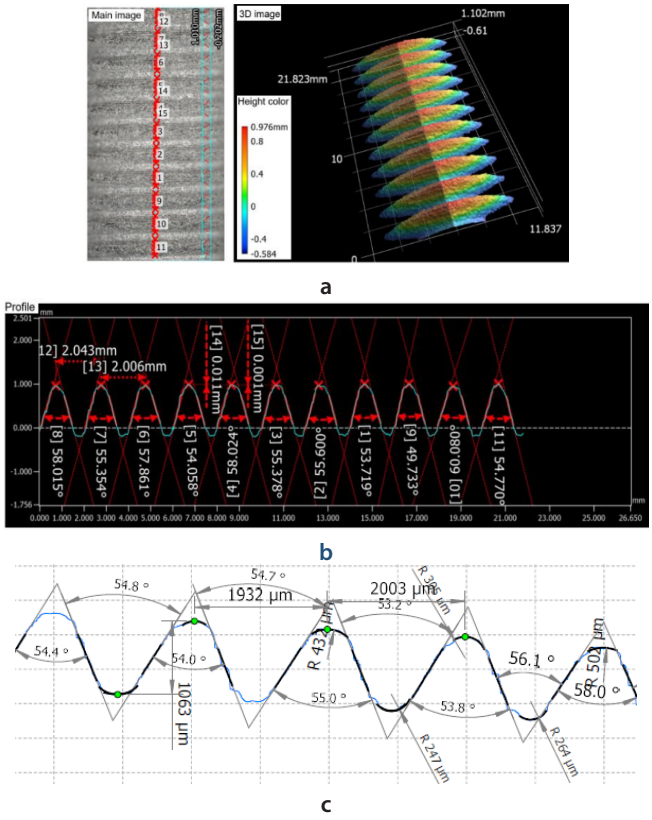

Figure 8. 3D optical tooth angle and distance measurement image of the Sample-45 (a) and measurement results (b), measurement procedure of 2D tactile tooth angle and distance measurement (c).

By optical measurement technique, average tooth angle for sample-45 was recorded as 55.69° with SD 2.792° where it was measured as 57.88° with SD 2.219° for sample-90. Tooth angle of reference CAD data was 60°, so the angular deviation was 4.31° for sample-45 and 2.12° for sample-90. These differences were statistically significant with p=0.000 for Sample-45 and p=0.010 for Sample-90. Also the difference between two sample tooth angle values were different significantly. By tactile measurements, average tooth angle of Sample-45 recorded as 55.32° with SD 1.980° and for Sample-90 as 58.009° with SD 2.047°. These tooth angle values were statistically different from each other with p= 0.000 and p=0.038 for Sample-45 and Sample-90 respectively. Moreover, tooth angle values of the both samples groups were significantly different from each other with p=0.026.

Mean value of the distance between two teeth were measured as 2.0245 mm with SD 0.0262 mm for Sample-45 and 1.9690 mm with SD 0.0834 mm for Sample-90 by optical

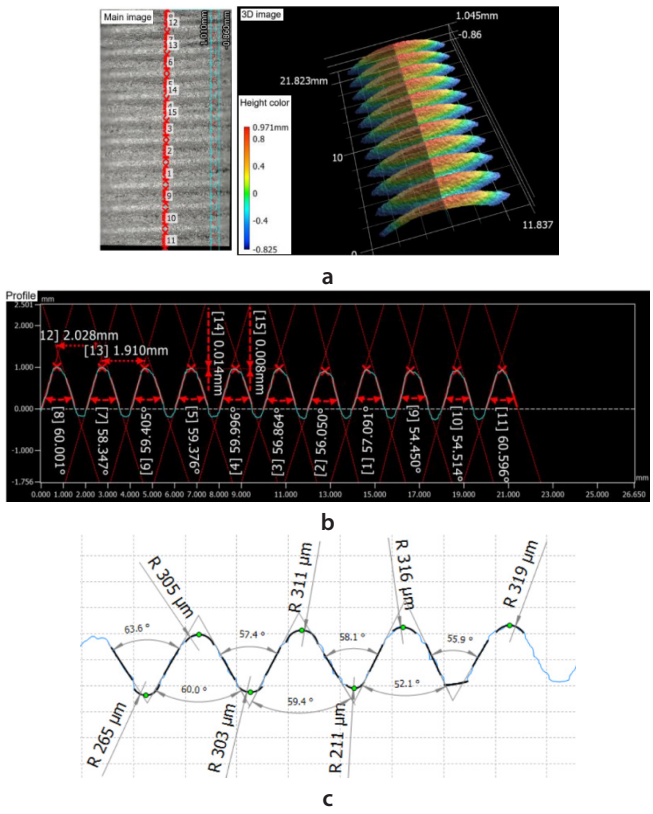

Figure 9. 3D optical tooth angle and distance measurement image of the Sample-90 (a) and measurement results (b), Measurement procedure of 2D tactile tooth angle and distance measurement (c).

method. These values were recorded as 2.0040 mm with SD 0.0438 mm for Sample-45 and 2.0680 mm with SD 0.0563 mm for Sample-90 by tactile measurements. All the distance values were statistically same with each other while the nominal reference distance value was 2 mm in CAD data.

4. CONCLUSION

In this study, effect of orientation angle on the surface roughness, tooth height, tooth angle and distance of two teeth of a bolt, manufactured by MJF process was investigated. Samples were printed in 90 and 45 degree of orientation angle. Roughness measurements and dimensional characterizations were applied by optical and tactile precision measurement systems. The results were indicated that,

- Orientation angle had significant effect on surface roughness. Perpendicular placement of the printed bolt provided better surface quality for the teeth.
- 45 degree inclined positioning provided lower tooth height difference than 90 degree.
- Tooth angle deviation of both sample groups were high and significantly different from nominal angle value of CAD data. Also, the deviation of Sample-45 was higher than Sample-90.
- Distance between two teeth was not significantly affected by orientation angle.
- Perpendicular positioning of the print part provides better surface quality and angular accuracy for bolt

teeth manufactured by MJF process.

In conclusion, it can be said that build orientation angle affects the surface quality and dimensional accuracy of MJF manufactured parts. For further studies, experiments are continuing by trying different orientation angles for determination of optimal positioning with different process parameters.

5. ACKNOWLEDGEMENT

In this study manufacturing of PA12 bolt samples by MJF were supported by Form Katmanlı İmalat ve Robot Teknolojileri A.Ş.- Turkiye. Tactile surface measurements were applied in Star Teknik Elektronik Cihaz San. ve Tic. Ltd. Şti.-Turkiye. Optical measurements were taken in TU Wien, Institute for Production Engineering and Photonic Technologies, Department of Industrial Metrology and Adaptronic Systems-Austria. The author would like to thank for the supports.

6. REFERENCES

[1] Sagbas, B., (2020). Post-Processing Effects on Surface Properties of Direct Metal Laser Sintered AlSi10Mg Parts. Metals and Materials International, 26(1): 143-153. doi:10.1007/s12540-019-00375-3

[2] Mele, M., Campana, G., Monti, G. L. (2019). Modelling of the capillarity effect in Multi Jet Fusion technology. Additive Manufacturing, 30: 100879. doi:10.1016/j.addma.2019.100879

[3] Riedelbauch, J., Rietzel, D., Witt, G. (2019). Analysis of material aging and the influence on the mechanical properties of polyamide 12 in the Multi Jet Fusion process. Additive Manufacturing, 27: 259–266. doi:10.1016/j.addma.2019.03.002

[4] Chatham, C. A., Long, T. E., Williams, C. B. (2019). A review of the process physics and material screening methods for polymer powder bed fusion additive manufacturing. Progress in Polymer Science, 93: 68–95. doi:10.1016/j.progpolymsci.2019.03.003

[5] Sillani, F., Kleijnen, R. G., Vetterli, M., Schmid, M., Wegener, K. (2019). Selective laser sintering and multi jet fusion: Process-induced modification of the raw materials and analyses of parts performance. Additive Manufacturing, 27: 32–41. doi:10.1016/j.addma.2019.02.004

[6] Morales-Planas, S., Minguella-Canela, J., Lluma-Fuentes, J., Travieso-Rodriguez, J., García-Granada, A.-A. (2018). Multi Jet Fusion PA12 Manufacturing Parameters for Watertightness, Strength and Tolerances. Materials, 11(8): 1472. doi:10.3390/ma11081472

[7] O'Connor, H. J., Dickson, A. N., Dowling, D. P. (2018). Evaluation of the mechanical performance of polymer parts fabricated using a production scale multi jet fusion printing process. Additive Manufacturing, 22, 381–387. doi:10.1016/j.addma.2018.05.035

[8] HP 3D Printing materials, (November 2019). Access date: 21.01.2020. https://www8.hp.com/h20195/v2/GetDocument.aspx?docname=4AA7-1533ENA

[9] Palma, T., Munther, M., Damasus, P., Salari, S., Beheshti, A., Davami, K. (2019). Multiscale mechanical and tribological characterizations of additively manufactured polyamide 12 parts with different print orientations. Journal of Manufacturing Processes, 40: 76–83. doi:10.1016/j.jmapro.2019.03.004

[10] HP Data Sheet, 3D High Reusability PA 12, (March 2018). Access date: 21.01.2020. https://static1.sw-cdn.net/files/cms/materials/data-sheets/HP%20Data%20sheet.pdf

[11] HP MJF Handbook- General Recommendations for Printing Processes, (March 2019). Access date: 21.01.2020. https://enable.hp.com/us-en-3dprint-mjfhandbook

[12] ISO, ISO 4287:2010-07 Geometrical Product Specifications (GPS) - Surface texture: Profile method - Terms, definitions and surface texture parameters.

[13] ISO 25178-2:2012 Geometrical product specifications (GPS) — Surface texture: Areal- Part 2: Terms, definitions and surface texture parameters.

[14] Sagbas, B., Durakbasa, N. M. (2019). Profile and Areal Surface Characterization of Additive Manufacturing Polymer and Metal Parts. Proceedings of the 12th International Conference on Measurement and Quality Control - Cyber Physical Issue, 240–246. doi:10.1007/978-3-030-18177-2_22

[15] Poyraz Ö., Solakoğlu, E.U., Ören, S., Tüzemen, C., Akbulut, G. (2019). Surface texture and form characterization for powder bed additive manufacturing Journal of the Faculty of Engineering and Architecture of Gazi University, 34(3): 1653-1664. doi:10.17341/gazimmfd.461588

[16] HP MJF Handbook- Design for Aesthetics. Access date: 21.01.2020. https://enable.hp.com/us-en-3dprint-mjfhandbook

EUROPEAN MECHANICAL SCIENCE
e-ISSN: 2587-1110

Research Paper

A Dynamic Approach in Production Management for Automotive Field

Banu Özkeser*

Koluman Otomotiv Endüstri A.Ş. R&D Center, Mersin, Turkey

Abstract

Solution proposals, based on dynamic approaches, can easily take place of the existing situations owing to the unlimited customer requests. Therefore, this may lead to a rapid transformation, triggering the manufacturing society to deal with the requirements for a sustainable competitive advantage. Especially, the automotive field, deeply affected by the fast-changing demands, brings about some new business models superimposing the existing ones because of the technology-intensive production management. This progress makes the world's expectation be higher depending on process innovation and minimizing the lead time may be declared as one of the top satisfaction points in the market. This paper, including the review of different manufacturing methods, highlights the awareness of the best implementations along with the production management in the automotive field. Moreover, the final objective is to develop a process innovation by designing a dynamic algorithm. The content of the paper, depending on multiple machines with multiple orders, is completed in all details by analyzing the gaps of the literature review. In the second step, the original algorithm is formed by taking into consideration the priorities. The achieved analysis is based on the main criteria and subcomponents of the scheduling of the manufacturing process. Finally, the algorithm, formed by four main priorities, leads the numerical implementations to be done in only one order and the results show that this approach can be a good way for minimization of total delays of orders. The results approve that the algorithm minimizes the delay and helps the customer increase their satisfaction.

Keywords: Automotive, Production Management, Manufacturing Methods, Process Innovation

1. INTRODUCTION

The production activities have become complicated due to the developing production techniques and growing production systems, and become out of control with simple production activities. Manufacturing processes which could be coped with simple approaches in the past, has become more detailed due to tool and technological improvements. However, it is inevitable that companies, using innovative approaches, will be successful in competition as they can use production management more effectively.

While planning in production management; long, medium and short term plans are taken into account. For the long term, it is foreseen that takes place from two to ten years; In the medium term, plans between one year and two years are taken into consideration. In product management, which includes short-term planning; the fact that orders have unique processing rows and preparation times depending on the processing sequence also makes process innovation in order to improve processes inevitable. Job-shop production systems, especially used in the automotive industry, is a production system that is not easy to realize production management due to its structure. The large number of orders in the job-shop type production system, each order's having its unique processing order and preparation time depending on the process order make the solution more complex.

Since the system is mostly dynamic, algorithms close to the optimum solution are preferred. The performance criterion required for each system may not be the same. The goal in this paper is to minimize the delivery time of the orders and balance the machines' usage capacities with the designed algorithm.

This paper is about an order-type production system with k workstations, where d_i delivery time and work route is random, with certain n jobs, coming to the system at random.

A wide literature survey is completed that addresses the approaches developed within the scope of production management and especially in the automotive field.

* Corresponding authour
Email: banuozkeser@gmail.com

European Mechanical Science (2020), 4(2): 53-58
doi: https://doi.org/10.26701/ems.678821
Received: January 22, 2020, Revised: February 19, 2020
Accepted: February 26, 2020, Published: February 29, 2020

Panwalker and Iskander classified the order of the jobs and priorities depending on four main factors. They are; earliest due date, implementation of the simple rules in the different queues in the same system, weighted prioritization and heuristic algorithms. All these are tested and the results are vary from each other in terms of real conditions. The results of their study show the system needs revision adapting to all possibilities [1].

In Sun and Lin's study, it is assumed that each job has its processing route, each machine can do only one job at the same time and it's impossible to stop the machines until the process is completed while a process is undertaken, Moreover, how long time each process has is presumably known. In this algorithm, the set of jobs waiting in front of a machine can be known precisely, the order to start the first operation can be determined and it is possible to calculate the delivery of a new job. In this respect, the algorithm has superiority over other approaches. However, they stated that in the calculation of delivery times, further studies should be done in order to get better results in minimizing the flow times and finishing the works on time [2].

Another study is completed on a technique that offers robust solutions to production scheduling problems. According to this study, makespan value is considered as a performance criterion. The makespan value is defined from the start time of the process to the last finish time [3].

Duenyas and Van Oyen aims to reduce the average waiting cost in a system with single-service parallel heterogeneous queues. First of all, in a two-tailed system, they developed an intuitive algorithm to determine the most accurate time for one job to move to another queue, and they tested this rule with simulation technique in many tailed systems and stated that the heuristic method they developed is effective in many problems [4].

In another paper, in which an interactive decision support system is developed for the solution of scheduling problems, the implemented steps are follows:

1. Identification of parameters that are important in decision making and measurement of these parameters
2. Determination of scheduling parameters
3. Specification of a control parameter as a time qualifier
4. Developing a better system to get rid of the bottlenecks of the current system
5. Defining an objective parameter for grouping the operations on each machine
6. Defining the procedure to be developed [5]

Godin stated that, in systems where re-scheduling was performed, the computer should not be used as a decision maker, but in pre-application information such as making calculations and testing decisions, rather than as a decision maker, as there were shortcomings in the model [6].

Vancheeswaran and Townsend take into account the subject to minimize the delays arising from the failure to comply with the delivery times of the orders, and the delay time is tried to be minimized with integer programming technique. In large systems, the difficulty of applying the technique has been demonstrated as it requires a lot of computation time [7].

Blackstone, Phillips and Hogg examined analytical approaches and simulation techniques on which of the pending jobs will be put into the first process. They found that even in small workshop models, analytical studies have become very complex. They said that in distribution systems producing workshops, no distribution rules give optimal results. They emphasized that charts using more than one rule rather than a single rule give better results [8].

Buxey investigated the theoretical approaches developed for scheduling problems in production systems and their applications in practice. Production scheduling is divided into four main groups: scheduling resources, delivering to orders, scheduling backwards according to deliveries and assigning priority orders and assignment to machines. He stated that while mathematical models can be successful in the first three groups, analytical approaches are not fully modeled with analytical approaches in determining the priority order of jobs and assigning them to machines, and the models are not flexible enough. He added that mathematical models and analytical approaches can be successful in small businesses in three other groups and in production systems where unexpected events are very rare [9].

Metaxiotis, Askounis, and Psarras divided the solutions of scheduling problems into two main groups as algorithmic approaches and remodeling approaches. After creating the mathematical model of the scheduling problem, they defined solutions such as integer or dynamic programming as algorithmic approaches that maximize the goal function or find solutions that are close to the best with intuitive approaches, and said that the model should be enriched in order to meet the desired targets in the remodeling approach. They said that after scheduling problem was modeled in algorithmic approaches, it focused on solution models, solutions were sought by creating different constraints and resources in the model for a satisfactory solution in re-modeling, and methods that gave quick results could be selected in the solution method. Considering that people spend 80-90% of their time in scheduling problems in determining the constraints of the problem and 10-20% of their time in scheduling, enrichment of the decision-support systems with the modeling approach can be the main contribution of the modeling without human intervention, and this type of approach is better in scheduling problems. They stated that they produced solutions [10].

Kerr and Ebsary have tried to develop a decision support model that can schedule the production system by making use of the experience of the decision maker who created the scheduling in the production system and the methods de-

veloped by the decision maker. They systematized the methods they use as an intuitive rule. Besides, they made calculations with the computer and loaded the machine for both current scheduling and possible situations. Thus, they have established a system where very fast and alternative scheduling is done [11].

In another study, it is indicated that the will to reduce vehicular traffic in cities, to improve its regulation have made smart mobility an increasingly important topic during the last years. As a consequence, automotive companies have begun to develop electric vehicles and related components. In this context, a well known Italian company operating in automotive field, is giving its important contribution working on many research projects concerning vehicle electrification. The presentation of paper is mainly the report of the activities concerning the design of the production process, along with the development of the FMEA [12].

Given the recent dynamics of the automotive industry, the ability for a firm to be flexible has often taken priority over other performance indicators. Using the notion of distinct business models and trade-offs as our theoretical lens, the purpose of this study was to pay attention to lean manufacturing, a different approach. Data was obtained from 140 automotive companies and implementing agile production methods were found to be more flexible in comparison with firms implementing lean production methods [13].

2. MATERIALS AND METHOD

In order to keep production under control, the enterprise must have a dynamic infrastructure. Instant information of both orders and machines is needed for applying dynamic scheduling algorithms. In the developed algorithm, information such as average workloads on machines, average queue waiting times and remaining idle times of orders will be needed.

The main features of the production system discussed in this study are listed below:

- More than one product is produced. The product range is very wide, since the study was carried out in an order-based enterprise.
- The work order followed by each product is different. It is also possible to arrive new orders with unknown transaction order, although the transaction route is generally known.
- Multiple machines perform similar operations.
- Product order sizes are different. Even if orders of very large size have come, production is made in one lot and the order is not divided.
- The unit capacities of the machines are determined.
- Delivery times of orders are clear. Delivery times are determined when the order is placed.
- Some machines have preparation times depending on the previous process.

Assumptions:

- Preparation times were considered as part of the waiting time in the queue and did not need to be considered separately.
- It is assumed that the machines operate without malfunction in line with their unit capacities.
- Machines that do the same job have the same capacity.
- Transport times between workstations have been neglected.
- Workstations cannot refuse incoming orders.
- Reprocessing of orders has been ignored.
- Overtime is out of the question.
- Due to the orders route, they can visit the same workstation more than once.

The notation used in the formulation of the problem is as follows:

i: order number i:1….n

k: work station number k:1….s

D_i: delivery time of i. order

Z: today's date

q_i: the quantity of i order

S_i: the idle time of the i order (without waiting)

S_{ibek} : the idle time of the i order (with waiting)

$ORT(W_k)$: average queue waiting time of k workstation

$ORT(W_{i\ (k\rightarrow n}$): avarage waiting time for the next station after k workstation of i order

P_k : the queue length of k workstation (numbers)

$ORT(P_k)$: avarage the queue length of k workstation (numbers)

$ORT(P_{i\ (k\rightarrow n}$): avarage the queue length for the next station after k workstation of i order

t_{ik}: the process time of i order in k workstation

$t_{i(k\rightarrow l)}$: the unit process time after k workstation of i order

X_{ik}: time to reach the station k of the delayed order i (minute)

G_k: A set of parts that will delay the k station

Kk: Set of parts delays waiting at the k station

Bk: A set of parts with possible delays at the k station

hk: Time to reach the minimum k station of the delayed parts that will stop by the k station (minute)

Mk: Set of time to finish the work of the machines at the k station

Ykm: m machine at the k station to be assigned

I_i: the last Workstation of i order

In the algorithm development phase, the main goal was determined as minimization of delay times, four different priority situations were revealed by examining the situations that might be encountered in this direction and these situ-

ations were tried to be formulated to minimize the delays.

The designed algorithm has four priorities, explained in below:

1. priority: Parts previously reported to stop by the station

S_i is calculated for the parts waiting in the queue of all stations in the system. If a negative S_i value is found, a signal is sent to all workstations that the order will undergo. In this signal, the times for the parts to reach the relevant workstations are the times when the processing times are taken into account, for which the delays are not taken into account. In the light of this information, when assigning a machine, the first priority is, of course, late orders and delivery times.

When a part comes out of the machine at the workstation and it is decided which part to replace; this workstation will first investigate whether there are any delayed parts of its workstation with reported reach time. If there are no parts reported, it takes the 2nd priority. If any delayed parts are reported, it is checked if there is a machine that will go into empty state before the delayed part reaches the station. if any, it takes the second priority, otherwise the empty machine waits for the delayed part to be reported. Here is the notation of this first priority:

Define G_k set

If $G_k=\emptyset$, go to 2. priority

If $G_k\neq\emptyset$ and hk > min(M_k) $\notin Y_{km}$, go to 2. priority

If $G_k\neq\emptyset$ and hk < min(M_k) $\notin Y_{km}$, assign the part having h_k value to the empty machine and arrange X_{ik} for the selected part

2. priority: waiting parts that occurred while waiting in the queue

The beginning of the signal logic occurs at this step. Delayed parts are detected by the system for the first time at this stage and signals are sent to almost all workstations. When a part is removed from the machine at the workstation and which part is to be replaced, the idle times of the parts waiting to be processed are calculated first. If a negative value is found, it signals. Then, the idle time weighted in the queue with the waiting times is determined. What is meant here is that whichever of the workstations it will drop by for the order, the average waiting time is greater, and that the workstation should have more idle time. Selects the order with the smallest value to be processed. Here is the notation of this second priority:

Calculate $S_i = D_i - Z - (ti \times q_i)$

If Si $\not<$ 0 , go to 3. priority

If Si < 0 , assign the min (S_i x [ORT(W_k) / ORT($W_{i\,(k\rightarrow n)}$) value to the empty machine

$Xik = \Sigma\,(t_{ir} \times q_i)$ for k= xi…..l_i

3. priority: Parts that may be delayed

In cases where there are no orders to be delayed, new idle times are calculated by taking into account the average queue waiting times in the workstations, they will stop for the parts waiting in the queue. The aim here is to find out which of them are candidates to be late if the orders continue their normal route. If the ratios are evaluated as a result of the calculations, these parts are important and priority parts for the system. Among them, the order with the smallest weighted idle time is selected to be traded on the empty machine. If no negative value is found, 4th priority is passed. Here is the notation of the third priority:

Calculate $S_{ibek} = Di - Z - \Sigma\,((t_{ir} \times q_i) + ORT(W_k))$

If $S_{ibek} \not< 0$, go to 4. Priority

If $S_{ibek} < 0$, assign the min (S_{ibek} x [ORT(W_k) / ORT($W_{i\,(k\rightarrow n)}$) value to the empty machine

4. priority: workload balancing

When there are no delayed or delayed parts, priorities to balance the workloads of the machines take the first place. This process is tried to be done by sending parts from the stations where the orders will go, to those with low workload and by not sending parts to stations with high workload except emergency parts. For this purpose, workstations first calculate their workload. Here is the number of parts in the queue meant as workload. If the number of parts in the queue is more than the average number of parts in the queue, this means the workstation is dense. The notation is explained below:

If P_k > ORT(P_k) , assign the part having tha value of min (t_{ik} / t_{ikn}) to the empty machine

If P_k < ORT(P_k) , assign the jobs of $P_{i\,(k\rightarrow n)}$ < ORT($P_{i\,(k\rightarrow n)}$) to the the empty machine having max ($t_{i\,(k\rightarrow n)}$)

If P_k < ORT(P_k), assign the other jobs except for $P_{i\,(k\rightarrow n)}$< ORT($P_{i\,(k\rightarrow n)}$) to the the empty machine having min ($t_{i\,(k\rightarrow n)}$)

3. RESULTS AND DISCUSSION

The algortihm is implemented in the manufacturing line of a company, in automotive field. There are three machines in *k* workstation and one of them is empty.

1. sample

Initially, X_{ik} workstation and M_i are calculated.

Table 1. Access time of the 1st sample

M_i	times of M_i
M_2	50
M_3	120

Table 2. M_i time of the 1st sample

X_{ik}	X_{ik} access time
X_{5k}	15
X_{7k}	90

The minimum reach time of delayed parts is 15 minutes.

The minimum time of the running machines is 50 minutes.

Since 15 <50, the M_i machine waits for the X_{5k} order.

2. sample

Initially, X_{ik} workstation and M_i are calculated.

Table 3. Access time of the 2nd sample

M_i	times of M_i
M_2	15
M_3	120

Table 4. M_i time of the 2nd sample

X_{ik}	X_{ik} access time
X_{5k}	50
X_{7k}	90

The minimum reach time of delayed parts is 50 minutes.

The minimum time of the running machines is 15 minutes.

Since 50>15, the M_i machine goes to second priority because M_2 machine will be empty before passing through the X_{5k} workstation.

Table 5. S_i value for the parts waiting in the queue

$ORT(W_k)$	$ORT(W_{i(k\rightarrow n)})$
-	-
5	10
10	100

Table 6. $ORT(W_{i(k\rightarrow n)})$ value

S_i	X_{ik} access time
S_4	50
S_6	-5
S_7	-20

3. sample

Initially, X_{ik} workstation and M_i are calculated.

Table 7. Access time of the 2nd sample

M_i	times of M_i
M_2	15
M_3	120

Table 8. M_i time of the 2nd sample

X_{ik}	X_{ik} access time
X_{5k}	50
X_{7k}	90

The minimum reach time of delayed parts is 50 minutes.

The minimum time of the running machines is 15 minutes.

Since 50>15, the M_i machine goes to second priority because M_2 machine will be empty before passing through the X_{5k} workstation.

Table 9. S_i value for the parts waiting in the queue

S_i	time
S_4	50
S_6	10
S_7	5

$ORT(W_k)$	$ORT(W_{i(k\rightarrow n)})$
-	-
-	-
-	-

Table 9. (*Cont.*)

$S \not< 0$, so it's possible to pass the third priority.

S_i	time
S_4	50
S_6	3
S_7	-7

$ORT(W_k)$	$ORT(W_{i(k\rightarrow n)})$
-	-
-	-
10	100

4. sample

Initially, X_{ik} workstation and M_i are calculated.

Table 10. Access time of the 2nd sample

X_{ik}	X_{ik} access time
X_{5k}	50
X_{7k}	90

Table 11. M_i time of the 2nd sample

M_i	times of M_i
M_2	15
M_3	120

The minimum reach time of delayed parts is 50 minutes.

The minimum time of the running machines is 15 minutes.

Since 50>15, the M_i machine goes to second priority because M_2 machine will be empty before passing through the X_{5k} workstation.

4. CONCLUSION

While the main target of businesses was profitability etc., today, the main target has become customer satisfaction. Establishing a system that will provide products or services that satisfy customers is the basic criterion of success. In this context, scheduling algorithms help companies to set up and manage systems with the process innovation it creates. In this way, we can provide services to the customer without delay on the specified delivery date, and we can also make progress on issues such as efficient use of resources and profitability. Although there are many sources on the subject in the literature, static systems are generally emphasized and dynamic studies are not included. Heuristic algorithms are taken into consideration as well as algorithms for the optimal result. The problem addressed in this study is the multiple order problem that is encountered especially in the automotive industry. The purpose of the developed algorithm, a process innovation, is to minimize the delay times of the orders and balance the machine capacities. A certain target has been determined in the algorithm and many possibilities are tried to be formulated. The study was based on the production of orders in only one lot. If algorithms are developed on the basis that lots can be divided, more improved results can be obtained. It is assumed that the machine times that perform the same operation are the same and this acceptance can be changed in future studies. Machine stoppages, rework, etc. are ignored. These issues can also be addressed in the future.

5. REFERENCES

[1] Panwalkar, S. S., Iskander, W. (1977). A Survey of Scheduling Rules. Operations Research, 25(1): 45–61. doi:10.1287/opre.25.1.45

[2] Sun, D., Lin, L. (1994). A dynamic job shop scheduling framework: a backward approach. The International Journal of Production Research, 32(4): 967-985.

[3] Tjornfelt-Jensen, M., Hansen, T. K. (1999). Robust solutions to job shop problems. In Proceedings of the 1999 Congress on Evolutionary Computation-CEC99 IEEE (Cat. No. 99TH8406) 2: 1138-1144.

[4] Duenyas, I., Van Oyen, M. P. (1996). Heuristic scheduling of parallel heterogeneous queues with set-ups. Management Science, 42(6): 814-829.

[5] Banerjee, S., Banerjee, A., Burton, J., Bistline, W. (2001). Controlled partial shipments in two-echelon supply chain networks: a simulation study. International Journal of Production Economics, 71(1-3): 91-100.

[6] Godin, V. B. (1978). Interactive scheduling: historical survey and state of the art. AIIE Transactions, 10(3): 331-337.

[7] Vancheeswaran, R., Townsend, M. A. (1993). Two-stage heuristic procedure for scheduling job shops. Journal of Manufacturing Systems, 12(4): 315-325.

[8] Blackstone, J. H., Phillips, D. T., Hogg, G. L. (1982). A state-of-the-art survey of dispatching rules for manufacturing job shop operations. The International Journal of Production Research, 20(1): 27-45.

[9] Buxey, G. (1989). Production scheduling: Practice and theory. European Journal of Operational Research, 39(1): 17-31.

[10] Metaxiotis, K. S., Askounis, D., Psarras, J., (2002), Expert systems in production planning and scheduling: A state-of-the-art survey. Journal of Intelligent Manufacturing, 13(4), 253-260.

[11] Kerr, R., Ebsary, R. (1988). Implementation of an expert system for production scheduling. European journal of operational research, 33(1), 17-29.

[12] Righettini, P., Strada, R., Gosatti, A., Togni, S., Camozzi, F., Fissore, C. (2019). Smart Mobility: a modern approach to automotive product development for vehicle electrification. 2019 IEEE 5th International Forum on Research and Technology for Society and Industry (RTSI). doi:10.1109/rtsi.2019.8895541

[13] Qamar, A., Hall, M. A., Collinson, S. (2018). Lean versus agile production: flexibility trade-offs within the automotive supply chain. International Journal of Production Research, 56(11): 3974-3993.

EUROPEAN MECHANICAL SCIENCE
e-ISSN: 2587-1110

Research Paper

Production, Characterization and Surface Properties of Sr Doped Hydroxyapatite Coating on Magnesium Alloy by Hydrothermal Method

Turan Gurgenc*

Firat University, Automotive Engineering, 23119, Elazig, Turkey

Abstract

In this study, the surface of AZ91D magnesium alloy was coated with undoped and at different ratios strontium doped hydroxyapatite. Coatings were carried out at 180 °C in 3 hours. The surface roughness of the coated samples was determined and the microstructure of the phases forming on the coated surfaces were examined by scanning electron microscopy (SEM). The chemical composition of the phases formed on the coated surfaces was determined by energy dispersed X-ray spectroscopy (EDS). The phases formed on the surfaces were characterized by X-Ray diffraction (XRD) and Fourier transform infrared spectrometry (FT-IR). The AZ91D magnesium alloy was coated successfully with undoped and strontium doped hydroxyapatite by hydrothermal method. The highest surface roughness value was measured as R_a = 8.255 µm in 15% strontium doped sample. It was determined that the (Ca + Sr) / P ratios of the coatings were higher than the stoichiometric ratio of hydroxyapatite, 1.67. It was determined that the closest coating to the stoichiometric ratio was 10% Sr doped coating.

Keywords: Hydroxyapatite coating, Magnesium alloy, Hydrothermal method, Surface roughness, Biomaterial.

1. INTRODUCTION

Repairing damaged bone tissue one of the important topics in tissue engineering. Implant materials used in tissue engineering should be biocompatible and biodegradable in the human body during the repair of bone tissues [1]. In recent years, magnesium (Mg) alloys have become very interesting among metallic implants due to their important advantages especially in orthopedic applications. These advantages include its extremely lightweight, limited biological reactions, biodegradability, outstanding mechanical properties close to natural bone, and excellent biocompatibility. In addition, the presence of Mg^{2+} ions in apatite crystals can increase osteoblast adhesion rate and increase bone formation [2-4]. Besides these advantages, low wear-resistance and weak corrosion resistance especially in physiological solution are the most important disadvantages of Mg implants. In the implants exposed to corrosion and wear, the mechanical properties deteriorate before sufficient bone healing and limits their usage by preventing the use of implants as a load-bearing material [2, 3]. The most effective and efficient way to avoid these disadvantages of Mg implants is to increase their corrosion resistance, wear-resistance and biocompatibility by modification their surfaces with a biocompatible protective coating [2, 5]. Synthetic hydroxyapatite is one of the most preferred among biocompatible coatings ($Ca_{10}(PO_4)_6(OH)_2$, HA). This is because hydroxyapatite has the most similarity to the mineral part of the bone, excellent biocompatibility, good biodegradability and high osteogenic potential [6, 7].

The most commonly used techniques for coating the surfaces of Mg alloys with HA are sol-gel, electrodeposition, biomimetic method, atmospheric plasma spraying and hydrothermal method. Among these methods, hydrothermal method has advantages such as being simple, cost effective and needing low temperatures [8].

Strontium (Sr) is an element in the human body that is usually found in the body skeleton and has bone targeting properties. Sr has some positive properties like playing an important role in bone formation, the presence of Sr ions in biological environments, greatly increasing osteoblast differentiation, antimicrobial effect, inhibiting osteoclast activity, increasing preosteoblastic cell proliferation and bone matrix synthesis. Due to such positive properties, Sr has been doped to HA in recent years for improving the biological

* Corresponding authour
Email: tgurgenc@firat.edu.tr

European Mechanical Science (2020), 4(2): 59-64
doi: https://doi.org/10.26701/ems.686549
Received: February 7, 2020, Revised: February 21, 2020
Accepted: March 5, 2020, Published: March 7, 2020

performance of HAs [9, 10].

Zhang et al. coated the surface of AZ31 magnesium alloy with hydroxyapatite by hydrothermal method at different temperatures and times [11]. Sun et al. investigated the coating surface properties and corrosion resistance of the AZ91D magnesium alloy, which they coated with fluorinated hydroxyapatite by hydrothermal method [8]. Yang et al. coated the surface of the ZK60 magnesium alloy with hydroxyapatite by hydrothermal method at different times [12]. In another study, Mg-2.9Gd-1.5Nd-0.3Zn-0.3Zr magnesium alloy was coated with hydroxyapatite by hydrothermal method [13]. Li et al. coated the surface of pure magnesium with calcium phosphate by hydrothermal method [14]. Asl et al. coated the surface of the AZ31 magnesium alloy with calcium phosphate by hydrothermal method at different temperatures [15]. Wang et al. coated the ZK60 magnesium alloy with Sr doped hydroxyapatite at different doping ratios (3%, 5% and 10%) by hydrothermal method [16].

As a result of the literature studies, not many studies have been encountered regarding the coating of AZ91D magnesium alloy with Sr doped hydroxyapatite by hydrothermal method and it has been decided to carry out this study. In this study, the surface of AZ91D magnesium alloy was coated with Sr doped hydroxyapatite in different doping ratios by hydrothermal method in constant process parameters. Surface roughness of coated surfaces was determined and microstructural properties of coated surfaces were analyzed by FT-IR, SEM, EDS and XRD.

2. EXPERIMENTAL DETAILS

In present study, AZ91D magnesium alloy with a diameter of 20 mm and a thickness of 10 mm, whose chemical composition is given in Table 1, was used as the substrate material. The substrate material was polished with 1200 mesh SiC sandpaper and then cleaned with ultrasonic bath for 15 min. with acetone and then dried with hot air. For HA coating, firstly 0.1 M Merck brand $Ca(NO_3)_2.4H_2O$ was added to 30 ml of pure water in the beaker and stirred for 30 min. at room temperature in a magnetic stirrer. Fluka analytical brand 0.06 M $H_9N_2O_4P$ was added to 30 ml of pure water in a second beaker and stirred for 30 min. at room temperature in a magnetic stirrer. The mixture containing $H_9N_2O_4P$ was then poured into the mixture containing $Ca(NO_3)_2.4H_2O$ and stirred together for 30 minutes at room temperature in a magnetic stirrer. The pH of the mixture was adjusted to 4 with HNO_3 while stirring was continiue. Finally, after stirring this mixture for another 10 min. in a magnetic stirrer, it was ultrasonicated for 30 min. and the final mixture was obtained. After the substrate material was placed on the bottom of the autoclave, the final solution was poured into the autoclave and placed in the hydrothermal reactor. Hydrothermal treatment was carried out at 180 °C for 3 hours and when the reactor temperature reached room temperature, the sample was removed and washed several times with pure water and then dried at 60 °C for 1 hour. Production methods of Sr doped samples are the same as HA coating. Only for the production of Sr additive samples, Acros organic brand $Sr(NO_3)_2$ was added in different [Sr] / [Sr + Ca] molar ratios (5%, 10%, 15% and 20%,) keeping the molarity constant for the first solution containing $Ca(NO_3)_2.4H_2O$. Pure hydroxyapatite coated sample was named HA and 5%, 10%, 15% and 20% Sr doped samples were named as Sr5HA, Sr10HA, Sr15HA and Sr20HA, respectively.

The surface roughness of the produced samples was determined using the Mitutoyo SJ-201 profilometer. Measurements were carried out from 10 different points of the coating surfaces and the surface roughness values were calculated by calculating the average. Microstructures of sample surfaces were examined with ZEISS EVO-MA10 brand SEM device in different magnifications. The chemical compositions of the coated surfaces were measured using the Bruker brand EDS detector connected to the ZEISS EVO-MA10 brand SEM device. The phases formed on coated surfaces were determined by XRD. XRD analyzes were performed on the Malvern Panalytical brand device at CuKα (λ = 1.5406Å) radiation, 2θ = 20 - 90° scanning range at 40 mA and 45 kV. FT-IR analysis was carried out on Thermo Scientific Nicolet IS 5 brand FT-IR spectrometer device with a scanning range of 4000 - 550 cm^{-1}.

3. RESULTS AND DISCUSSION

Figure 1 shows the coating surface images of samples coated with hydrothermal method. As can be seen, AZ91D magnesium alloy was successfully coated with undoped and Sr doped hydroxyapatite by hydrothermal method. No visible cracks or porosity were found on the coating surfaces. In addition, the coating layer is combined with the substrate surface well.

Table 1. Chemical composition of AZ91D (at.-%).

Mg	Al	Zn	Mn	Cu	Si	Other metals
88-90.50	8.5-9.5	0.45-0.9	0.17-0.4	0.025 max.	0.050 max.	Rest

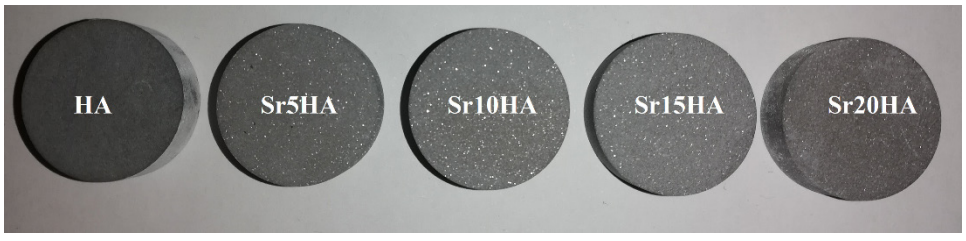

Figure 1. Macro surface images of coated samples.

The surface roughness values of the coated samples are seen in Figure 2. Surface roughness value of the sample coated with HA is lower than the Sr doped samples. Surface roughness increased with increasing Sr doping ratio up to 15%. Then, when the Sr doping ratio reaches to 20%, the surface roughness value decreased. This change in surface roughness is thought to occur due to the change in the shape and size of the crystals formed on the coated surface due to different doping ratios [15, 17]. In implants generally rough surfaces are preferred compared to a smooth surface. This is because of the surface roughness is an important factor for better osseointegration and biomechanical bonding. Thanks to the surface roughness, a better adhesion can be achieved between the implant surface and the bone [17]. The SEM photos are shown in Figure 3 also confirm the different microstructures formed on the coating surfaces. Similar shaped structures have also been seen in previous researches on hydroxyapatite coating of magnesium alloys by hydrothermal method [12, 15]. The coating surfaces of HA coated samples consisted of fine-grained triclinic and hexagonal structures compared to Sr-doped samples (Figure 3a and b). In Sr doped samples, these structures are more coarse and there are some spherical shaped particles in between these structures (Figure 3c-i). EDS analysis results obtained from coating surfaces at low magnification are given in Table 2. The (Ca + Sr) / P ratio of all samples is higher than 1.67, which is the stoichiometric ratio of HA, and the sample with the closest value to this ratio is 10% Sr doped sample [18]. As expected, as the Sr doping rate increased, the Sr composition in the coating layer increased. The (Ca + Sr) /P ratio of the flower-shaped structure at point-1 in Figure 3b is 1.88 and the crystal at point-2 is 2.01. In the Sr5HA sample, the crystalline (Figure 3d-point-3) (Ca + Sr) / P ratio is 1.46 and the spherical particle's (Ca + Sr) / P ratio is 1.98 (Figure 3d-point-4). The crystalline (Ca + Sr) / P ratio at point-5 in Figure 3f is 1.80 and the particle at point 6 is 1.85. The crystalline (Figure 3h-point-7) and particle's (Figure 3h-point 8) (Ca + Sr) / P ratios of 15% Sr doped sample are 1.56 and 1.60, respectively. The crystalline (Ca + Sr) / P ratio at point-9 in Figure 3i is 1.52 and the particle at point 10 is 1.93. As can be seen from the EDS analysis results, with the change of the Sr doping ratio, the (Ca + Sr) / P values of the structures in the coating layers changed. It has been seen also in the previous studies that the rates of doping elements change the (Ca + M) / P (M = doping element) ratios differ [19, 20]. In addition, the spherical shaped particles in the Sr doped samples are richer by Sr element and the (Ca + Sr) / P ratio of these particles are higher than the crystal structures.

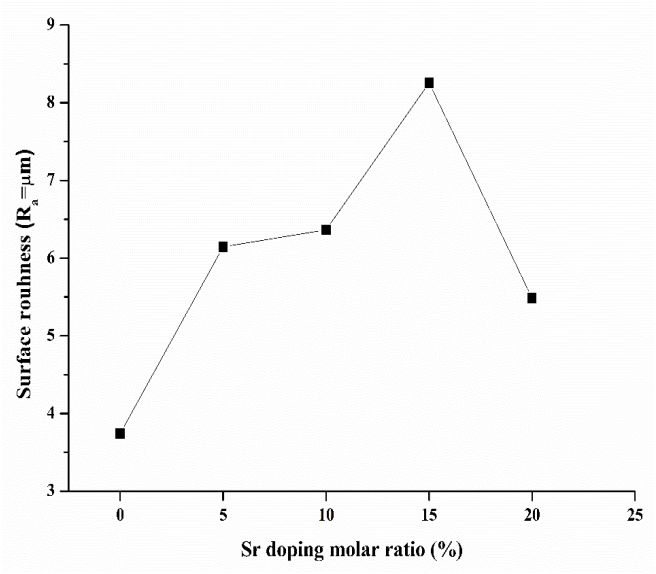

Figure 2. Surface roughness values of coated samples.

When XRD diffraction patterns of pure HA and Sr doped HA coated samples are examined, sharp HA peaks are observed alongside Mg peaks (Figure 4). The absence of sharp peaks of other structures other than these sharp peaks indicates that the coatings are highly crystalline and that HA coating is successfully performed on Mg by hydrothermal method [9, 17]. The peak intensities of Sr doped samples in the (002) planes are higher than the undoped sample and other HA peaks. This shows that the crystal plane HA (002) is directed to AZ91D in the same manner as pure Mg [18]. Again, XRD results are generally in agreement with previous researches [18, 21].

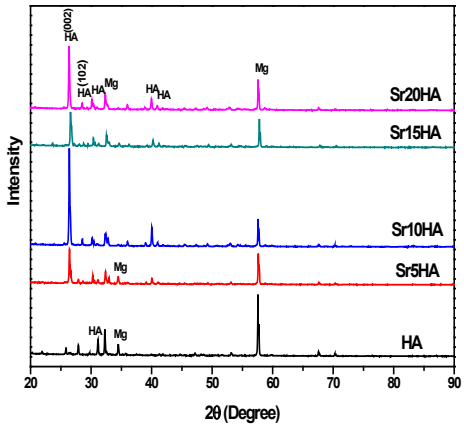

Figure 4. XRD analysis results.

FT-IR analysis results of samples are shown in Figure 5. The peak at about 601 cm^{-1} correspond to vibration of PO_4^{3-} [15, 17]. The bands at about 1022 cm^{-1} and 980 cm^{-1} in HA and 1018 cm^{-1} in Sr5HA, 1017 cm^{-1} in Sr10HA, 1011 cm^{-1} in Sr-

Table 2. EDS analysis results taken from coating surfaces (at.-%).

Sample	Ca	P	O	Mg	Zn	Sr	(Ca + Sr) / P
HA	33.18	12.33	53.18	0.72	0.58	0.00	2.69
Sr5HA	29.53	12.26	57.32	0.70	0.00	0.19	2.42
Sr10HA	25.62	15.09	58.88	0.00	0.05	0.36	1.72
Sr15HA	25.51	13.21	59.34	0.44	0.55	0.94	2.00
Sr20HA	25.11	15.03	58.68	0.00	0.00	0.99	1.74

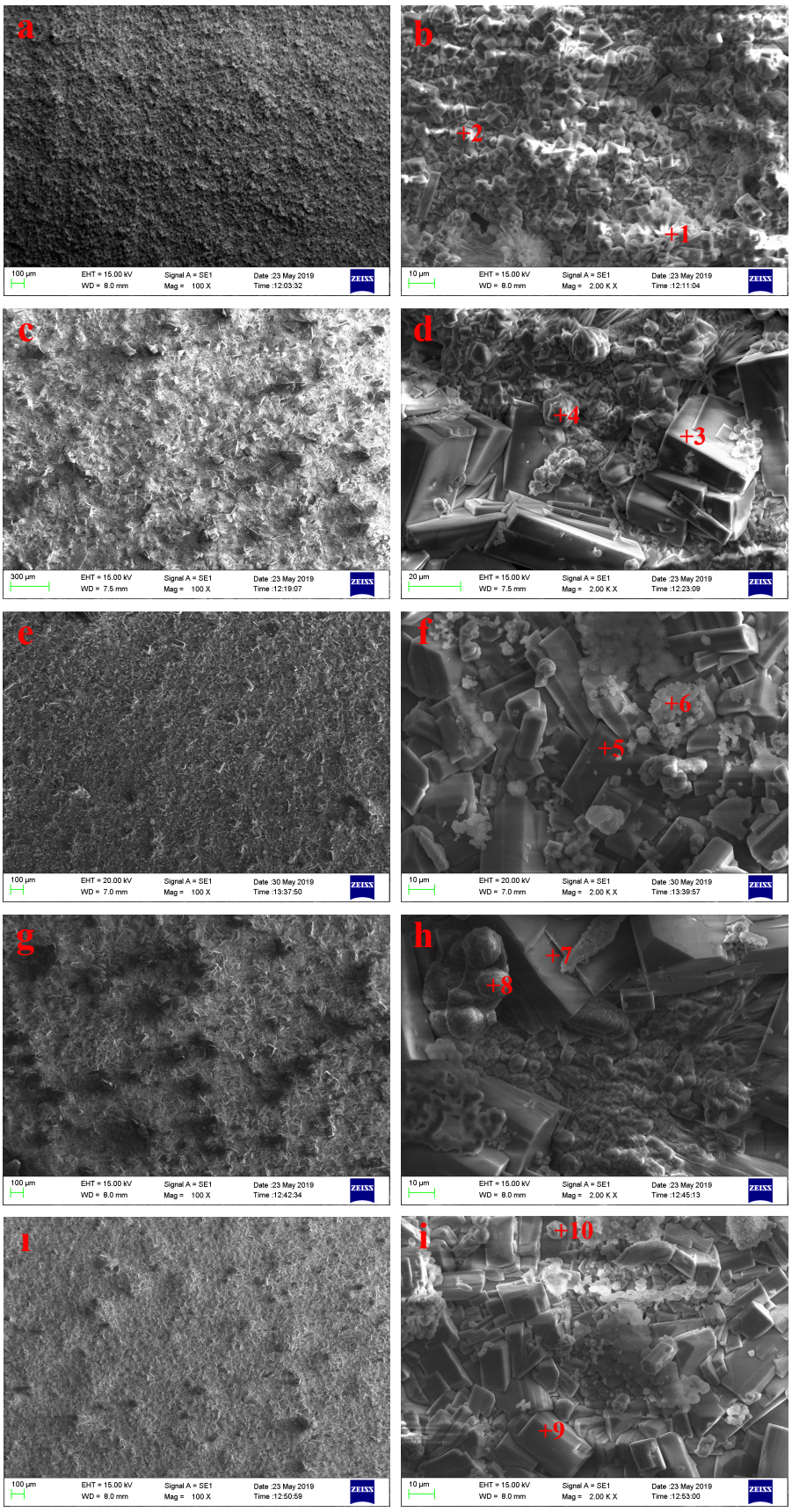

Figure 3. The coating surface SEM photographs of the samples a) HA x100, b) HA x2000, c) Sr5HA x100, d) Sr5HA x2000, e) Sr10HA x100, f) Sr10HA x2000, g) Sr15HA x100, h) Sr15HA x2000, ı) Sr20HA x100 and i) Sr20HA x2000.

doi: https://doi.org/10.26701/ems.686549

15HA and 1015 cm^{-1} in Sr20HA are ascribed to stretching modes of PO_4^{3-} [13]. The bands observed at 1651 cm^{-1} in Sr-10HA, 1726 cm^{-1} in Sr15HA and 1731 cm^{-1} in other samples correspond to H_2O [14]. The peaks observed at about 2362 cm^{-1} orginate from CO_2 in the air [14]. The wideband centered at approximately 3360 cm^{-1} is ascribed to adsorbed/lattice water [13, 17].The FT-IR analysis results support to XRD analysis and are generally in agreement with the previous researches [13-15, 17].

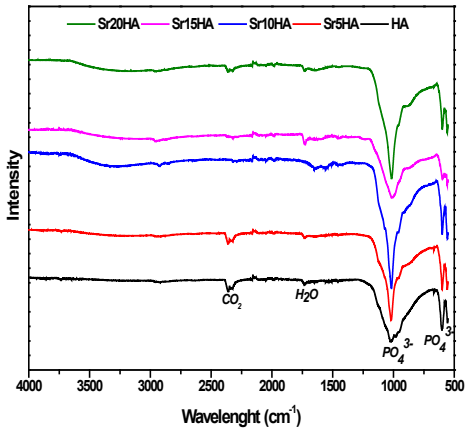

Figure 5. FT-IR analysis results.

4. CONCLUSIONS

- The surface of the AZ91D magnesium alloy was successfully coated with HA and Sr doped HA.
- The surface roughness value of coated surfaces increased with increasing Sr doping ratio. The coating surfaces of HA coated samples consisted of finer grained structures than Sr doped samples. The coating layers are generally consisted of HA and Mg.
- The (Ca + Sr) / P ratios of the undoped and Sr doped samples are higher than the stoichiometric ratio (1.67) of HA. The closest (Ca + Sr) / P ratio to the stoichiometric ratio of HA was 1.72 in the sample with 10% Sr doped.
- It is thought that 10% Sr doped HA coating can be used as an implant material since the surface roughness value is high and (Ca + Sr) / P ratio is closest to stoichiometric ratio.

REFERENCES

[1] Dehghanian, C., Aboudzadeh, N., Shokrgozar, M. A. (2018). Characterization of silicon-substituted nano hydroxyapatite coating on magnesium alloy for biomaterial application. Materials Chemistry and Physics, 203: 27-33. doi: 10.1016/j.matchemphys.2017.08.020

[2] Diez, M., Kang, M.-H., Kim, S.-M., Kim, H.-E., Song, J. (2016). Hydroxyapatite (HA)/poly-L-lactic acid (PLLA) dual coating on magnesium alloy under deformation for biomedical applications. Journal of Materials Science: Materials in Medicine, 27(2): 34. doi: 10.1007/s10856-015-5643-8

[3] Bakhsheshi-Rad, H., Hamzah, E., Ismail, A., Aziz, M., Karamian, E., Iqbal, N. (2018). Bioactivity, in-vitro corrosion behavior, and antibacterial activity of silver–zeolites doped hydroxyapatite coating on magnesium alloy. Transactions of Nonferrous Metals Society of China, 28(8): 1553-1562. doi: 10.1016/S1003-6326(18)64797-1

[4] Dunne, C. F., Levy, G. K., Hakimi, O., Aghion, E., Twomey, B., Stanton, K. T. (2016). Corrosion behaviour of biodegradable magnesium alloys with hydroxyapatite coatings. Surface and Coatings Technology, 289: 37-44. doi: 10.1016/j.surfcoat.2016.01.045

[5] Yang, H., Yan, X., Ling, M., Xiong, Z., Ou, C., Lu, W. (2015). In vitro corrosion and cytocompatibility properties of nano-whisker hydroxyapatite coating on magnesium alloy for bone tissue engineering applications. International journal of molecular sciences, 16(3): 6113-6123. doi: 10.3390/ijms16036113

[6] Shen, S., Cai, S., Bao, X., Xu, P., Li, Y., Jiang, S., Xu, G. (2018). Biomimetic fluoridated hydroxyapatite coating with micron/nano-topography on magnesium alloy for orthopaedic application. Chemical Engineering Journal, 339: 7-13. doi: 10.1016/j.cej.2018.01.083

[7] Sadat-Shojai, M., Khorasani, M.-T., Dinpanah-Khoshdargi, E., Jamshidi, A. (2013). Synthesis methods for nanosized hydroxyapatite with diverse structures. Acta biomaterialia, 9(8): 7591-7621. doi: 10.1016/j.actbio.2013.04.012

[8] Sun, R., Liu, P., Zhang, R., Lv, Y., Chen, K. (2016). Hydrothermal synthesis of microstructured fluoridated hydroxyapatite coating on magnesium alloy. Surface Engineering, 32 (11): 879-884. doi: 10.1080/02670844.2016.1194511

[9] Yu, N., Cai, S., Wang, F., Zhang, F., Ling, R., Li, Y., Jiang, Y., Xu, G. (2017). Microwave assisted deposition of strontium doped hydroxyapatite coating on AZ31 magnesium alloy with enhanced mineralization ability and corrosion resistance. Ceramics International, 43(2): 2495-2503. doi: 10.1016/j.ceramint.2016.11.050

[10] Geng, Z., Cui, Z., Li, Z., Zhu, S., Liang, Y., Liu, Y., Li, X., He, X., Yu, X., Wang, R. (2016). Strontium incorporation to optimize the antibacterial and biological characteristics of silver-substituted hydroxyapatite coating. Materials Science and Engineering: C, 58: 467-477. doi: 10.1016/j.msec.2015.08.061

[11] Zhang, M., Cai, S., Shen, S., Xu, G., Li, Y., Ling, R., Wu, X. (2016). In-situ defect repairing in hydroxyapatite/phytic acid hybrid coatings on AZ31 magnesium alloy by hydrothermal treatment. Journal of Alloys and Compounds, 658: 649-656. doi: 10.1016/j.jallcom.2015.10.282

[12] Yang, H., Xia, K., Wang, T., Niu, J., Song, Y., Xiong, Z., Zheng, K., Wei, S., Lu, W. (2016). Growth, in vitro biodegradation and cytocompatibility properties of nano-hydroxyapatite coatings on biodegradable magnesium alloys. Journal of Alloys and Compounds, 672: 366-373. doi: 10.1016/j.jallcom.2016.02.156

[13] Kang, Z., Zhang, J., Niu, L. (2018). A one-step hydrothermal process to fabricate superhydrophobic hydroxyapatite coatings and determination of their properties. Surface and Coatings Technology, 334: 84-89. doi: 10.1016/j.surfcoat.2017.11.007

[14] Li, L. Y., Cui, L. Y., Liu, B., Zeng, R. C., Chen, X. B., Li, S. Q., Wang, Z. L., Han, E. H. (2019). Corrosion resistance of glucose-induced hydrothermal calcium phosphate coating on pure magnesium. Applied Surface Science, 465: 1066-1077. doi: 10.1016/j.apsusc.2018.09.203

[15] Asl, S. K. F., Nemeth, S., Tan, M. J. (2014). Hydrothermally deposited protective and bioactive coating for magnesium alloys for implant application. Surface and Coatings Technology, 258: 931-937. doi: 10.1016/j.surfcoat.2014.07.055

[16] Wang, T., Yang, G., Zhou, W., Hu, J., Jia, W., Lu, W. (2019). One-pot hydrothermal synthesis, in vitro biodegradation and biocompatibility of Sr-doped nanorod/nanowire hydroxyapatite coatings on ZK60 magnesium alloy. Journal of Alloys and Compounds, 799: 71-82. doi: 10.1016/j.jallcom.2019.05.338

[17] Kavitha, R., Ravichandran, K., Narayanan, T. S. (2018). Deposition of strontium phosphate coatings on magnesium by hydrothermal treatment: Characteristics, corrosion resistance and bioactivity. Journal of Alloys and Compounds, 745: 725-743. doi: 10.1016/j.jallcom.2018.02.200

[18] Hiromoto, S., Tomozawa, M. (2011). Hydroxyapatite coating of AZ31 magnesium alloy by a solution treatment and its corrosion behavior in NaCl solution. Surface and Coatings Technology, 205(19): 4711-4719. doi: 10.1016/j.surfcoat.2011.04.036

[19] Geng, Z., Wang, R., Zhuo, X., Li, Z., Huang, Y., Ma, L., Cui, Z., Zhu, S., Liang, Y., Liu, Y. (2017). Incorporation of silver and strontium in hydroxyapatite coating on titanium surface for enhanced antibacterial and biological properties. Materials Science and Engineering: C, 71: 852-861. doi: 10.1016/j.msec.2016.10.079

[20] Lam, W., Pan, H., Li, Z., Yang, C., Chan, W., Wong, C., Luk, K., Lu, W. (2010). Strontium-substituted calcium phosphates prepared by hydrothermal method under linoleic acid–ethanol solution. Ceramics international, 36(2): 683-688. doi: 10.1016/j.ceramint.2009.10.012

[21] Tomozawa, M., Hiromoto, S. (2011). Microstructure of hydroxyapatite-and octacalcium phosphate-coatings formed on magnesium by a hydrothermal treatment at various pH values. Acta Materialia, 59(1): 355-363. doi: 10.1016/j.actamat.2010.09.041

EUROPEAN MECHANICAL SCIENCE
e-ISSN: 2587-1110

Research Paper

Investigation of the Effects of Gasoline-Bioethanol Blends on Engine Performance and Exhaust Emissions in a Spark Ignition Engine

Savaş Yelbey[1*], Murat Ciniviz[2]

[1]Yozgat Bozok University, Vocational School of Technical Sciences, Department of Automotive Technology, Yozgat, Turkey
[2]Selcuk University, Faculty of Technology, Department of Mechanical Engineering, Konya, Turkey

Abstract

In this study; 95 octane unleaded gasoline and bioethanol were tested as fuel in a spark-ignition engine by blending bioethanol with gasoline in certain proportions (2%, 4%, 6%, 8%, 10%). Tests were carried out at five different engine loads for a constant engine speed of 2500 rpm. The variations in engine performance parameters (engine torque, engine power, brake thermal efficiency, brake specific fuel consumption, brake specific energy consumption) and exhaust emissions (exhaust gas temperature, HC, CO, CO_2 and O_2) were investigated on the basis of test fuel and engine load. According to the test results, with the increase of bioethanol ratio in the blend, brake specific fuel consumption values increased by 9.71% and brake thermal efficiency values decreased by approximately 4.97% compared to gasoline. There was decrease up to 35.56% and up to 23.77% in HC and CO emissions respectively, and an increase by 6.01% in CO_2 emissions with bioethanol addition.

Keywords: Gasoline, bioethanol, exhaust emission, engine performance

1. INTRODUCTION

Energy is one of the fundamental and driving needs of a countries economic and social development. In this respect, "Energy Security" is a vital element of economic and national security. It is an indispensable input for almost all the processes necessary to sustain our social life and used in sub-sectors such as industry, transportation, housing and commercial. Today, 86% of the energy consumption is met from fossil sources such as oil, natural gas and coal in the world. Oil, as the main energy source of the transportation sector, has the largest share in the world's primary energy consumption. Turkey is one of the significant energy consumers with its emerging economy. Oil ranks first with the rate of 31% in primary energy demand which is equal to 136.2 MTEP in 2016 and it is followed by natural gas and coal. When the distribution of Turkey's primary energy demand was examined, it was observed as follows: 25% of it in industry, 24% of it in housing and service industry, 23% of it in electricity generation, 20% of it in transportation industry [1].

The fact that most of the energy demand is met from petroleum and its derivatives, however, the depletion of oil reserves, directs humanity to long-lasting, no consumable resources. Considering the environmental impacts caused by petroleum fuels such as carbon dioxide and greenhouse gas emissions and acid rain associated with them, global warming and climate changes, the importance of alternative energy increases. The use of alternative energy sources is also inevitable for Turkey which meet the oil demand with importing 89% of it [1, 2].

The petroleum crisis at 1970s leaded many countries to searching of alternative fuels, thus the use of ethanol as a fuel has been brought to the agenda, and studies on fuel ethanol have increased rapidly day by day. In the early days, corn was used as the raw material of ethanol production because of its easy production and its ability to be converted to a high rate to alcohol [3, 4]. Today, renewable products such as sugar cane, sugar beet and cassava are the most important raw materials of ethanol. Bioethanol has same molecule with ethanol as chemically. The difference of bioethanol from ethanol is that it produces from biological feedstocks via fermentation methods. Therefore, it called bioethanol. The ethanol produces from petrochemical feedsotcks such as ethylene, calcium carbide, coal, natural gas via catalytic hydration [5-7].

Since bioethanol has similar fuel properties with gasoline, it can be used both directly and mixed with gasoline in spark plug ignition engines. In addition, the higher octane number of ethanol allows spark ignition engines to run at higher

* Corresponding authour
Email: savas.yelbey@bozok.edu.tr

European Mechanical Science (2020), 4(2): 65-71
doi: https://doi.org/10.26701/ems.635790
Received: October 22, 2019, Revised: April 16, 2020
Accepted: April 19, 2020, Published: April 25, 2020

compression ratios. Many European countries with primarily the world's largest bioethanol producers USA and Brazil, also use bioethanol as fuel [8].

The use of bioethanol as fuel causes a decrease in engine performance due to its low calorific value [9]. However, there are also many studies showing that exhaust emissions of spark ignition engines reduce by increasing the combustion quality thanks to the oxygen content of bioethanol [10, 11]. It is even stated that, thanks to its oxygen content, it increases the volumetric efficiency and thus causes an increase in the thermal efficiency values from time to time [12, 13].

Altun, Öztop [14] investigated the effects of ethanol and methanol addition (5, 10% by volume) to unleaded gasoline on performance and exhaust emissions of a spark-ignition engine. They performed their experiments at different engine speeds varied from 1000 to 4000 rpm for full throttle position. It was observed decrease in brake thermal efficiency, CO and HC emissions, while brake specific fuel consumption increased with alcohol addiction. It stated that researchers achieved best results in the case of the engine being fueled blend contain 10% methanol or ethanol at current engine design. Balki, Sayin [15] examined the use of alcohols (ethanol and methanol) on performance, emission and combustion characteristics of a single-cylinder engine by comparing unleaded gasoline. They performed the experiments at variable engine speeds for full open throttle. As a result, they stated that the use of alcohol fuels increases engine torque, instantaneous specific fuel consumption, thermal efficiency and combustion efficiency. In the case of engine being operated with alcohols, the cylinder gas pressure and heat release rate had already occurred before. It also reported that CO_2 emission increased while HC, CO and NOx emissions decreased. Najafi, Ghobadian [16] have tested the engine with E5, E7.5, E10, E12.5 and E15 gasoline-ethanol blends to investigate the performance and emission behavior of a four-cylinder, four-stroke spark ignition engine. They stated that usage of ethanol in blend increased brake torque, and brake power and improved the exhaust emissions but it decreased brake specific fuel consumption. The optimum values are obtained when engine operated at 3000 rpm engine speed with E10. Özsezen [17] used a single-cylinder spark-ignition engine with a compression ratio of 8/1 in their experimental study. Within the context of study, tests were performed at 1000, 1500, 2000 and 2500 rpm in a spark-ignition engine fueled with gasoline-ethanol (E5 and E10) blends to examine engine performance and exhaust emissions. The results of study indicated that CO and unburned HC emissions were reduced but CO_2 and NOx emissions were increased when the test engine was run with gasoline-ethanol blends. In addition, it is stated that the air-fuel ratio increased with increasing ratio of ethanol in blended fuels. Deng, Chen [18] carried out their tests in a single-cylinder, variable compression ratio spark-ignition engine operated with unleaded gasoline, pure ethanol and their blends (10% and 20%). Test conditions are as follows: five different compression ratios by of 4/1, 5.5 /1, 7/1, 8.5/1, 10/1 and full open throttle. It was found that brake average effective pressure, brake thermal efficiency and brake specific fuel consumption were higher when the fuel is gasoline-ethanol blend. They also stated that it was obtained better results for gasoline-ethanol blends compared with pure gasoline with regard to exhaust emissions. They also added the results that NOx emissions became more unstable as the compression ratio changed during the tests.

Bioethanol is a renewable alcohol with high energy value that can be produced with local sources. It is used as alternative fuel in spark plug ignition engines due to the high octane number. In this study, the effects of up to 10% bioethanol addition to gasoline on performance and emission parameters were analyzed step by step. The engine torque, power, brake specific fuel consumption, brake specific energy consumption and brake thermal efficiency values were investigated as engine performance parameters, and CO, HC, CO_2, O_2 and exhaust gas temperature values were investigated as exhaust emission characteristics. The obtained results were compared with gasoline, and have been presented as graphically.

2. MATERIAL AND METHOD

The test setup consisting of universal drive and brake unit, display panel, fuel tank, measuring tube for fuel consumption, temperature measuring device, pressure measuring device, speed measuring device, emission measuring device and a gasoline engine is shown in Figure 1. Technical specifications of the single cylinder, four stroke and air-cooled internal combustion engine are given in Table 1.

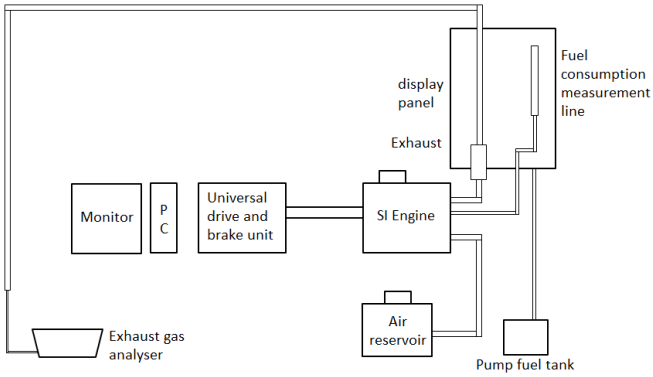

Figure 1. Experimental setup

Table 1. Specification of test engine

Engine Brand	GUNT CT152
Engine type	Four stroke, with carburettor
Cylinder number	1
Bore x Stroke, (mm x mm)	65.1 x 44.4
Cooling system	Air cooled
Compression ratio	7:1
Maximum engine power	1.2 kW
Maximum engine torque	4.5 Nm
Ignition advance	25° BTDC

Measurement ranges and accuracies of Mobydic 5000 portable gas analyzer used to measure exhaust emissions are given in Table 2.

Table 2. Specifications of the Mobydic 5000 portable gas analyzer

Measurement module	Ranges	Accuracies
CO (% vol)	0-10	0.01
CO_2 (% vol)	0-20	0.01
HC (ppm vol)	0-2000	1
NO_x (% vol)	0-5000	1
Lambda	0-5	0.001

In the experiments, 95 octane unleaded gasoline purchased from one of the gas stations and bioethanol obtained supplied from Konya Sugar Factory were used to form fuel blends, contents of which are as follows. In Table 3, some physical properties of test fuels are given.

E0: 100% unleaded gasoline

E2: 98% unleaded gasoline - 2% bioethanol

E4: 96% unleaded gasoline - 4% bioethanol

E6: 94% unleaded gasoline - 6% bioethanol

E8: 92% unleaded gasoline - 8% bioethanol

E10: 90% unleaded gasoline - 10% bioethanol

Table 3. Some physical properties of test fuels

Test fuels	Density (15°C-g/cm³)	Lower heating value (MJ/kg)	Kinematic viscosity (40°C-mm²/s)	Water content (ppm)
Bioethanol (E100)	0.78820	26.694	1.2	1093.4
Gasoline (E0)	0.72926	42.582	0.566081	-
E2	0.73198	42.131	0.576054	-
E4	0.73354	41.899	0.587451	-
E6	0.73557	41.732	0.597899	-
E8	0.73594	41.235	0.607872	-
E10	0.73809	40.901	0.617845	-

3. RESULTS

3.1. Engine Performance Parameters

Figure 2 shows changes of max torque and max power values for test fuels. The lower of calorific value of bioethanol caused a decrease both torque and power values. This decrement increased with increment of bioethanol ratio in blends. The highest decrement values have obtained by 5.77% for torque and by 6.25 for power with E10 fuel.

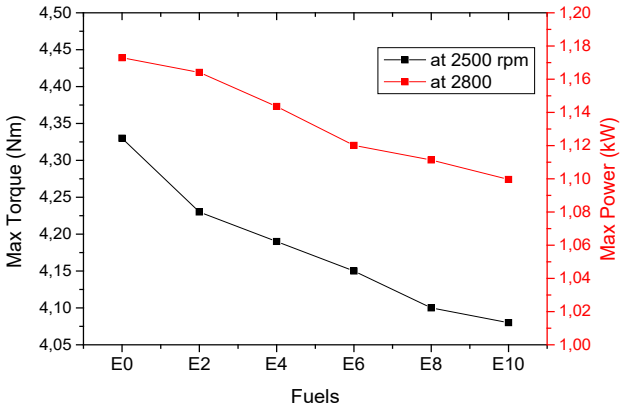

Figure 2. Maximum torque and maximum power ratings of test fuels

Brake specific fuel consumption (BSFC) is the amount of fuel, used by the engine to obtain brake power. BSFC values obtained during the tests performed at five engine loads and constant engine speed of 2500 rpm, maximum torque speed, are shown in Figure 3. As a result of the experiments, the lowest BSFC values were obtained at 2.5 Nm engine load for all test fuels. When the data obtained for all engine loads were examined, the lowest BSFC value was obtained as 525.593 g/kWh with gasoline. With the increase in bioethanol ratios in the blends, this value increased to 589.765 g/kWh with E10 fuel. The highest BSFC values for gasoline, E2 and E4 fuels are obtained at 4 Nm engine load, while the BSFC values at 4 Nm were lower than those at 2 Nm for other test fuels. This can be explained by the fact that the ideal operating range of the engine is around 2.5 Nm - 3 Nm. Load average-BSFC values are higher approximately 2.27%, 3.65%, 6.26%, 7.91% and 9.70% for E2, E4, E6, E8 and E10 respectively than that of E0. The bioethanol has lower calorific value (about 37.31%) than gasoline. This caused the lower thermal value of the E10 fuel to drop to approximately 4%. Therefore, BSFC values for bioethanol added fuels are higher than gasoline. In the literature, there are studies showing that addition of bioethanol increases BSFC unless any modification is made in the engine for similar reasons[19, 20].

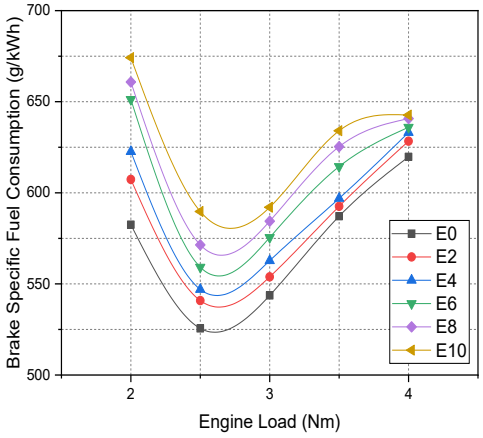

Figure 3. Variation of BSFC with engine load

Brake specific energy consumption (BSEC) is the amount of energy consumed by engine to generate unit power. The variation of BSEC with engine load and bioethanol content are shown in Figure 4. As a result of the experiments, the lowest BSEC values for all test fuels were obtained at 2.5 Nm engine load. When the data obtained for all engine loads were examined, the lowest BSEC value was obtained with gasoline as 22.381 MJ/kWh, this value reached up to 24.122 MJ/kWh for E10 fuel for the same engine load value by increasing with bioethanol rate. For gasoline, E2 and E4 fuels, the highest BSEC were obtained at 4 Nm engine load, and for other fuels BSEC are lower at 4 Nm than that of 2 Nm. This can be explained by the fact that the energy per unit power is lower in the range of 2.5 Nm to 3 Nm engine loads. For average engine loads, the increase in BSEC are approximately 1.18%, 1.99%, 4.14%, 4.49% and 5.37% for E2, E4, E6, E8 and E10 respectively with respect to gasoline. Both the increase in fuel consumption and decrease in calorific value with bioethanol addition have led to an increase in the BSEC. Zhuang and Hong [21] also reported in their studies that due to the low calorific value of bioethanol, the amount of heat ener-

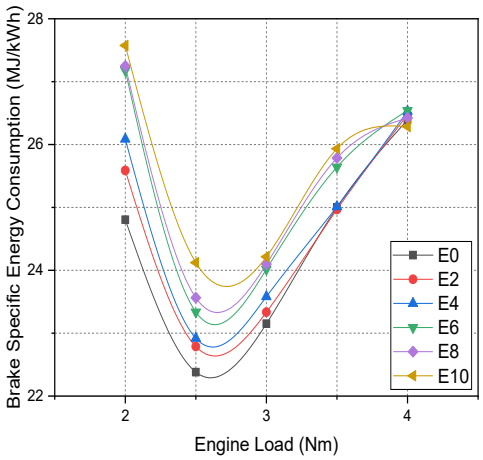

Figure 4. Variation of BSEC with engine load

gy released in the cylinder decreased and fuel consumption increased with bioethanol usage, and therefore BSEC values increased.

Figure 5 shows the variation in brake thermal efficiency (BTE), which is an expression of conversion ratio of fuel energy to brake power. As a result of the experiments, the highest BTE values were obtained with gasoline and it was observed that the BTE values decreased with increasing bioethanol ratio in the blend. For all test fuels, maximum BTE values were obtained at 2.5 Nm engine load i.e. 16.085% for gasoline and 14.924% for E10 fuel. After 2.5 Nm engine load, BTE values have started to decrease with the increase in friction losses and the amount of fuel consumed. With bioethanol usage, the decrease in BTE are approximately 1.16%, 1.92%, 3.90%, 4.21% and 4.97% for E2, E4, E6, E8 and E10 respectively. As a result of the decrease in the thermal value of the addition of bioethanol, it requires more fuel consumption per unit time in order to obtain an equal amount of brake power under the same operating conditions of engine. Due to the fact that the amount of fuel taken into the cylinders in one cycle is almost the same for all test fuels and lower heating values of the blended fuels, the amount of energy generated in the cylinder during combustion decreases, thus reduce the engine output power. Since this decreasing engine output power value is obtained with the same amount of fuel, the BTE values of the engine are also decreased in the calculations. In the literature, some researchers have reported that due to the high evaporation temperature of bioethanol in the combustion chamber cannot be achieved in the homogeneity of the mixture so the use of bioethanol decreased BTE values [22, 23].

3.2. Exhaust Emission Parameters

The exhaust gas temperature (EGT) is an important parameter in the interpretation of exhaust emission parameters and the quality of combustion within the cylinder. The variation in the EGT depending on the engine load are shown in Figure 6. By adding bioethanol to gasoline, EGT values increased up to 473.2 °C. It is the result of increasing combustion efficiency affected positively by oxygen content of bioethanol. However, Topgül [24] stated that addition of ethanol in ratios above 10% ethanol undermines the homogeneity of the mixture by the effect of high evaporation heat of it. It is also reported that increased oxygen content of the blend reduced the amount of hydrocarbon and increased combustion rate decreased the end-combustion temperature. According to the results of the experiment, with the use of bioethanol, the EGT values of E2, E4, E6, E8 and E10 fuels increased by 0.66%, 1.83%, 3.02%, 3.36% and 3.70% on average. With the increase in engine load, more fuel enters to the cylinder at the same speed, but the time required to burn it cannot be provided. Therefore, the fuel does not burn completely and the EGT decreases.

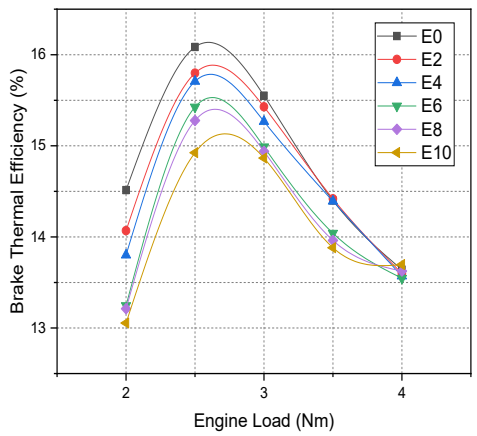

Figure 5. Variation of BTE with engine load

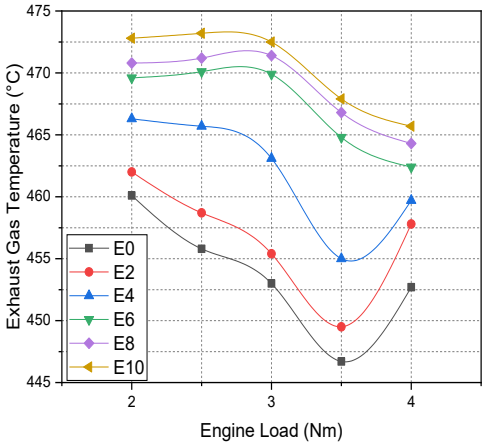

Figure 6. Variation of EGT with engine load

With the combustion of hydrocarbon-based engine fuels, H_2O_{gaz} produce as usual. However, if sufficient oxygen is not taken into the cylinder, the H atom cannot find enough O atoms for this reaction and generates HC emissions. Bioethanol allows the H atoms in the fuel to break off from the C atoms during combustion and react with oxygen to burn. Thus, the combustion approaches the completion. As shown in Figure 7, HC emission values decreased to 172 ppm with the use of bioethanol. In addition, the increase in EGT is another factor in reducing HC emissions. Increased HC emissions due to engine load are the result of reduced EGT as engine load increases. While the lowest HC emission values were obtained with E10 fuel, as the bioethanol content in the mixture increased, HC emission values decreased by 5.33%, 11.16%, 22.70%, 27.70% and 35.56% with

E2, E4, E6, E8 and E10 fuels on average. Similar results have been reported in the literature showing that bioethanol reduces HC emissions [25, 26].

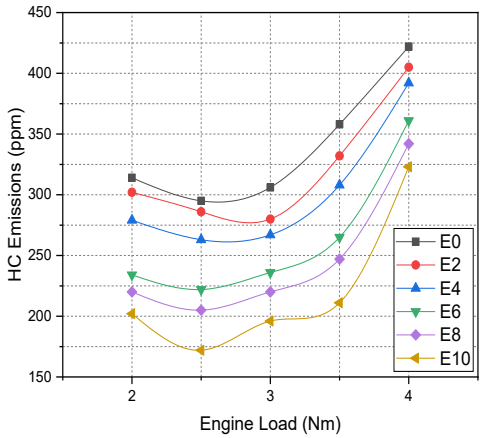

Figure 7. Variation of HC emission with engine load

Low oxygen intake to the cylinders prevents the complete combustion of the fuel and releases CO gas from the exhaust instead of CO_2, usual combustion product. The increase in engine load requires more fuel to burn in the same duration. The greater amount of fuel in the combustion chamber cannot burn faster, CO emissions increase with increasing engine load. Figure 8 shows variation of CO emission with engine load. Bioethanol supply O_2 to react CO_2 during combustion, resulting in a reduction in CO emissions. For example, CO emissions were reduced by up to 2.29% with E10 fuel compared to gasoline. Load averaged-CO emission values decreased by 7.86%, 11.71%, 22.72%, 23.77% and 26.04% on average with E2, E4, E6, E8 and E10 fuels. It has been reported by other researchers that bioethanol reduces CO emissions as it causes the fuel burn completely [10, 27, 28].

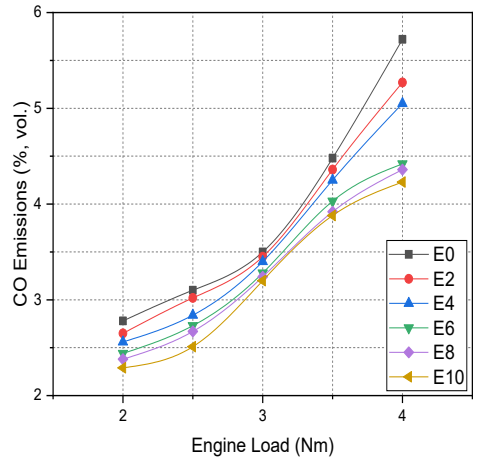

Figure 8. Variation of CO emission with engine load

Figure 9 shows the variation of CO_2 emission depending on engine load. Bioethanol has small amount of C atoms compared to gasoline. It improves the combustion efficiency, resulting as a reduction in CO_2 emissions by 6.01%. However, the lowest CO_2 emission values were obtained at 3.5 Nm engine load, where combustion efficiency was close to ideal, and CO_2 emissions were increased due to the decrease in the amount of fuel taken into the cylinder at lower engine loads and the homogeneity of the mixture due to the high evaporation temperature of bioethanol. In addition, at higher engine loads, the time for the fuel to burn was shortened, thus causing the fuel to not burn completely, causing CO emissions. These results are similar to previous studies in the literature [15, 29-31].

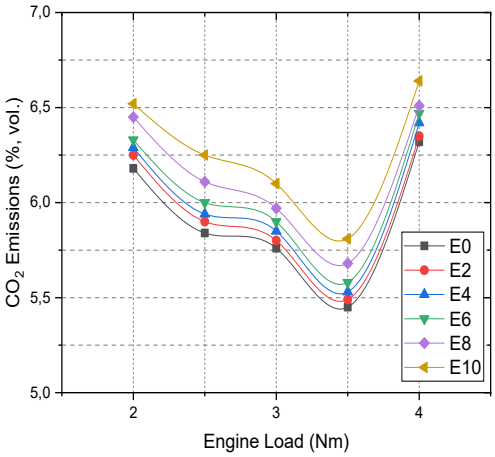

Figure 9. Variation of CO_2 emission with engine load

Variations of O_2 emission at different engine load values are given in Figure 10. The O_2 concentration depends on the oxygen/fuel ratio in the cylinders. Bioethanol contains oxygen in its chemical structure and increases the oxygen concentration of the mixture fuels made with gasoline. In this experimental study, O_2 emission values of blended fuels were higher than gasoline. The highest O_2 emission for all test fuels are found for E10 fuel as 12.03%. The variation in engine load had no significant effect on the amount of O_2 in the exhaust gas. Compared to gasoline, O_2 emission values of E2, E4, E6, E8 and E10 fuels are higher as by 1.96%, 2.48%, 11.43%, 12.03% and 22.39% respectively.

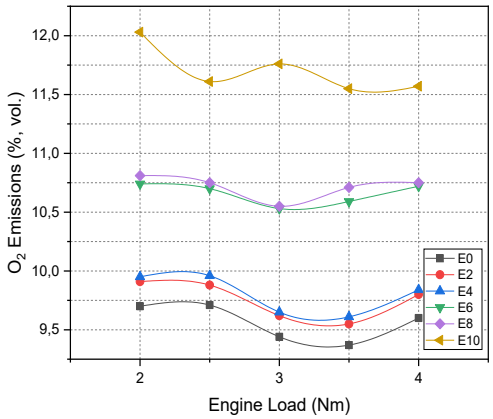

Figure 10. Variation of O_2 emission with engine load

4. CONCLUSION

In this study, engine performance and exhaust emission of a single cylinder spark ignition engine used gasoline-bioethanol blends were examined and the results were presented as follows.

- Although bioethanol produced from sugar beet has

similar fuel characteristics with gasoline, the lower heating value of it stands out as the most important parameter adversely affecting engine performance.

- Due to the fact that it has lower thermal value than gasoline and higher combustion rate due to oxygen content, bioethanol has a negative effect on performance parameters by decreasing in the effective pressure affecting the piston surface. The increase in bioethanol ratio in the blends resulted in an increase in the BSFC and BSEC values up to 9.70% and 5.37% on average, while the BTE values decreased by of 4.97%, respectively.
- Blending gasoline with bioethanol up to 10% improves the combustion efficiency, thus an increase in exhaust temperature values observed up to 3.7% compared to gasoline. It indicates that the fuel can burn more completely, thus it also reduce HC emissions.
- Bioethanol causes cleaner combustion and reduces harmful exhaust gases. Oxygen in bioethanol content reacted with H and C atoms in hydrocarbon based fuels during combustion, so it causing less HC and CO emissions by of 35.56% and 26.04%, respectively. In addition, it has a reduction in CO_2 emissions up to 6.01% as it has a lower amount of C atoms than gasoline.

In conclusion, although the addition of bioethanol to gasoline affects the engine performance parameters negatively, it is seen that this negative effect is at most 9.70%. Compared to it with improvement in exhaust emission parameters by of 35.56%, bioethanol is a convenient fuel. Furthermore, the fact that addition bioethanol by of 10% to fuel can be used without any change in engine operating parameters indicates that legal limit (4%) for addition bioethanol to gasoline can be easily increased in our country.

5. ACKNOWLEDGMENT

This study is produced from master's thesis of Savaş Yelbey. Appreciations to Selcuk University Scientific Research Projects Unit (Project No: 18201146) for its support.

6. REFERENCES

[1] TPAOGM (2018). Crude oil and natural gas sector report for 2017. General Directorate of Turkey Petroleum Corporation.

[2] Sezgin, B., Bilen, K., Çelik, V. (2013). Modification of a Diesel Engine to Natural Gas and Experimental Analysis of Modified Engine Performance and Exhaust Emission. Engineer & the Machinery Magazine, 54(642): 41-51.

[3] İlker, Ö., Ciniviz, M. (2012). Investigation On Vehicle Using Gasoline-Bioethanol Blended Fuels. International Journal of Automotive Engineering and Technologies, 1(2): 32-39.

[4] Niphadkar, S., Bagade, P., Ahmed, S. (2018). Bioethanol production: insight into past, present and future perspectives. Biofuels, 9(2): 229-238.

[5] Lavanya, A. K., Sharma, A., Choudhary, S. B., Sharma, H. K., Nain, P. K. S., Singh, S., Nain, L. (2019). Mesta (Hibiscus spp.)–a potential feedstock for bioethanol production. Energy Sources, Part A: Recovery, Utilization, and Environmental Effects, 1-14.

[6] Melikoglu, M., Albostan, A. (2011). Bioethanol production and potential of Turkey. Journal of the Faculty of Engineering and Architecture of Gazi University, 26(1): 151-160.

[7] Örs, İ. (2020). Experimental investigation of the cetane improver and bioethanol addition for the use of waste cooking oil biodiesel as an alternative fuel in diesel engines. Journal of the Brazilian Society of Mechanical Sciences and Engineering, 42(4): 1-14. doi: 10.1007/s40430-020-2270-1

[8] Costa, R. C., Sodré, J. R. (2010). Hydrous ethanol vs. gasoline-ethanol blend: Engine performance and emissions. Fuel, 89(2): 287-293.

[9] Renzi, M., Bietresato, M., & Mazzetto, F. (2016). An experimental evaluation of the performance of a SI internal combustion engine for agricultural purposes fuelled with different bioethanol blends. Energy, 115: 1069-1080.

[10] Balki, M.K., Sayin, C. (2014). The effect of compression ratio on the performance, emissions and combustion of an SI (spark ignition) engine fueled with pure ethanol, methanol and unleaded gasoline. Energy, 71: 194-201.

[11] Celik, M.B. (2008). Experimental determination of suitable ethanol–gasoline blend rate at high compression ratio for gasoline engine. Applied Thermal Engineering, 28(5-6): 396-404.

[12] Qi, D., Lee, C.-F. (2016). Combustion and emissions behaviour for ethanol–gasoline-blended fuels in a multipoint electronic fuel injection engine. International Journal of Sustainable Energy, 35(4): 323-338.

[13] Schifter, I., Diaz, L., Rodriguez, R., Gómez, J. P., Gonzalez, U. (2011). Combustion and emissions behavior for ethanol–gasoline blends in a single cylinder engine. Fuel, 90(12): 3586-3592.

[14] Altun, Ş., Öztop, H., Öner, C., Varol, Y. (2013). Exhaust emissions of methanol and ethanol-unleaded gasoline blends in a spark-ignition engine. Thermal Science, 17(1): 291–297. doi:10.2298/tsci111207034a

[15] Balki, M. K., Sayin, C., Canakci, M. (2014). The effect of different alcohol fuels on the performance, emission and combustion characteristics of a gasoline engine. Fuel, 115: 901–906. doi:10.1016/j.fuel.2012.09.020

[16] Najafi, G., Ghobadian, B., Yusaf, T., Safieddin Ardebili, S. M., Mamat, R. (2015). Optimization of performance and exhaust emission parameters of a SI (spark ignition) engine with gasoline–ethanol blended fuels using response surface methodology. Energy, 90: 1815–1829. doi:10.1016/j.energy.2015.07.004

[17] Özsezen, A.N. (2016). Evaluating Environmental Effects of Bioethanol-Gasoline Blends in Use a SI Engine. Uluslararası Yakıtlar, Yanma ve Yangın Dergisi, (4): 36-41.

[18] Deng, X., Chen, Z., Wang, X., Zhen, H., Xie, R. (2018). Exhaust noise, performance and emission characteristics of spark ignition engine fuelled with pure gasoline and hydrous ethanol gasoline blends. Case Studies in Thermal Engineering, 12: 55–63. doi:10.1016/j.csite.2018.02.004

[19] Doğan, B., Erol, D., Yaman, H., Kodanli, E. (2017). The effect of ethanol-gasoline blends on performance and exhaust emissions of a spark ignition engine through exergy analysis. Applied Thermal Engineering, 120: 433–443. doi:10.1016/j.applthermaleng.2017.04.012

[20] Koç, M., Sekmen, Y., Topgül, T., & Yücesu, H. S. (2009). The effects of ethanol–unleaded gasoline blends on engine performance and exhaust emissions in a spark-ignition engine. Renewable Energy, 34(10): 2101–2106. doi:10.1016/j.renene.2009.01.018

[21] Zhuang, Y., Hong, G. (2013). Primary investigation to leveraging effect of using ethanol fuel on reducing gasoline fuel consumption. Fuel, 105: 425–431. doi:10.1016/j.fuel.2012.09.013

[22] Kamil, M., Nazzal, I.T. (2016). Performance Evaluation of Spark Ignited Engine Fueled with Gasoline-Ethanol-Methanol Blends. Journal of Energy and Power Engineering, 10(6). doi:10.17265/1934-8975/2016.06.002

[23] Phuangwongtrakul, S., Wechsatol, W., Sethaput, T., Suktang, K., Wongwises, S. (2016). Experimental study on sparking ignition engine performance for optimal mixing ratio of ethanol–gasoline blended fuels. Applied Thermal Engineering, 100: 869–879. doi:10.1016/j.applthermaleng.2016.02.084

[24] Topgül, T., (2006). The investigation of optimum working parameters of spark ignition engines using ethyl alcohol-gasoline blend. Gazi University Graduate School of Natural and Applied Sciences.

[25] Elfasakhany, A., (2015). Investigations on the effects of ethanol–methanol–gasoline blends in a spark-ignition engine: performance and emissions analysis. Engineering Science and Technology, an International Journal, 18(4): 713-719.

[26] Hasan, A. O., Al-Rawashdeh, H., Al-Muhtaseb, A. H., Abu-jrai Ahmad, Ahmad, R., Zeaiter, J. (2018). Impact of changing combustion chamber geometry on emissions, and combustion characteristics of a single cylinder SI (spark ignition) engine fueled with ethanol/gasoline blends. Fuel, 231: 197–203. doi:10.1016/j.fuel.2018.05.045

[27] Kasmuri, N. H., Kamarudin, S. K., Abdullah, S. R. S., Hasan, H. A., Som, A. M. (2017). Process system engineering aspect of bio-alcohol fuel production from biomass via pyrolysis: An overview. Renewable and Sustainable Energy Reviews, 79: 914–923. doi:10.1016/j.rser.2017.05.182

[28] Wang, X., Chen, Z., Ni, J., Liu, S., Zhou, H. (2015). The effects of hydrous ethanol gasoline on combustion and emission characteristics of a port injection gasoline engine. Case Studies in Thermal Engineering, 6: 147–154. doi:10.1016/j.csite.2015.09.007

[29] Canakci, M., Ozsezen, A. N., Alptekin, E., Eyidogan, M. (2013). Impact of alcohol–gasoline fuel blends on the exhaust emission of an SI engine. Renewable Energy, 52: 111–117. doi:10.1016/j.renene.2012.09.062

[30] Costagliola, M. A., Prati, M. V., Florio, S., Scorletti, P., Terna, D., Iodice, P., … Senatore, A. (2016). Performances and emissions of a 4-stroke motorcycle fuelled with ethanol/gasoline blends. Fuel, 183: 470–477. doi:10.1016/j.fuel.2016.06.105

[31] Iodice, P., Langella, G., Amoresano, A. (2018). Ethanol in gasoline fuel blends: Effect on fuel consumption and engine out emissions of SI engines in cold operating conditions. Applied Thermal Engineering, 130: 1081–1089. doi:10.1016/j.applthermaleng.2017.11.090

EUROPEAN MECHANICAL SCIENCE
e-ISSN: 2587-1110

Research Paper

Performance Analysis of a Large-Scale Steam Condenser Used in a Steam Power Plant

Mehmet Tontu

Iskenderun Energy Production and Trade Company, Operation Department, 01680, Adana, Turkey

Abstract

This paper summarizes performance analysis of large-scale seawater-cooled box type condenser in a 660 MW steam power plant. Effect of seawater temperature and steam mass flow rate are investigated on the key performance parameters of steam condenser. Results indicated that improvement in the cooling water temperature generally is found favorable on the performance indicators of condenser. Condenser effectiveness improves by increasing of sea water temperature also its value enhances from 0.27 to 0.48. On the contrary TTD value decreases accordingly. On the other hand, in the case of steam flow rate changing, effectiveness and overall heat transfer coefficient almost remain constant. Effectiveness of condenser isn't found as a function of steam flow variation. Moreover, steam power plant heat rate is investigated as a function of cooling water of condenser and thus it is seen to be decreased in the result of improvement of cooling water temperature. Conversely, power plant overall thermal efficiency decreases from 39.85 % to 38.72 % due to reduction of power generation.

Keywords: Steam condenser, Condenser performance, power plant, exergy destruction, heat load

1. INTRODUCTION

Condensation is a phase changing process by withdrawing of the latent heat of evaporation [1-2]. Condensation heat transfer has a significant duty in many industrial processes, such as thermal power plant, heavy industry, cooling and, air-conditioning cycles. Various physical processes are comprised in the condensation phenomena, their relative significance depending on the conditions and implementations [3-4].

Huge type water-cooled condenser is one of the highly critical equipment of thermal and nuclear power stations. Its effectiveness has a substantial influence on the whole steam power plant's thermal performance. [5-6]. Thermal energy losses from the steam power station are primarily because of heat ejection through the condenser. The condenser in a steam power station mostly utilizes either closed-cooling water cycle from a cooling tower to transfer low-grade waste heat to the environmental or once-through water from a river, lake or sea. Since the highest amount of energy loss in the steam power station is caused by heat expel from the condenser, the heat recovery, less fuel consumption and subsequent development in the power plant performance can be accomplished by decreasing thermal energy loss from condenser by optimizing cooling water flow parameters [7-8]. However, weakness in the condenser circulating water parameters may cause an energy generation restriction due to lower vacuum pressure in the condenser. Thus, there is an essential to identify the optimal working parameters of condenser to obtain better efficiency of the thermal power stations and enhanced performance of the Rankine power cycle [9-10].

Recently, many related studies have been carried out which examine performance evaluation of steam condenser. Pattanayak et al. [9] investigated thermal performances of the steam surface condenser which is employed in the 210 MW capacity power plant. Heat transfer characteristics of condenser and its performances are examined using a modeling study by means of thermodynamic laws by changing key operating parameters of cooling water. Laskowski et al. [6] performed analysis to define performance variation of steam condenser against to upstream cooling water temperature, the cooling water mass flow rate and the steam mass flow rate. Actual data of this analysis is taken from currently running of 200 MW capacity of power stations. Steam condenser efficiency, amount of heat transfer, vacuum pressure inside the chamber, and the performance and energy generation of the LP part of the steam turbine are assessed. Masiwal et al. [11] presented off-design performance evaluation

* Corresponding authour
Email: mtontu86@gmail.com

European Mechanical Science (2020), 4(2): 72-77
doi: https://doi.org/10.26701/ems.644733
Received: November 09, 2019, Revised: February 6, 2020
Accepted: February 13, 2020, Published: April 29, 2020

and calculation methodology of a surface type condenser. Condenser performance study has been carried out for cooling water flow, cooling water inlet temperature, and air ingress/dirty tubes. In their work, all data for performance has been collected and evaluated from a 525 MW operating unit of Bharat Heavy Electricals Limited. Anozie and Odejobi [7] conducted an optimization study to estimate the optimum circulation water flow rate of a condenser. Circulating water flowrate is vitally significant to ensure the highest performance and lowest running cost of the plant. In this work, software programs were developed for modeling of a power stations at several cooling water flowrate, to identify the optimal condenser circulating water flow rate for the cycle. The investigation indicated that working condenser at a reduced circulating water flow rate of 32,000 m3/h instead of the base case scenario of 32,660 m3/h, reduced the overall heat transfer area requirement from 13,256 m2 to 8,113 m2, with the condenser making the maximum contribution to heat transfer area reduction. Harish et al [12] concentrated on improve a new model for adjusting smartly circulating seawater flow rate through condenser and illustrated of the use of this theoretical model with a given studies. Results indicated that less power consumption and better performance of power plant were provided by regulating pump speed compared to constant pump speed. Zeng at al. [13] analyzed condenser of 300 MW capacity power plant numerically in terms of the flow and heat transfer performance. Three different type tube arrangements were considered. The three typical tube arrangements were investigated to improve a unique tube arrangement model. These outcomes demonstrate that the condenser effectiveness with the new tube arrangement is significantly improved.

Box type seawater-cooled large-scale steam surface condenser is generally preferred in the steam power plants and its effectiveness considerably affects the plant electricity production as well as the performance of the unit. This study attempts to show performance and heat transfer characteristics of huge type steam condenser used in 660 MW capacity steam power plant. Characteristics of major operating parameters influencing the thermal performance of surface condenser in the steam power stations for several working conditions are examined. The effect of steam flow rate, seawater temperature and condenser vacuum pressure on heat rate and condenser performance are investigated through considering real operating data which is taken from the existing power plant. In addition to that the impact of climatic changes is shown to be important in the performance of condenser and also to compensate for the loss in plant efficiency. Climate considerations is also become even more significant particularly, seasonal transitions.

2. SYSTEM DESCRIPTION

In this analysis, the process flow taken into account is a typical 660 MW power capacity based on Rankine cycle having single reheat system with 4 low-pressure pre-heaters (LPH), 2 high-pressure pre-heaters (HPH), single flow high-pressure turbine (HPT), double-flow intermediate pressure turbine (IPT), 2 double-flow low-pressure turbines (LPT) and 2 identical condensers. Condenser is a fundamental element where the power generation by means of water-steam cycle [14]. It is a type of heat exchanger in which steam undergoes phase change by giving latent heat and converts into water. In turn, coolant water gains sensible heat. As the specific volume of steam is more than that of a specific volume of condensed water. A vacuum (negative pressure) develops in the shell side of condenser which extracts more steam from low-pressure turbine exhaust and thus creates a self-suction natural phenomenon. Condenser reduces the turbine exhaust pressure to increase the specific output of the turbine. The condenser has the function of condensing the steam exhausted from the last turbine stage to deaerate the accumulating condensate and to produce and maintain as high a vacuum as possible. Furthermore, it collects and condenses the steam produced at by-pass operation. The exhausted steam must be condensed to maintain circulation in the system. The condenser is designed for condensation at the lowest possible pressure, close to an absolute vacuum, and consequently for an increase in the usable thermal gradient in the turbine. The condenser cooling medium is seawater. To maintain the coefficient of heat transmission and to prevent deposits of corrosive substances as well as of mucous producing bacteria, the condenser tubes are continuously kept clean utilizing cleaning balls from the tube cleaning system.

The schematic of the steam condenser is as illustrated in Figure 1. The condenser is a box-type surface condenser. The box-type construction of the steam space provides optimum utilization of the enclosed volume in terms of the heat transfer surface. Circulating seawater (CW) enters the tubes, through the tube sheet and the shell side of the condenser accepts wet-steam from exit of LPT. Steam flows over the shell side and circulating water flows through the tube side. The tube sides of the two condensers are series-connected. The circulating water heats up in the first condenser, is then routed to the second condenser and passes through this in the opposite direction whereby it is heated up still further. The condensers are divided on the tube side. The tubing is divided into two halves having identical functions. Each condenser half has its inlet and outlet water boxes for the circulating water. Two separate circulating water flows are therefore routed through the tubing. Both flows are routed through the condenser in a single pass. The arrangement of the condenser tubing within the steam space has a considerable influence on the efficiency of the condenser. The objectives are as follows: To provide a uniform distribution of the steam across the entire heat transfer surface, an optimum steam velocity between the tubes and to keep the pressure difference between the topmost and bottommost row of tubes as small as possible. Nominal operating parameters of steam condenser are shown in Table 1.

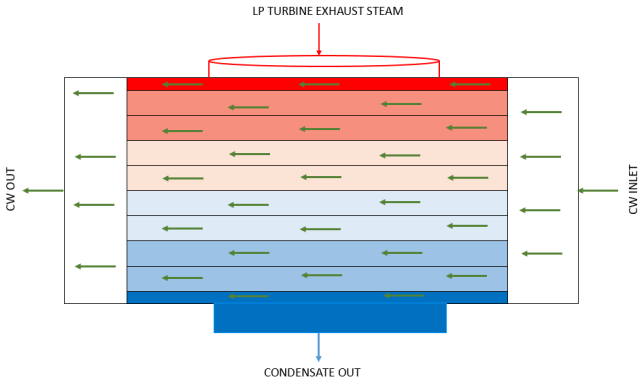

Figure 1. The schematic of the steam condenser

Table 1. Nominal operating parameters of steam condenser

Specifications	Unit	Amount
Material	----	Titanium
Surface Area	m^2	24013
Number of passes	----	1
Number of tubes	pcs	20372
Dimensions of tube	mm	28*0.5*13400
Cooling water flow rate	kg/s	29000
Cooling water temperature	°C	17-31
Steam flow rate	kg/s	180
Operation pressure	bar	0.04

3. ANALYSIS

3.1. Thermal Analysis

Amount of heat transfer of condenser can be found in three different methods: through the energy balance for water (1), steam (2) or heat transfer rate in the condenser (3). Figure 2 illustrates condensation process and temperature changes through condenser lengths. The theory of thermodynamics needs that the rate of heat transfer from the steam be equal to the rate of heat transfer to the cooling water side. Also, different methods can be performed for thermal analysis of condenser. In this study, effectiveness of the condenser is investigated based on two different ways namely, logarithmic mean temperature difference (LMTD) method and ε-NTU method [15-16].

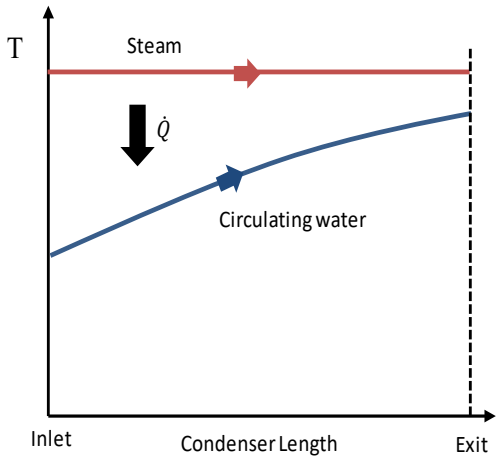

Figure 2. Condensation process and temperature changes through condenser lengths

$$\dot{Q} = \dot{m}_{cw} \times c_{p,cw} \times (T_{cw,e} - T_{cw,i}) \quad (1)$$

$$\dot{Q} = \dot{m}_s \times h_{fg} \quad (2)$$

$$\dot{Q} = U \times A \times \Delta T_m \quad (3)$$

$$TTD = T_s - T_{cw,e} \quad (4)$$

Table 2. Equations based on LMTD and –NTU methods

LMTD	ε-NTU
$\dot{Q} = U \times A \times \Delta T_m$	$\dot{Q} = \varepsilon \times C_{\min} \times (T_s - T_{cw,i})$
$\Delta T = \frac{\Delta T_1 - \Delta T_2}{\ln(\Delta T_1 / \Delta T_2)}$	$C^* = \frac{C_{\min}}{C_{\max}} = \frac{(\dot{m}c_p)_{\min}}{(\dot{m}c_p)_{\max}}$
$\Delta T_1 = T_s - T_{cw,e}$	$NTU = \frac{UA}{C_{\min}}$
$\Delta T_2 = T_s - T_{cw,i}$	$\varepsilon = 1 - \exp(-NTU)$

Condensers are generally operated for long term with without performance loss and no alteration in their working conditions. So, condensers could be designed as steady-state flow components. As such, the mass flow rate of each fluid keeps constant, and the fluid features for example, temperature and velocity at any entrance or exit remain the same. Furthermore, the fluid streams experience little or no variations in their velocities and elevations, and hence the kinetic and potential energy differences are not considered. The specific heat of a fluid, generally, is variable with temperature. But, in a specified temperature range, it can be treated as a constant at some mean value with little loss inaccuracy. Axial heat conduction along the tube is normally unimportant and can be considered negligible. Finally, the external surface of the condenser is supposed to be adiabatic, so that in order to prevent heat transfer to the ambient, and heat transfer takes place between the two medium only [16].

3.2. Exergy analysis

The exergy analysis method is well-matched for furthering the objective of using more efficient energy sources, because it allows the location, cause and size of wastes to be recognized. This information can be used to design a new energy efficient system and improve the efficiency of existing systems. This approach will provide you to understand the properties of the exergy change during the heating process and to see which components have the greatest impact on system availability [17].

To understand the quality of an energy system, the second law of thermodynamics should be considered. The entropy change in a steady-state flow stream is revealed as; the sum of the entropy generation from the exergy destruction within system boundary, the net entropy transfer through the control volume by heat transfer and entropy change by mass flow across the boundaries which are also given below [18-19]:

$$\dot{S}_{gen} = \sum_{out} \dot{m}s - \sum_{in} \dot{m}s \quad (5)$$

$$\dot{X}_d = T_0 \times \dot{S}_{gen} \quad (6)$$

The exergy equivalence at steady state situation is commonly expressed as the balance between the net exergy transfers by heat, work or mass flow through the boundaries of control volume and destructed exergy and exergy efficiency as

stated in the following [20-21]:

$$\dot{X}_d = \dot{X}_{in} - \dot{X}_{out} \quad (7)$$

4. RESULTS AND DISCUSSIONS

This study is aimed to investigate performance of one of two identical condensers. In the first case, circulating sea water cooling inlet temperature to steam condenser was improved from 17°C to 31°C, in two degree Celsius increments. The cooling water and steam mass flow rates are constant and equivalent to the nominal operating values.

The effect of the variation in the cooling water inlet temperature on the steam condenser heat rate and the exergy destruction rate are shown in Figure 3. Heat rejection to environmental linearly increases as seawater temperature increases. Heat load of condenser is the output of the combination of overall heat transfer coefficient and temperature differences between two medium therefore, heat rejection directly proportional to the seawater temperature. Conversely, exergy destruction in the condenser is positively influenced by the seawater incremental. Irreversibility in the condenser is mainly because of temperature differences between steam and seawater temperature so it is reduced with seawater enhancement. Moreover, heat rejection from condenser is thermodynamically insignificant due to heat source close to outside condition. Decline in the exergy destruction while increasing heat transfer is indicative of increased usable energy and seawater temperature increase also confirms this result.

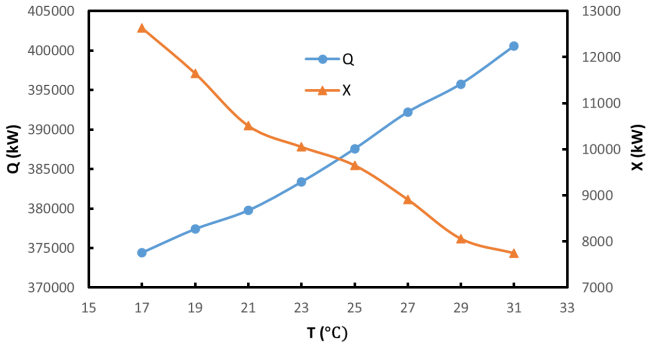

Figure 3. Variation of heat load and exergy destruction as a function of seawater temperatures

Figure 4 shows condenser TTD and effectiveness values as a function of cooling water inlet temperature. TTD is a measure of the efficiency with which heat is transferred from the steam side to the water side. A lower TTD is always better, and provides greater heat rate in the condenser and hence performance of condenser will enhance. Two main reasons for higher TTD: if there's an air removal problem, the air will collect in the condenser and reduce the effective area for the heat to transfer across the two working fluids of the exchanger. Another common reason for higher TTD occurs over a greater amount of time and isn't so instant would be heat exchanger fouling. The build up inside of the tubes can reduce cross section area as well so the fluids pass one another faster through choking and don't allow for the proper heat transfer time needed.

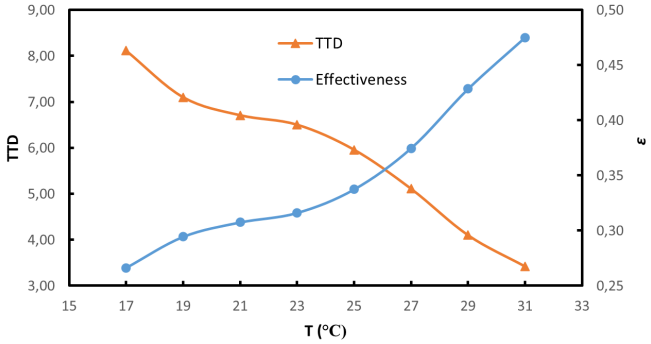

Figure 4. Condenser TTD and effectiveness values as a function of cooling water inlet temperature

Figure 5 indicates the impact of cooling water inlet temperature on condenser pressure and heat transfer coefficient. Increase in the CW temperature causes rise in the condenser pressure for a considered CW flow rate. Heat transfer coefficient enlarges with enhance in CW temperature from 17 °C to 31 °C. As obtained, the mathematical relation of CW inlet temperature with heat transfer coefficient is found to be nonlinear but quadratic in nature, whereas with condenser operating pressure the relation is exponential. Overall heat transfer coefficient increases by virtue of condenser steam temperature is enhanced as response of an increase of condenser working pressure. The pressure in the large-scale condenser is highly depend on condenser structures, the amount of latent heat to be removed, CW temperature and flow rate, maintenance of the condenser and air removal system as well as sealing system.

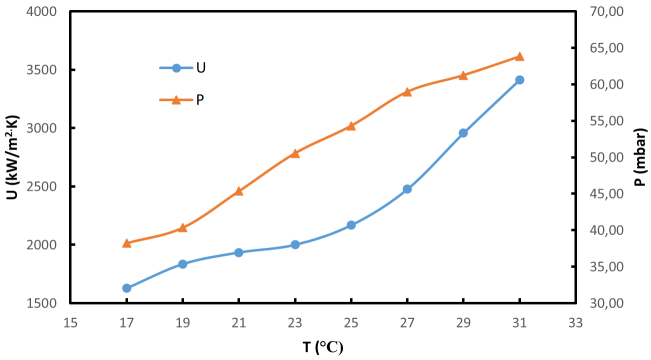

Figure 5. The relationship of cooling water inlet temperatures on condenser heat transfer coefficient and condenser pressure

Condenser cooling water inlet temperature is vital importance for both heat rate and power plant efficiencies. As it is seen from figure 6, power plant thermal efficiencies and heat rate are directly depend on CW inlet temperature variation. Higher inlet cooling water temperature causes worse condenser pressure and the power plant consumes additional coal to produce desired unit load. Condenser pressure and turbine power are negative correlated. An increase in condenser pressure leads to enthalpy rise at the outlet of the LP turbine therefore adversely affect electricity production. The enhancement in heat transfer is because of the higher steam flow required to keep target energy generation with the increase of cooling water temperature.

Table 3. Effect of steam flow variation on the condenser performance indicators

Steam flow (kg/s)	Vacum pressure (mbar)	CW inlet temp. (°C)	ΔT_r (°C)	CW Flow rate (kg/s)	Q (kW)	ε	U (kW/kg.K)	X_D (kW)	TTD (°C)
190	38.92	17	3.17	29000	385287	0.28	1667	13020	8.13
180	36.81	17	3.06	29000	371482	0.28	1613	12362	8.14
170	35.89	17	2.89	29000	351301	0.28	1673	11069	7.38
160	35.37	17	2.79	29000	338807	0.28	1690	10131	7.03
150	34.58	17	2.67	29000	323981	0.28	1663	9519	6.85
140	33.38	17	2.51	29000	304723	0.28	1646	8414	6.52

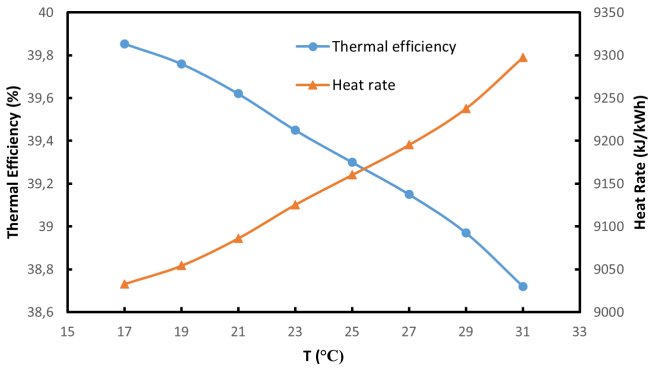

Figure 6. Effect of cooling water inlet temperature on the plant thermal efficiency and heat rate

Table 3 presents steam flow variation on the condenser performance indicators at constant CW temperature and flow rate. Steam power plant unit can vary against to load demand of dispatch center so steam inlet to condenser is changed. Heat rejection and exergy destruction decreases due to decline in the temperature of CW side resulting from steam flow reduces. Vacuum pressure is adversely affected by increasing from steam flow rate. Because, average temperature of CW temperature increase and hence condenser operating pressure is deteriorated. TTD value also decreases however, effectiveness and overall heat transfer coefficient almost remain constant. Effectiveness of condenser isn't found as a function of steam flow variation.

5. CONCLUSIONS

Condenser is the one of the most significant component of thermal power stations. The outputs and performance of steam power plant considerably depends on the condenser working criteria. This paper assessed all the aspects of condenser which affecting the performance of power plant. The dependency of cooling water temperature and steam mass flow rate with heat transfer coefficient, condenser pressure and heat transfer rate is established for a 660 MW power plant condenser. The variation in cooling water-side parameters influence the typical factors which describe the condenser performance, such as the effectiveness, the amount of heat transfer, and the condenser operating pressure, which has a substantial impact on the efficiency of condenser. Main findings are summarized as follows:

- Increase of cooling water temperature improves steam condenser performance parameters from thermal assessment point of view.
- Variation of steam flow rate doesn't affect intensely condenser performance however; steam flow rate changing directly influences exergy destruction and heat load of condenser.
- Cycle efficiency of coal-fired power plant improves with cooling water reduction of condenser since turbines converts more heat into electricity.

6. REFERENCES

[1] Strusnik, D., Golob, M., Avsec, J. (2016). Effect of non-condensable gas on heat transfer in steam turbine condenser and modelling of ejector pump system by controlling the gas extraction rate through extraction tubes. Energy Conversion and Management, 126: 228-246.

[2] Haldkar, V., Sharma, A.S, Ranjan, R.K., Bajpai, V.K. (2013). An energy analysis of condenser. International Journal of Thermal Technologies, 3: 120-125.

[3] Mirzabeygi, P. Zhang, C. (2015). Three-dimensional numerical model for the two-phase flow and heat transfer in condensers. International Journal of Heat and Mass Transfer, 81: 618-637.

[4] Mathurkar, R. D., Lawankar, Dr. S. M. (2017). Review on steam condensation heat transfer coefficient in vertical mini diameter tube. International Research Journal of Engineering and Technology, 4: 705-710.

[5] Viola, V. M., Pavkovic, B., Mrzljak. (2018). Numerical model for on-condition monitoring of condenser in coal-fired power plants. International Journal of Heat and Mass Transfer, 117: 912-923.

[6] Laskowski, R., Smyk, A., Lewandowski, J., Rusowicz, A. (2015). Cooperation of a steam condenser with a low-pressure part of a steam turbine in off-design conditions, American Journal of Energy Research, 3: 13-18.

[7] Anozie, A.N., Odejobi, O.J. (2011). The search for optimum condenser cooling water flow rate in a thermal power plant. Applied Thermal Engineering, 31: 4083-4090.

[8] Sikarwar, A.S., Dandotiya, D., Agrawal, S.K. (2013). Performance analysis of surface condenser under various operating parameters. International Research Journal of Engineering Reserarch and Aplications, 3: 416-421.

[9] Pattanayak, L., Padhi, B.N., Kodamasing, B. (2019). Thermal performance assessment of steam surface condenser. Case Studies in Thermal Engineering, 14: 100484.

[10] Nebot, E., Casanueva, J.F., Casanueva, T., Sales, D. (2007). Model for fouling deposition on power plant steam condensers cooled with seawater: Effect of water velocity and tube material. International Journal of Heat and Mass Transfer, 50: 3351-3358.

[11] Masiwal, G., Kumar, P.S., Chaudhary, S. (2017). Performance analysis of surface condenser in 525MW thermal power plant. International Research Journal of Engineering and Technology, 9: 1931-1939.

[12] Harish, R., Subhramanyan, E. E., Madhavan, R., Vidyanand, S. (2010). Theoretical model for evaluation of variable frequency drive for cooling water pumps in sea water based once through condenser cooling water systems, Applied Thermal Engineering, 30: 2051-2057.

[13] Zeng, H., Meng, J., Li, Z. (2012). Numerical study of a power plant condenser tube arrangement, Applied Thermal Engineering, 40: 294-303.

[14] Tontu, M., Bilgili, M., Sahin, B. (2018). Performance analysis of an industrial steam power plant with varying loads. International Journal of Exergy, 27(2): 231–250.

[15] Kakac, S. (1991). Boilers evaporators and condensers, John wiley & sons, Newyork.

[16] Çengel, A.Y., Ghajar, A. J. (2015). Heat and mass transfer: fundamentals & applications, Mc Graw-Hill, Newyork.

[17] Aysakhanam, D., Patel, I.J. (2014). Exergy analysis of inlet water temperature of condenser. International Research Journal of Engineering Reserarch and Aplications, 4: 249-252.

[18] Ameri, M., Ahmadi, P., Hamidi, A. (2009). Energy, exergy and exergo-economic analysis of a steam power plant: A case study. International Journal of Energy Research, 33: 499-512.

[19] Oztürk, M.M., Erbay, B. (2016). Transient exergy analysis of the condenser and evaporator of an air source heat pump water heater. Journal of Mechanics Engineering and Automation, 6: 339-347.

[20] Bilgili, M., Çardak, E., Aktaş, A. E. (2017). Thermodynamic Analysis of Bus Air Conditioner Working with Refrigerant R600a. European Mechanical Science, 1(2): 69-75.

[21] Kurtulmuş, N., Horuz, I. (2017). An industrial vapor absorption air conditioning application. Journal of Thermal Science and Technology, 37(2): 49-60.

Nomenclature

$\dot{X}$	: Exergy (kW)
$\dot{Q}$	: Heat rate (kW)
$\dot{m}$	: Mass flow rate (kg/s)
T	: Temperature (°C)
h	: Enthalpy (kJ/kg)
$\dot{S}$	: Entropy (kW)
TTD	: Terminal Temperature Difference (°C)
U	: Overall heat transfer coefficient (kW/kg.K)
P	: Pressure (mbar)
ε	: Effectiveness

Subscript

cw,i	: Circulating water inlet
cw,o	: Circulating water outlet
s	: Steam
d	: Destruction
in	: Input
out	: Output
gen	: Generation
min	: Minimum
max	: Maximum

doi: https://doi.org/10.26701/ems.644733

EUROPEAN MECHANICAL SCIENCE
e-ISSN: 2587-1110

Research Paper

Influence of Pressing Time on Physical and Mechanical Properties of Particleboards Made From Scots Pine (*Pinus sylvestris* L.)

Miglena Valyova[1*], Daniel Koynov[2]

[1]University of Forestry - Sofia, Faculty of Ecology and Landscape Architecture, Department of Plant Pathology and Chemistry, 1797 Sofia, Bulgaria
[2]University of Forestry - Sofia, Faculty of Forest Industry, Department of Mechanical Technology of Wood, 1797 Sofia, Bulgaria

Abstract

This study presents the results of investigations on some physical and mechanical properties of one-layer particleboards made from Scots pine (*Pinus sylvestris* L.). The size and the ratio of the using particles were: 0.5-1 mm- 20 %, 1-3 mm- 60 % and 3-5 mm-20 %, respectively. Urea-formaldehyde resin was used as a binder. The effect of different pressing time- 15, 30, 60 and 90 s.mm^{-1} on the some properties, such as: density, moisture content, water absorption, thickness swelling and bending strength according to appropriate standards was evaluated. The best results were observed at pressing time of 90 s.mm^{-1}. The particleboards obtained under these conditions can be used in the furniture industry.

Keywords: particleboards, urea-formaldehyde resin (UF), physical properties, pressing time

7. INTRODUCTION

Particleboards (PB) are pressed panels made out of wood particles or other lignocellulosic materials and an adhesive under pressure [1]. They possess a number of valuable properties, such as: high density, high durability, abrasion resistance, high surface hardness etc. [2; 3]. Particleboards are widely used throughout the world in the production of home and office furniture, house construction, as well as interior design elements, flooring systems, etc. [4; 5].

The forestry industry generates a considerable amount of waste, such as bark, off-cuts, slabs, rejects, etc. Many of these are small size wastes, for example sawdust and shavings obtained in the processing of solid wood materials [6]. The release of waste is a serious problem and its incorrect solving leads to an irrational utilization of the wood. On the other hand, conditions for environmental pollution are created [7; 8; 9]. In recent years, wood waste has a great application as a raw material for combustion, as well as in the production of pellets, briquettes, etc. [10].

Furthermore, the consumption of wood and products made from wood has been rapidly increasing year by year. This requires searching for more rational methods for utilization [11; 12].

There are various technological processes for the production of shredded wood composites. In addition, the assortment of manufactured products covers more than 100 types of panels and volume pressed products with different operational properties [13; 14].

The qualitative indicators of the different types of boards are regulated by the relevant standard requirements. The quality of the manufacturing particleboards depends on the influence of many factors, such as: particle density, particle size, pressing time, press temperature, type of adhesive etc. [15; 16; 17]. In this regard, the physical and mechanical properties of the boards can be improved by regulation of these factors [18; 19; 20; 21]. The objective of this research was to evaluate the effect of pressing time on some physical and mechanical properties of particleboards made from softwood.

8. MATERIAL AND METHODS

For the production of panels, particles from softwood (*Pinus sylvestris* L.) were used. The size of particles in the mixture was 0.5-1 mm- 20 %; 1-3 mm- 60 % and 3-5 mm-20 %, respectively. The target dimensions of the experimental one-layer particleboards were 500×500×8 mm. Commercial urea-formaldehyde (UF) resin (type UFR 1;"Neochim" PLC Dimitrovgrad) with solid content 70 % and hardener- 1 % ammonium chloride was used as an adhesive. The amount of the applied resin was 20 % in relation to the mixture.

After mixing of raw materials, particleboards were manu-

* Corresponding authour
Email: mvalyova@abv.bg

European Mechanical Science (2020), 4(2): 78-81
doi: https://doi.org/10.26701/ems.532796
Received: February 26, 2019, Revised: March 10, 2020
Accepted: March 17, 2020, Published: April 29, 2020

factured by pressing at temperature of 150°C, pressure of 2 MPa and pressing time of 15, 30, 60, 90 s/mm^{-1}. Four experimental boards were produced for each pressing time. Boards were conditioned at 20°C and 65 % relative humidity for five days prior to testing the following physical and mechanical properties: density, moisture content, water absorption, thickness swelling and bending strength.

The measurement of the density of the particleboards were made in accordance with BDS EN 323:2001 [22] using equation 1:

$$\rho = \frac{m}{V}, \text{ kg.m}^{-3}, \quad (1)$$

where: m is the mass of the test sample (kg); V is the volume of the test sample (m^3).

The dimensions of the test specimens for determination of density, moisture content, water absorption and thickness swelling were 50×50×8 mm.

The moisture content of the experimental particleboards was evaluated according to BDS EN 326-1:2001 [23]. It was calculated using equation 2:

$$H = \frac{m_H - m_0}{m_0}.100,\%, \quad (2)$$

where: $m_н$ is the initial mass of the test sample (g), m_0 is the mass of the test sample after drying (g).

The water absorption of the particleboards was measured in accordance with BDS EN 317:1993 (equation 3) [24]:

$$\Delta_W = \frac{m_2 - m_1}{m_1}.100\,, \% \quad (3)$$

where: m_1 is the mass of the test sample before immersion in water (g), m_2 is the mass of the test sample after immersion in water (g).

The thickness swelling was determined in accordance with BDS EN 317:1993, using the following equation:

$$G_t = \frac{t_2 - t_1}{t_1}.100\,, \% \quad (4)$$

where: t_1 is the thickness of the test sample before immersion in water (mm), t_2 is the thickness of the test sample after immersion in water (mm).

The bending strength test was carried out according to BDS EN 310:1999 [25]. Eight specimens for each pressing time with dimensions 200×50×8 mm were prepared. The calculations were based on the equation 5:

$$f_m = \frac{3F_{\max}.l_1}{2bt^2}, \text{ N.mm}^{-2} \quad (5)$$

where: F_{max} is the failure load (N), l_1 is the distance between the centers of the supports (mm), b is the width of the test sample (mm), t is the thickness of the test sample (mm).

The results were calculated based on statistical methods and the following parameters were determined: average arithmetical values ($\overline{X}$), average quadratic diversion (S_x), average error (m_x) and index of accuracy (p_x).

9. RESULTS AND DISCUSSION

The effect of pressing time on the density is shown in Fig. 1. According to data, the increasing of pressing time leads to increase the density of particleboards. The values obtained ranged from 672 to 953 kg.m^{-3}.

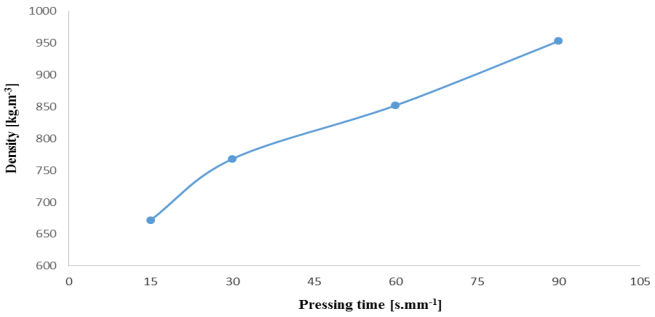

Figure 1. Density of particleboards depending on the pressing time

The highest density (953 kg.m^{-3}) was obtained at samples with a pressing time of 90 s.mm^{-1}. The density has a significant effect on the other properties of particleboards. The increase of pressing time leads to an increase in the density of the pressed panels. This is due to the compaction of the wood under pressure and temperature, especially the facial layers that are in contact with the hot press.

The results from determining the moisture content of the experimentally obtained panels are given in Fig. 2. This indicator progressively increases with an increase in the pressing time- from 6.90% (at 15 s.mm^{-1}) to 7.60% (at 90 s.mm^{-1}). In this assay, the moisture content of the source wood was 7.75% and that of the particleboards was 7.65%, respectively.

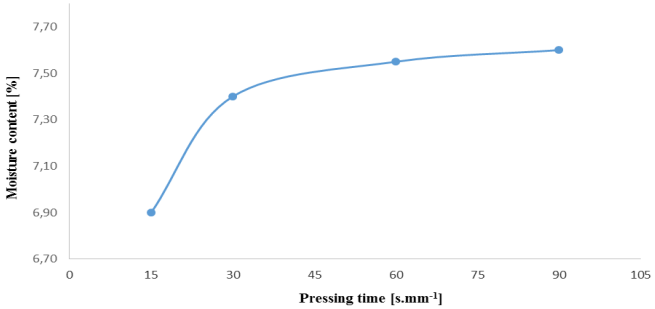

Figure 2. Moisture content of particleboards depending on pressing time

Table 1 summarizes the obtained results of water absorption depending on pressing time. As can be seen from data, the particleboards obtained at pressing time of 60 s.mm^{-1} had greater water absorption in comparison to these obtained at pressing time of 90 s.mm^{-1}. The latter had about fifteen times lower values and they possess better water resistance.

Table 1. Water absorption of particleboards depending on the pressing time

Pressing time (s.mm^{-1})	$\overline{X}$ (%)	S_x (%)	m_x (%)	p_x (%)	n
60	77.66	0.64	0.20	0.26	32
90	5.34	0.18	0.06	1.07	32

*n- number of samples

The samples obtained at pressing time of 15 and 30 s.mm^{-1} did not show any water resistance because of their destruction. Similar results were established also for thickness swelling. At pressing times of 15 and 30 s.mm^{-1}, the wood particles do not compress enough. In general, the time is insufficient for their compaction and adhesion. For this reason, the obtained panels were destroyed at removing from the press. This in turn led to the inability to determine their water resistance.

The average values at investigation of thickness swelling are given in Table 2. It includes data from evaluation of particleboards at pressing time of 60 and 90 s.mm^{-1}, respectively. A better value showed panels with a pressing time of 90 s.mm^{-1}.

Table 2. Effect of pressing time on the thickness swelling of particleboards

Pressing time (s.mm^{-1})	$\overline{X}$ (%)	S_x (%)	m_x (%)	p_x (%)	n
60	60.06	3.29	1.04	1.73	32
90	4.95	0.31	0.098	1.97	32

*n- number of samples

The effects of pressing time on the bending strength of particleboards are shown in Fig. 3.

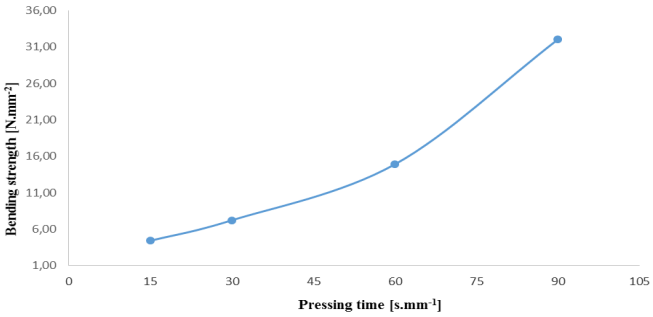

Figure 3. Bending strength of particleboards depending on pressing time

The bending strength of boards increases from 4.41 to 32.06 N.mm^{-2} or about 7 times with an increase in the pressing time from 15 to 90 s.mm^{-1}. The bending strength of panels obtained at pressing time of 90 s.mm^{-1} was about four times better than these obtained at pressing time of 30 s.mm^{-1}. The highest value was found at pressing time of 60 (14.91 N.mm^{-2}) and 90 s.mm^{-1} (32.06 N.mm^{-2}), respectively.

The bending strength increased with increase in the density of the wood due to the pressure and temperature during the pressing. The tree species with higher density are characterized with greater bending strength. The latter property affects the production of the wood based panel products.

10. CONCLUSIONS

In this research some physical and mechanical properties of one layer particleboards produced from Scots pine were determined according to the standards. The following conclusions can be drawn from the obtained results presented above:

1. The greatest density was established for particleboards at pressing time 90 s.mm^{-1}.

2. For just one parameter, bending strength, one highest value was obtained at pressing time 90 s.mm^{-1}.

Therefore, these panels can be used as a construction material in the furniture industry.

3. The lowest values for physical properties water absorption and thickness swelling at pressing time of 90 s.mm^{-1} were determined. For this reason, these panels are characterized by the best water resistance.

11. REFERENCES

[1] Sellers, T. (2000). Growing markets for engineered products spurs research. Wood Technology, 127 (3): 40–43.

[2] Taş, H. H., Sevinçli, Y. (2015). Properties of Particleboard Produced from Red Pine (Pinus brutia) Chips and Lavender Stems. BioResources, 10(4). doi:10.15376/biores.10.4.7865-7876

[3] Maloney, T. M. (1993). Modern particleboard and dry process fiberboard manufacturing. Miller Freeman Publ, San Francisco.

[4] Wang, D., Sun, X. S. (2002). Low density particleboard from wheat straw and corn pith. Industrial Crops and Products, 15 (1): 43-50. doi: 10.1016/S0926-6690(01)00094-2.

[5] Kord, B., Roohani, M., Kord, B. (2015). Characterization and utilization of reed stem as alignocellulosic resource for particleboard production. Maderas. Ciencia y tecnología, 17 (3): 517-524. doi: 10.4067/S0718-221X2015005000046.

[6] Valarelli, I., Battistelle, R., Bueno, M., Bezerra, B., Campos, C., Alves, M. (2014). Physical and mechanical properties of particleboard bamboo waste bonded with urea formaldehyde and castor oil based adhesive. Revista Matéria, 19 (1): 1-6. doi: 10.1590/S1517-70762014000100002.

[7] Merrild, H., Christensen, T. H. (2009). Recycling of wood for particle board production: accounting of greenhouse gases and global warming contributions. Waste Management & Research, 27 (8): 781-788. doi: 10.1177/0734242X09349418.

[8] Ganne-Chédeville, C., Diederichs, S. (2015). Potential Environmental Benefits of Ultralight Particleboards with Biobased Foam Cores. International Journal of Polymer Science, 2015: 1–14. doi:10.1155/2015/383279

[9] Németh, G. (2009). Handling and recycling of waste in wood industry, Ph.D. Thesis, University of West Hungary.

[10] Kamikawa, D., Kuroda, K., Inoue, M., Kubo, S., Yoshida, T. (2009). Evaluation of combustion properties of wood pellets using a cone calorimeter. Journal of Wood Science, 55 (6): 453–457. doi: 10.1007/s10086-009-1061-1.

[11] Melo, R. R., Stangerlin, D. M., Santana, R. R. C., Pedrosa, T. D. (2014). Physical and mechanical properties of particleboard manufactured from wood, bamboo and rice husk. Materials Research, 17 (3): 682-686. doi: 10.1590/S1516-14392014005000052.

[12] Palo, M., Uusivuori, J. (2012). World forests, society and environment. Springer Science & Business Media.

[13] Skog, K., Ince, P., Dietzman, D., Ingram, C. (1995). Wood products technology trends. Changing the face of forestry. Journal of Forestry, 93 (12): 30-33.

[14] Tabarsa, T., Khanjanzadeh, H., Pirayesh, H. (2011). Key Engineering Materials, 471-472: 62-66. doi: 10.4028/www.scientific.net/KEM.471-472.62.

[15] Antonovic, A., Jambrekovic, V., Kljak, J., Spanic, N., Medved, S. (2010). Influence of urea-formaldehyde resin modification with liquefied wood on particleboard properties. Drvna Industrija, 61 (1): 5-14.

[16] Oliveira, S. L., Mendes, R. F., Mendes, L. M., Freire, T. P. (2016). Particleboard panels made from sugarcane bagasse: characterization for use in the furniture industry. Materials Research, 19 (4): 914-922. doi: 10.1590/1980-5373-MR-2015-0211.

[17] Savov, V. (2014). Effect of temperature and duration of hot-pressing on main properties of light MDF. Woodworking industry and furniture manufacturing, 1: 34-39, Sofia. ISSN 1311-4972.

[18] Muruganandam, L., Ranjitha, J., Harshavardhan, A. (2016). A review report on physical and mechanical properties of particle boards from organic waste. International Journal of ChemTech Research, 9 (1): 64-72, ISSN: 0974-4290.

[19] Candan, Z., Akbulut, T. (2015). Physical and mechanical properties of nanoreinforced particleboards composites. Maderas Ciencia y Tecnología, 17 (2): 319 – 334. doi: 10.4067/S0718-221X2015005000030.

[20] Batiancela, M. A., Acda, M. N., Cabangon, R. J. (2014). Particleboard from waste tea leaves and wood particles. Journal of Composite Materials, 48 (8): 911-916. doi: 10.1177/0021998313480196.

[21] Taghiyari, H. R., Rangavar, H., Bibalan, O. F. (2011). Effect of nano-silver on reduction of hot pressing time and improvement in physical and mechanical properties of particleboard. BioResources, 6 (4): 4067-4075.

[22] BDS EN 323: 2001 "Wood-based panels - Determination of density".

[23] BDS EN 326-1: 2001 "Wood-based panels - Sampling, cutting and inspection - Part 1: Sampling and cutting of test pieces and expression of test results".

[24] BDS EN 317:1993 "Particleboards and fibreboards. Determination of swelling in thickness after immersion in water".

[25] BDS EN 310:1999 "Wood-based panels - Determination of modulus of elasticity in bending and of bending strength".

EUROPEAN MECHANICAL SCIENCE
e-ISSN: 2587-1110

Research Paper

The Dispersion Energy Parameters, Linear and Nonlinear Optical Properties of Transparent Mn:ZnO Nanolayers

Cihat Aydin

[1]Mersin University, Faculty of Engineering, Metallurgy and Materials Engineering Department, Mersin, Turkey

Abstract

Throughout this research, the impact of Manganese doping on the optical characteristics of ZnO nanolayers was explained. The sol-gel spin coating technique has significant advantages due to the mixing of components on the atomic scale and provides excellent control over the composition that was employed to produce samples. The optical characteristics of Mn: ZnO nanolayers, were determined with the help of UV-VIS-NIR spectroscopy. The linear and nonlinear optical properties of nanolayers were investigated between 300 and 800 nm wavelengths. The dispersion properties of the samples were determined and interpreted in accordance with the single-oscillator model. The third-order nonlinear optical characteristics indicate a good correlation between theoretical and experimental results. These interesting results obtained by Mn-doping of ZnO showed a significant behavior for technological applications in electronic, optoelectronic devices and nonlinear optical applications.

Keywords: Nonlinear optics, Opto-electrical properties, dispersion energy parameters, optical band gap

12. INTRODUCTION

Due to their unique properties, optical thin films have been widely used in the automotive industry, medical equipment, communication, computers, optoelectronics, spintronics, biomaterials, energy conversion, data storage, and even architecture [1]. ZnO draws great interest as a transparent conductive material because of its high optical transparency in the visible light region [2]. Therefore, ZnO is a suitable material for electronic and optical devices [3]. Furthermore, ZnO offers unique photocatalytic properties[4].

Bandwidth engineering research has been recently accelerated to improve the characteristics of semiconductors with wide bandwidths [5]. Therefore, comprehensive research has been conducted for the purpose of changing the characteristics of zinc oxide for various applications [6]. Developments in the synthesis of high-quality ZnO nanostructures allow the production of semiconductors, especially those used in nanoscale device applications [7]. The production of new semiconductors has been renovated with the development of semiconductor devices in science and industry.

In the present research, nanostructured doped and pure ZnO films produced by the spin coating technique. Also, the variation of linear and nonlinear optical properties by the Mn doping concentrations of ZnO nanolayers thin films were studied.

13. 2. EXPERIMENTALS

In this study, All chemicals were provided by Merck and analytical purity was protected. The solutions were quantified as 0.5 M, 5 ml, and the contents were put into test tubes containing solvent (2-methoxyethanol). These solutions were stirred at room temperature using a magnetic stirrer and an ultrasonic stirrer. Stirring was repeated under the same conditions after the dopant source was added. Finally, the stabilizer (Monoethanolamine) was added and stirring was repeated under the same conditions. Stirring was carried out in a magnetic stirrer (2h at 60 °C) to obtain a homogeneous gel from the solution. The microscope glasses were respectively ultrasonic cleaned in ethyl alcohol, acetone and pure water for 15 minutes and completely with the help of nitrogen gas. The growth of thin films was accomplished with the help of a spin coating devices(1500 rpm, 20 seconds). For drying, the substrates were held on a heater pre-set to 150 °C for 10 minutes. In the final step, the obtained films were heat-treated at 550 °C for 2 hour. Care was taken to prepare thin films under the same conditions for all doping ratios. Absorption T(λ), reflectance R(λ) and permeability A(λ) measurements of the prepared nanolayers were obtained with a spectrophotometer (Shimadzu UV-VIS-NIR 3600) in the wavelength range of 300 nm-800 nm. All measurements were made at room temperature.

* Corresponding authour
Email: cihataydin@mersin.edu.tr

European Mechanical Science (2020), 4(2): 82-89
doi: https://doi.org/10.26701/ems.710165
Received: March 27, 2019, Revised: April 1, 2020
Accepted: April 4, 2020, Published: April 29, 2020

14. RESULTS AND DISCUSSION

14.1. 3.2. Optical properties of pure and Mn-doped ZnO nanostructured films

The change in the absorption properties of pure and Mn-doped ZnO film samples at room temperature is shown in Fig.1. Upon examining Fig. 1, it is possible to say that the specific absorption properties of ZnO are significantly affected by Mn-doping. All samples have the ultraviolet absorption edges ranging from 300 - 400 nm. Depending on the Mn-doping ratio, the absorption value also increased. This increase is thought to have resulted from further absorption of photons because of the introduction of Mn-defects into the forbidden band [8,9]. The absorption spectrum of pure and Mn-doped ZnO thin films showed strong absorption properties in the wavelengths of 400 nm and lower, and a continuous increase in absorption was determined. However, absorption reaches an equilibrium value since the samples exhibit permeability in the wavelengths ranges equal to or greater than 400 nm [10,11]. The possible reason for the sharp absorption peak at about 300 nm for the samples may be the photostimulation of electrons from the valence band to the conduction band [12,13,14]. With Mn-doping, this absorption edge shifts to higher wavelengths. It is noteworthy that the pure ZnO sample has the lowest absorbance in the visible spectrum range because it is receiving high-energy photons, causing the activation of *sp-d* exchange interactions and typical *d-d* transitions [15]. This has been similarly stated in previous research [16].

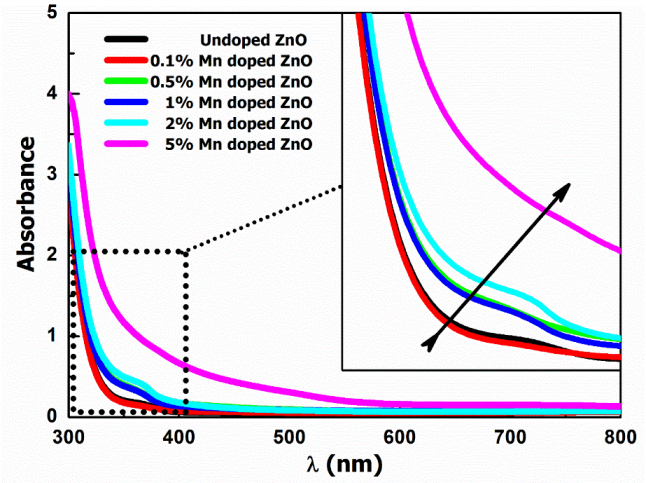

Figure 1. Absorbance spectra of the Mn: ZnO nanolayers

Fig. 2 demonstrates the reflection spectra of pure and Mn-doped ZnO nanolayers. As observed in Fig. 6, the reflection curves of the nanolayers demonstrated a peak in the wavelength of about 390 nm. The peak in question changes according to Mn-doping. This proves that the forbidden energy ranges of films vary with Mn-doping. This Mn doping leads to reduce the reflection values of the nanolayers compared to the pure ZnO film sample. The reduction of reflection by Mn-doping has been previously reported and such detail is in well agreement with our result [17]. The possible reason for the alteration in optical reflection can be the morphological alteration in films since the aspect ratio of crystallites changes according to the film thickness. This has been similarly stated for ZnO thin layers produced using several deposition routes[18]. Moreover, an increase occurred in the reflection values as they shifted to short wavelengths. This can be attributed to the back reflection of photons as a result of their higher interaction with electrons, atoms, or crystal molecules due to their increased energy.

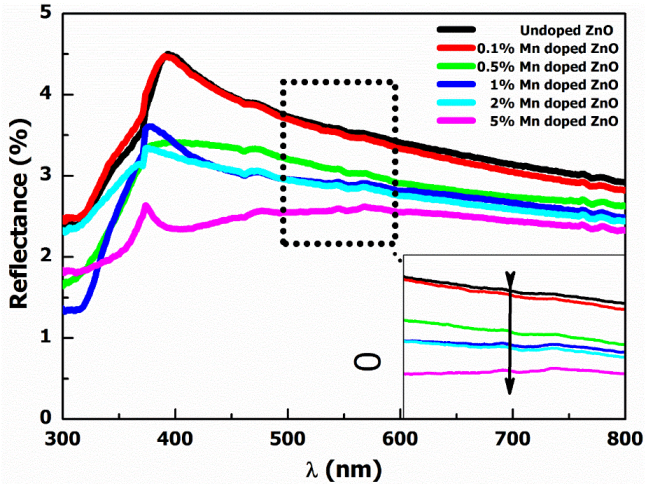

Figure 2. Reflectance spectra of the Mn: ZnO transparent nanolayers

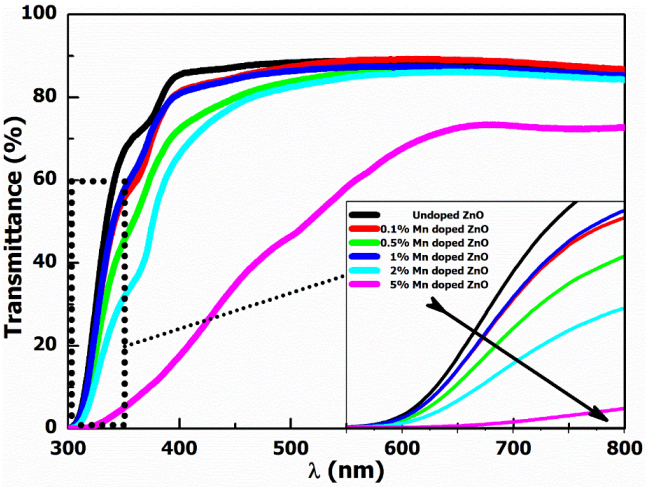

Figure 3. Transmittance spectra of the Mn: ZnO transparent nanolayers

The optical transmission spectra of pure and Mn-doped ZnO films that were recorded in the wavelength range of 300-800 nm are presented in Fig. 3. The prepared samples demonstrate high transparency in the visible range, and the transmission values decrease because of Mn-doping in all samples. The reduction in optical transmission is associated with the light loss caused by the structural properties of films, oxygen gaps, and dispersion in the grain boundaries [19] because the transmission of films, in general, depends on the surface morphology and structure [20]. The main cause of the loss of transmission observed due to increased Mn-contents in ZnO thin films may be deterioration of crystal quality of samples, increase in the defect density with the increasing doping ratio [21], and the presence of dispersion centers [22]. As the Mn-ratio increased, the transmission decreased as the optical dispersions increased. The trans-

mission spectrum of the thin films presented in Fig. 3 shows a sharp absorption edge in the wavelength range of 300-350 nm. This band edge shifts towards high wavelengths in parallel with increasing Mn- concentrations. This proves the successful incorporation of Mn-ions into the ZnO matrix. The possible reason for this is the low UV light absorption due to the increasing Mn-ratio [23]. This has been confirmed by similar results from many studies in the literature on doped and pure ZnO thin films [24].

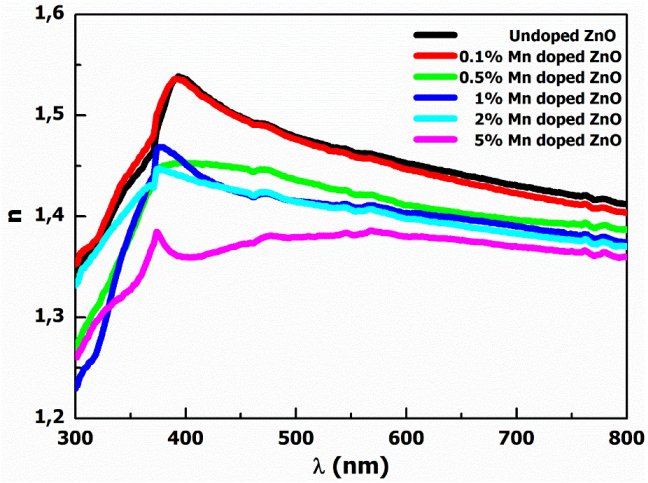

Figure 4. *n* (Refractive index) spectra of Mn:ZnO nanolayers

Finding the refractive index of semiconductor materials takes a significant part in identifying the suitable usage area by taking advantage of the optical characteristics of the material. In the design of the device, the refractive index represents the key parameter in the integrated optical devices, including switches, modulators, filters, etc. The refractive index can be adapted to any value that is needed for use in filters through the doping concentrations. The *n* and *k* values of the nanostructured thin films generated with the sol-gel technique were found from the transmittance and reflectance spectra.

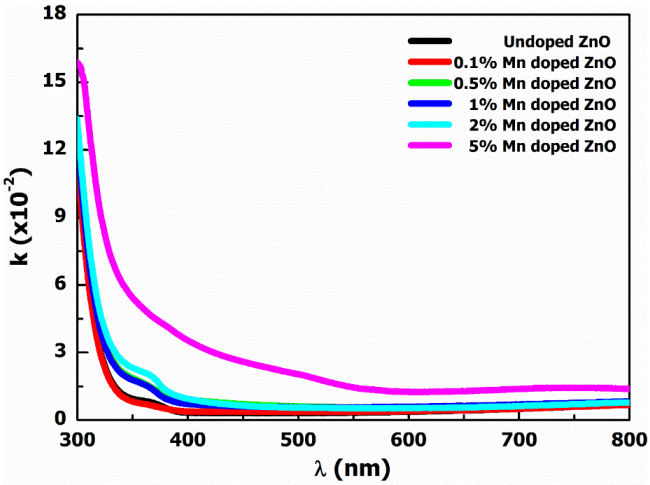

Figure 5. *k* (Absorption index) spectra of Mn:ZnO nanolayers

Refractive index and absorption index values of produced nanolayers by Sol-Gel technique were found with the help of tranmission and reflection curves.

In accordance with the analysis introduced by Moss, the absorption coefficient α was calculated from the measurements of $T(\lambda)$ and $R(\lambda)$ using the equation presented below [9]:

$$T = \frac{\left[(1-R)^2 \exp(-\alpha d)\right]}{\left[(1-R)^2 \exp(-2\alpha d)\right]} \quad (1)$$

$$R = \frac{(n-1)^2 + k^2}{(n+1)^2 + k^2} \quad (2)$$

It is possible to analyze these spectra for the purpose of determining optical constants, including refractive index (n) and damping coefficient (k). The correlation below can represent the complex refractive index of ZnO-based thin films [9]:

$$\check{n} = n(\lambda) + ik(\lambda) \quad (3)$$

where n refers to the real part, and k refers to the imaginary part of the complex refractive index. With the help of the reflection values of Mn: ZnO thin film samples, the refractive index (n) is computed by the following formula that is called Fresnel's formula [10]:

$$n = \frac{(1+R)\sqrt{4R - (1-R)^2 k^2}}{1-R} \quad (4)$$

It is possible to use the formula presented below for the purpose of obtaining the absorption index (k) [11]:

$$k = \frac{\alpha\lambda}{4\pi} \quad (5)$$

where λ is the wavelength and α is the absorption coefficient. The change in the n and k values can be calculated by using Fresnel's equations against wavelengths are demonstrated in Fig. 4 and Fig. 5, respectively. As can be observed from Fig. 4, with generally increasing incident wavelength, the refractive index value first increased and then decreased. The pure ZnO sample showed the highest refractive index. A non-linear decrease is observed in the refractive index values with Mn-doping in the ZnO matrix. The refractive index comprises two regions for all studied samples. The first one is lower wavelengths (abnormal dispersion) where an increase occurs in the refractive index with increasing wavelength, and the second one is the region where a decrease occurs in the refractive index (normal dispersion) with an increase in wavelength [9]. This abnormal dispersion determined in the refractive index in the lower wavelength region is due to the resonance impact between electromagnetic radiation and electron polarization by adding Mn-ions into the ZnO structure [13], which in turn causes the binding of electrons to the oscillating electric field. Likewise, it is possible to explain the decreasing tendency in higher wavelengths by the effect of band levels. Gradually decreasing n and k values result from increasing carrier concentrations as a consequence of changing the chemical composition of samples by doping. The findings in question have been similarly stated for ZnO nanomaterials [25]. The refractive index (n) of the undoped and Mn-doped ZnO nanostructured thin films at different wavelength are demonstrated in Table 1.

Table 1. *n* (Refractive index) of the Mn: ZnO nanolayers at different wavelength

Samples	The refractive index (n)		
	at 300 nm	500 at nm	700 at nm
Pure ZnO	1,3472	1,4787	1,4306
0.1% Mn doped ZnO	1,3545	1,4763	1,4229
0.5 % Mn doped ZnO	1,2646	1,4360	1,3966
1 % Mn doped ZnO	1,2295	1,4152	1,3901
2 % Mn doped ZnO	1,3319	1,4146	1,3826
5 % Mn doped ZnO	1,2616	1,3793	1,3702

The forbidden energy gap of the semiconductor thin films generated was found from the $(\alpha h\upsilon)^2$-$h\upsilon$ graph by utilizing the basic absorption spectrum. The energy gap value of the point at which the linear section of the mentioned change intersects the $h\upsilon$ axis at $(\alpha h\upsilon)^2 = 0$ gives the forbidden energy band gap of the studied semiconductor. The formula presented below and known as Tauc's equation was utilized to calculate the forbidden energy band gap as follows [26]:

$$(\alpha h\upsilon)^2 = A(h\upsilon - E_g) \quad (6)$$

where α refers to the absorption coefficient, $h\upsilon$ refers to the photon energy, E_g refers to the forbidden bandgap, and A refers to the constant. The $(\alpha h\upsilon)^2$-$h\upsilon$ plots to determine the forbidden energy gap of pure/Mn-doped nanostructured ZnO thin films are demonstrated in Fig. 6.

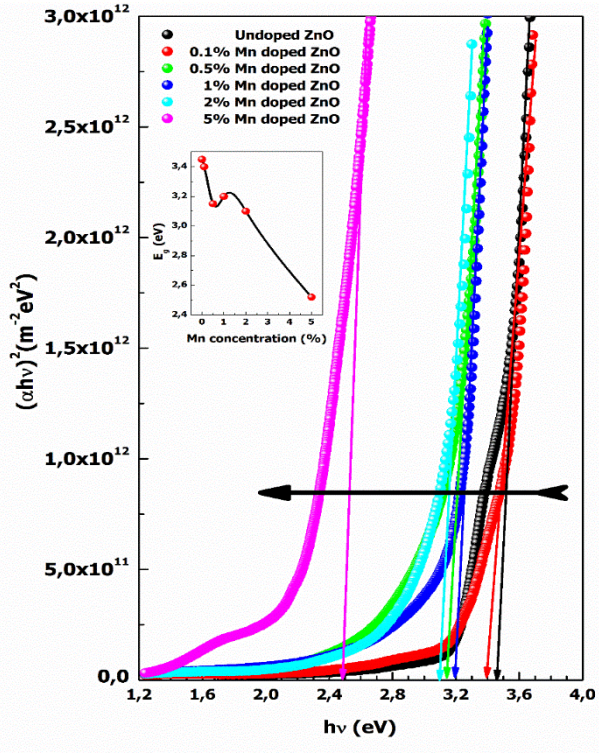

Figure 6. Tauc's *plots* of the Mn: ZnO nanolayers

With the help of these curves, the forbidden energy gaps (E_g) of the understudied samples were calculated and are presented in Table 2. The change in the energy gap with Mn-concentrations is given in Fig. 6. It is observed that the highest value of the energy gap belongs to the pure ZnO sample and the lowest value belongs to 5% Mn-doped ZnO film sample. The obtained findings on the energy gap are in compliance with the bulk ZnO (3.37 eV)) [10] and ZnO samples generated by similar methods in the literature [27]. The energy gap of the samples generally decreased with the increasing Mn-ratio. There may be two reasons for the decreasing optical band gaps of Mn-doped ZnO thin films. In other words, there is an inverse proportion of the forbidden energy gap to the size change because the size of doped Mn-grains is much smaller than the excitonic Bohr's radius in ZnO. Substituting both Mn-atoms and Mn- in the interstitial position with Zn-can lead to a lattice distortion [3]. Therefore, structural distortion and irregularity in the ZnO lattice may produce a change in the optical bandgap of Mn-doped ZnO films. Since the optical band gap is associated with the lattice constant [28], the latter may be attributed to the modification of the band structure due to the exchange interactions between sp-d electrons in ZnO [29]. This type of change interaction is caused by the reinforcement that causes the bandgap to be reduced by decreasing the bottom of the conduction band and increasing the top of the valence band . The narrowing of the ZnO bandgap with doping has been observed in a similar way in the previous research [30],[31],[32].

Table 2. Optical band gap of present work on ZnO nanolayers

	E_g (eV)
Pure ZnO	3.45
0.1% Mn doped ZnO	3.40
0.5 % Mn doped ZnO	3.15
1 % Mn doped ZnO	3.20
2 % Mn doped ZnO	3.10
5 % Mn doped ZnO	2.52

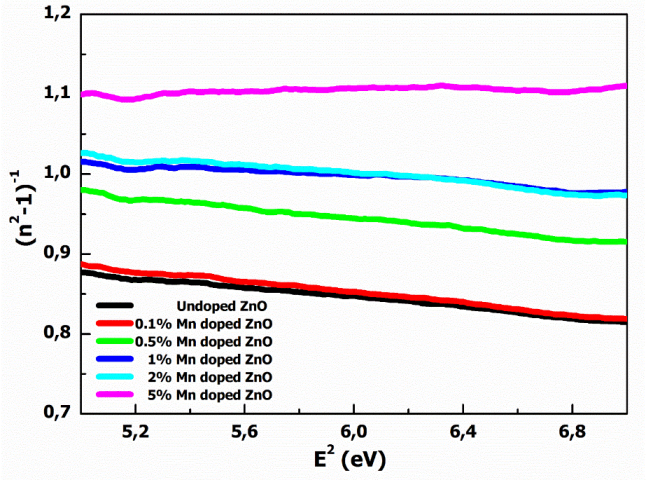

Figure 7. Plots of $(n^2\text{-}1)^{-1}$ - $(h\upsilon)^2$ of the Mn: ZnO nanolayers.

Refractive dispersion takes a significant part in investigating the optical properties of materials since it represents an essential factor for designing devices that will be utilized for image distribution in optical communications. The refractive index distribution of the nanostructured thin films acquired in the current research was studied by the Wemple-Didomenico (WD) model. The dispersion theory is expressed by the following equation in accordance with the effective single-oscillator model of the refractive index (n) in the low absorption region [34]:

$$n^2 = 1 + \frac{E_d E_0}{E_0^2 - (h\upsilon)^2} \quad (7)$$

where n denotes the refractive index, E_o denotes the single oscillator energy for electronic transitions, E_d denotes the dispersion energy for interband optical transitions, and hv denotes the photon energy. The E_d and E_o values of the samples were computed from the slope $(E_dE_o)^{-1}$ and intercept (E_o/E_d) of Fig. 7. The obtained E_o and E_d values show the validity of the single-oscillator model for the nanolayers generated.

It is a known fact that there is a proportion of the polarizability of any solid material to the dielectric constant. This situation is associated with the intensity of the state within the forbidden energy gap. In this regard, it is crucial to investigate the real and imaginary parts of the complex dielectric constant . The definition of the dielectric constant is made as follows: $\varepsilon = \varepsilon_1 - i\varepsilon_2$, i.e. $\varepsilon_1, \varepsilon_2$ are the real and imaginary parts of the complex dielectric constant, respectively. This is expressed by the following equation [35]:

$$\varepsilon_1 = n^2 - k^2 \tag{8}$$

ve

$$\varepsilon_2 = 2nk \tag{9}$$

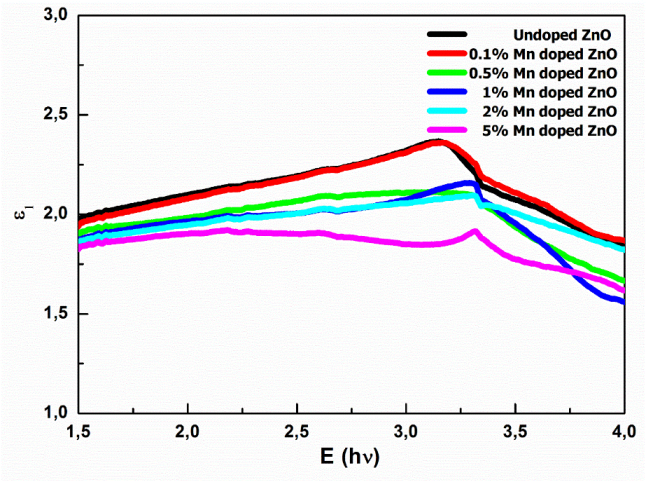

Figure 8. The plots of ε_1-E Mn: ZnO nanolayers.

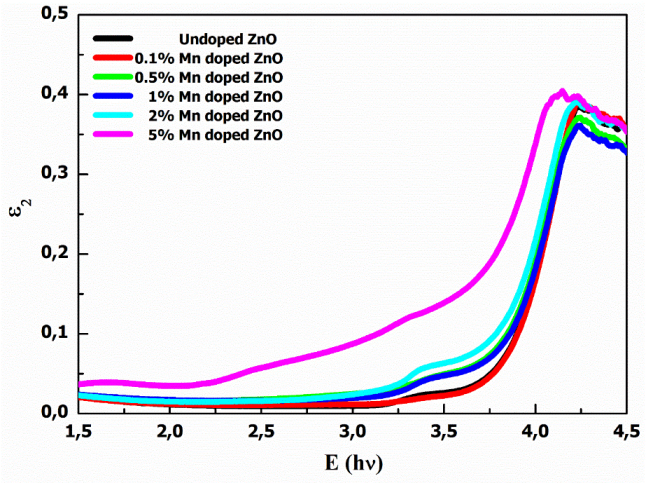

Figure 9. The plots of ε_2-E Mn: ZnO nanolayers

Fig. 8 and Fig. 9 demonstrate the interconnection of the real and imaginary parts of the dielectric constant on the photon energy (hv), respectively. Figs. 8 and 9 showed the real and imaginary dielectric constant changes in the visible region for all nanostructured thin films. With increasing energy, an increase occurs in both the real and imaginary dielectric constant values of the nanolayers. The mentioned increase in optical conductivity is believed to result from electrons excited by photon energy [36]. The graph in Fig. 9 showed a peak reflecting the general band structure. The presence of the mentioned peak results from the photo-excitation process when electrons are excited from the valence band to the conduction band [21]. The real and imaginary dielectric constant of the films changed due to the effect of Mn-doping. Furthermore, the average ε_1 values are observed to be higher than ε_2 in the studied samples. There is an association of the mentioned difference between the real and imaginary parts of optical conductivity with the densities of state (DOS) of the films in the energy band ranges.

14.2. Non-linear optical properties of nanostructured pure and Mn-doped ZnO films

The effect of light on nanomaterials plays an essential role in different optical device applications because of the high non-linear precision. When high radiation intensity occurs in the material, such as laser, it produces non-linear effects such as second ($\chi^{(2)}$) and sensitivity ($\chi^{(3)}$). This is caused by the interaction of induced polarization (P) with the applied electric field (E). These non-linear sensitivities allow us to obtain information about samples that will resist high laser pulses during second and third-order impacts. In the literature, several methods are used to calculate the nonlinear refractive index and optical polarization. However, the ideal equations for thin films are expressed below [37]:

$$p = \chi^{(1)}E + P_{NL} \tag{10}$$

Where;

$$P_{NL} = \chi^{(2)}E^2 + \chi^{(3)}E^3 \tag{11}$$

and $(\chi^{(1)})$ refers to the linear optical susceptibility, and the other parameters are the same as the mentioned above. In the same manner, the linear refractive index $n(\lambda)$ is expressed by the following equation:

$$n(\lambda) = n_0(\lambda) + n_2(E)^2 \tag{12}$$

here $n(\lambda)$ is defined as $n_0(\lambda) >> n_2(\lambda)$, $n(\lambda) = n_0(\lambda)$, and (E^2) denotes the mean square values of the electric field. It is possible to calculate $(\chi^{(1)})$ using the relation presented below:

$$\chi^{(1)} = (n^2 - 1)/4\pi \tag{13}$$

The $(\chi^{(3)})$ value can be calculated as follows:

$$\chi^{(3)} = A[(\chi^{(1)})]^4 \tag{14}$$

Using Eqs. (13) and (14), the following equation is obtained:

$$\chi^{(3)} = \frac{A}{(4\pi)^4}(n_0^2 - 1)^4 \tag{15}$$

where A refers to a constant, and its value is 1.7×10^{-10} esu . It is possible to describe the non-linear refractive index from the relation presented below:

$$n_2 = \frac{12\pi\chi^{(3)}}{n_0} \quad (16)$$

The variations of linear, third-order susceptibilities and nonlinear refractive index with the wavelength of pure and Mn-doped ZnO thin films were demonstrated in Fig. 10, Fig. 11, and Fig. 12, respectively.

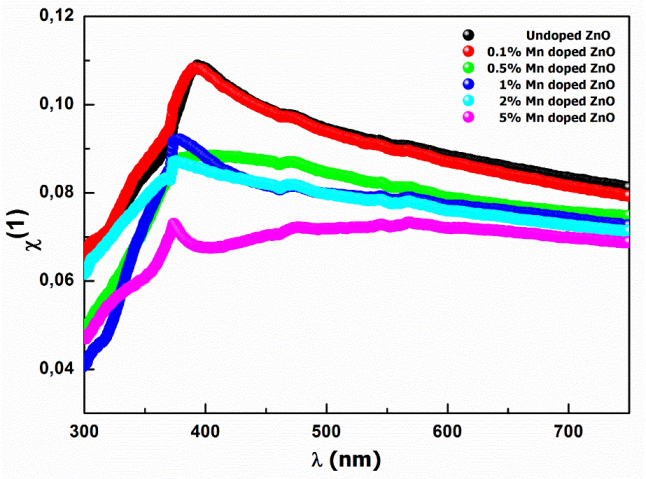

Figure 10. Linear optical susceptibility of the Mn: ZnO nanolayers.

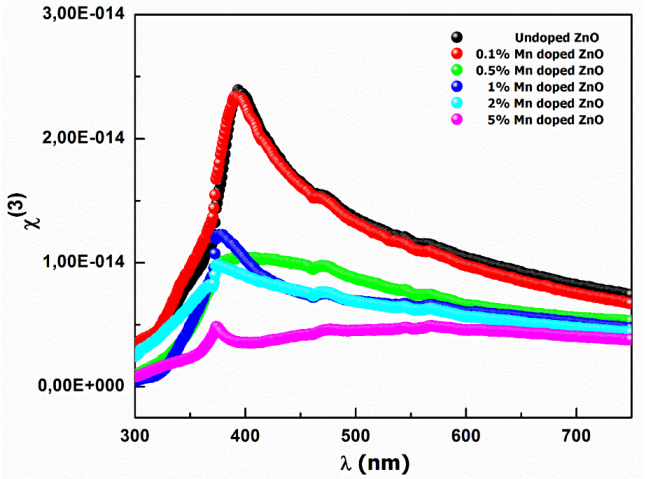

Figure 11. Third-order nonlinear optical susceptibility of the Mn: ZnO nanolayers.

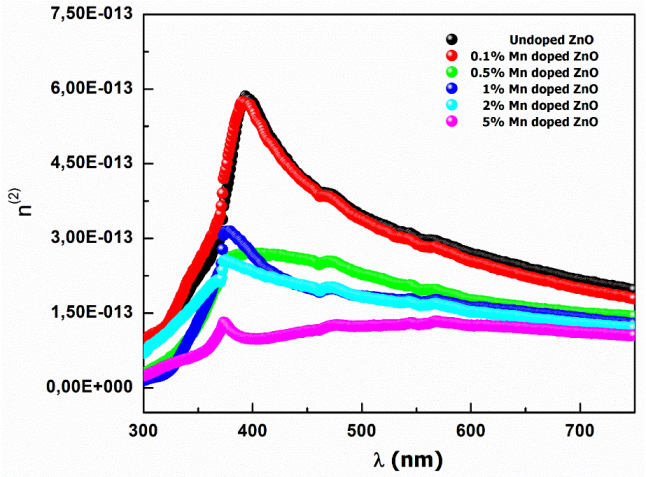

Figure 12. The nonlinear refractive index of the Mn: ZnO nanolayers.

From the obtained graphs, it is clearly seen that linear and non-linear sensitivities increase with wavelength and are saturated at certain wavelengths. This type of behavior is usually due to the regularity of atoms in materials with high levels of crystallization [6]. The behavior in question has been explained by the enhancement in the crystallinity of the pure zinc oxide due to the Mn doping concentration and the high polarization of the doped samples compared to the pure material. Therefore, the susceptibilities of doped samples increase as the level of crystallization increases due to the increased doping concentration. The linear susceptibilities in the current calculations vary between 0.04 and 0.11, while nonlinear susceptibilities vary between 1.05×10^{-14} and 9.41×10^{-15} esu, which demonstrates the impact of doping in ZnO thin films. The calculated optical parameters were compared with previous studies of zinc oxide and results are shown in Table 3.

Table 3. Nonlinear optical parameters of present work on prepared Mn: ZnO nanolayers

Samples	$\chi^{(3)}$ (*esu*)	$n^{(2)}$ (esu)
Pure ZnO	2.41×10^{-14}	5.96×10^{-13}
0.1% Mn doped ZnO	2.32×10^{-14}	5.82×10^{-13}
0.5 % Mn doped ZnO	1.05×10^{-14}	2.73×10^{-13}
1 % Mn doped ZnO	1.25×10^{-14}	3.22×10^{-13}
2 % Mn doped ZnO	9.41×10^{-15}	2.62×10^{-13}
5 % Mn doped ZnO	5.17×10^{-15}	1.36×10^{-13}

These values show that prepared samples are higher than the values of ZnO thin films studied before and Mn has a significant impact on ZnO thin films and gives better results for nonlinear optical applications. Therefore, prepared Mn-doped ZnO thin films in many applications can be used in place of other metal oxide thin films.

15. CONCLUSION

Mn: ZnO thin films were successfully produced with the sol-gel spin coating technique, a simple and effective method. The impact of Mn doping concentration on the optical characteristics was discussed in detail. The optical characteristics of films state that Mn^{2+} ions substitute for the Zn^{2+} ion without altering the wurtzite structure of ZnO. The results indicate that the average values of optical transmission of the samples are greater than 80% and that these materials can be used in optical devices. It was found out that mainly grain size, density, and Mn concentration determine the refractive index of Mn-doped ZnO thin films. The decreasing optical bandgap of the samples with Mn doping is usually caused by the sp-d exchange interaction. All of these cases show that different concentrations of Mn doping cause some levels of impurities or have some effect on the existing levels and thus affect the type of transition. All these data confirm that Mn doping alters both opto-electrical and nonlinear optical properties.

16. REFERENCES

[1] Akcan, D., Gungor, A., Arda, L. (2018). Structural and optical properties of Na-doped ZnO films. Journal of Molecular Structure, 1161: 299–305. doi:10.1016/j.molstruc.2018.02.058

[2] Aydin, H., El-Nasser, H. M., Aydin, C., Al-Ghamdi, A. A., Yakuphanoglu, F. (2015). Synthesis and characterization of nanostructured

undoped and Sn-doped ZnO thin films via sol–gel approach. Applied Surface Science, 350: 109–114. doi:10.1016/j.apsusc.2015.02.189

[3] Aydın, H., Yakuphanoglu, F., Aydın, C. (2019). Al-doped ZnO as a multifunctional nanomaterial: Structural, morphological, optical and low-temperature gas sensing properties. Journal of Alloys and Compounds, 773: 802–811. doi:10.1016/j.jallcom.2018.09.327

[4] Aydın, C., Abd El-sadek, M. S., Zheng, K., Yahia, I. S., Yakuphanoglu, F. (2013). Synthesis, diffused reflectance and electrical properties of nanocrystalline Fe-doped ZnO via sol–gel calcination technique. Optics & Laser Technology, 48: 447–452. doi:10.1016/j.optlastec.2012.11.004

[5] Aydin, C. (2018). The functionalization of morphological, structural and optical properties of Fe doped SnO2 nanocrystals synthesized by the sol–gel method. Journal of Materials Science: Materials in Electronics, 29(23): 20087–20096. doi:10.1007/s10854-018-0140-8

[6] Aydın, C., Benhaliliba, M., Al-Ghamdi, A. A., Gafer, Z. H., El-Tantawy, F., Yakuphanoglu, F. (2013). Determination of optical band gap of ZnO:ZnAl2O4 composite semiconductor nanopowder materials by optical reflectance method. Journal of Electroceramics, 31(1-2): 265–270. doi:10.1007/s10832-013-9829-5

[7] Akcan, D., Ozharar, S., Ozugurlu, E., Arda, L. (2019). The effects of Co/Cu Co-doped ZnO thin films: An optical study. Journal of Alloys and Compounds, 797: 253–261. doi:10.1016/j.jallcom.2019.05.126

[8] Aksoy, S., Caglar, Y. (2019). Synthesis of Mn doped ZnO nanopowders by MW-HTS and its structural, morphological and optical characteristics. Journal of Alloys and Compounds, 781: 929–935. doi:10.1016/j.jallcom.2018.12.101

[9] Aydin, C. (2019). Synthesis of Pd:ZnO nanofibers and their optical characterization dependent on modified morphological properties. Journal of Alloys and Compounds, 777: 145–151. doi:10.1016/j.jallcom.2018.10.325

[10] Aydın, H., Aydın, C., Al-Ghamdi, A. A., Farooq, W. A., Yakuphanoglu, F. (2016). Refractive index dispersion properties of Cr-doped ZnO thin films by sol–gel spin coating method. Optik, 127(4): 1879–1883. doi:10.1016/j.ijleo.2015.10.230

[11] Aydin, H., Gündüz, B., Aydin, C. (2019). Surface morphology, spectroscopy, optical and conductivity properties of transparent poly(9-vinylcarbazole) thin films modified with graphene oxide. Synthetic Metals, 252: 1–7. doi:10.1016/j.synthmet.2019.04.002

[12] Aydin, H., Mansour, S. A., Aydin, C., Al-Ghamdi, A. A., Al-Hartomy, O. A., El-Tantawy, F., Yakuphanoglu, F. (2012). Optical properties of nanostructure boron doped NiO thin films. Journal of Sol-Gel Science and Technology, 64(3): 728–733. doi:10.1007/s10971-012-2909-1

[13] Caglar, M., Ilican, S., Caglar, Y., Yakuphanoglu, F. (2009). Electrical conductivity and optical properties of ZnO nanostructured thin film. Applied Surface Science, 255(8): 4491–4496. doi:10.1016/j.apsusc.2008.11.055

[14] Caglar, Y. (2013). Sol–gel derived nanostructure undoped and cobalt doped ZnO: Structural, optical and electrical studies. Journal of Alloys and Compounds, 560: 181–188. doi:10.1016/j.jallcom.2013.01.080

[15] Caglar, Y., Ilican, S., Caglar, M., Yakuphanoglu, F. (2007). Effects of In, Al and Sn dopants on the structural and optical properties of ZnO thin films. Spectrochimica Acta Part A: Molecular and Biomolecular Spectroscopy, 67(3-4): 1113–1119. doi:10.1016/j.saa.2006.09.035

[16] Shinde, V. R., Gujar, T. P., Lokhande, C. D., Mane, R. S., Han, S.-H. (2006). Mn doped and undoped ZnO films: A comparative structural, optical and electrical properties study. Materials Chemistry and Physics, 96(2-3): 326–330. doi:10.1016/j.matchemphys.2005.07.045

[17] Chaitra, U., Kekuda, D., Mohan Rao, K. (2017). Effect of annealing temperature on the evolution of structural, microstructural, and optical properties of spin coated ZnO thin films. Ceramics International, 43(9): 7115–7122. doi:10.1016/j.ceramint.2017.02.144

[18] Ganesh, V., Salem, G. F., Yahia, I. S., Yakuphanoglu, F. (2017). Synthesis, Optical and Photoluminescence Properties of Cu-Doped Zno Nano-Fibers Thin Films: Nonlinear Optics. Journal of Electronic Materials, 47(3): 1798–1805. doi:10.1007/s11664-017-5950-6

[19] Hu, D., Liu, X., Deng, S., Liu, Y., Feng, Z., Han, B., … Wang, Y. (2014). Structural and optical properties of Mn-doped ZnO nanocrystalline thin films with the different dopant concentrations. Physica E: Low-Dimensional Systems and Nanostructures, 61: 14–22. doi:10.1016/j.physe.2014.03.007

[20] Islam, M. R., Rahman, M., Farhad, S. F. U., Podder, J. (2019). Structural, optical and photocatalysis properties of sol–gel deposited Al-doped ZnO thin films. Surfaces and Interfaces, 16: 120–126. doi:10.1016/j.surfin.2019.05.007

[21] Jacob, A. A., Balakrishnan, L., Meher, S. R., Shambavi, K., Alex, Z. C. (2017). Structural, optical and photodetection characteristics of Cd alloyed ZnO thin film by spin coating. Journal of Alloys and Compounds, 695: 3753–3759. doi:10.1016/j.jallcom.2016.11.265

[22] Karmakar, R., Neogi, S. K., Banerjee, A., Bandyopadhyay, S. (2012). Structural; morphological; optical and magnetic properties of Mn doped ferromagnetic ZnO thin film. Applied Surface Science, 263: 671–677. doi:10.1016/j.apsusc.2012.09.133

[23] Kaur, G., Mitra, A., Yadav, K. L. (2015). Pulsed laser deposited Al-doped ZnO thin films for optical applications. Progress in Natural Science: Materials International, 25(1): 12–21. doi:10.1016/j.pnsc.2015.01.012

[24] Mia, M. N. H., Pervez, M. F., Hossain, M. K., Reefaz Rahman, M., Uddin, M. J., Al Mashud, M. A., … Hoq, M. (2017). Influence of Mg content on tailoring optical bandgap of Mg-doped ZnO thin film prepared by sol-gel method. Results in Physics, 7: 2683–2691. doi:10.1016/j.rinp.2017.07.047

[25] Sankar Ganesh, R., Durgadevi, E., Navaneethan, M., Patil, V. L., Ponnusamy, S., Muthamizhchelvan, C., … Hayakawa, Y. (2017). Low temperature ammonia gas sensor based on Mn-doped ZnO nanoparticle decorated microspheres. Journal of Alloys and Compounds, 721: 182–190. doi:10.1016/j.jallcom.2017.05.315

[26] Aydin, H. (2014). Electrical and Optical Properties of Titanium Dioxide-Carbon Nanotube Nanocomposites. Journal of Nanoelectronics and Optoelectronics, 9(5): 608–613. doi:10.1166/jno.2014.1642

[27] Shukla, P., Tiwari, S., Joshi, S. R., Akshay, V. R., Vasundhara, M., Varma, S., … Chanda, A. (2018). Investigation on structural, morphological and optical properties of Co-doped ZnO thin films. Physica B: Condensed Matter, 550: 303–310. doi:10.1016/j.physb.2018.08.046

[28] Sindhu, H. S., Maidur, S. R., Patil, P. S., Choudhary, R. J., Rajendra, B. V. (2019). Nonlinear optical and optical power limiting studies of Zn1-xMnxO thin films prepared by spray pyrolysis. Optik, 182: 671–681. doi:10.1016/j.ijleo.2019.01.031

[29] Singh, P., Kaushal, A., Kaur, D. (2009). Mn-doped ZnO nanocrystalline thin films prepared by ultrasonic spray pyrolysis. Journal of Alloys and Compounds, 471(1-2): 11–15. doi:10.1016/j.jallcom.2008.03.123

[30] Sivalingam, D., Gopalakrishnan, J. B., Rayappan, J. B. B. (2012). Structural, morphological, electrical and vapour sensing properties of Mn doped nanostructured ZnO thin films. Sensors and Actuators B: Chemical, 166-167, 624–631. doi:10.1016/j.snb.2012.03.023

[31] Srinivasan, G., Kumar, J. (2008). Effect of Mn doping on the microstructures and optical properties of sol–gel derived ZnO thin films. Journal of Crystal Growth, 310(7-9): 1841–1846. doi:10.1016/j.jcrysgro.2007.10.056

[32] Ton-That, C., Foley, M., Phillips, M. R., Tsuzuki, T., Smith, Z. (2012). Correlation between the structural and optical properties of Mn-doped ZnO nanoparticles. Journal of Alloys and Compounds, 522: 114–117. doi:10.1016/j.jallcom.2012.01.116

[33] Vijayaprasath, G., Murugan, R., Ravi, G., Mahalingam, T., Hayakawa, Y. (2014). Characterization of dilute magnetic semiconducting transition metal doped ZnO thin films by sol–gel spin coating method. Applied Surface Science, 313: 870–876. doi:10.1016/j.apsusc.2014.06.093

[34] Xin, M., Hu, L. Z., Liu, D.-P., Yu, N.-S. (2014). Effect of Mn doping on the optical, structural and photoluminescence properties of nanostructured ZnO thin film synthesized by sol–gel technique. Superlattices and Microstructures, 74: 234–241. doi:10.1016/j.spmi.2014.06.009

[35] Yang, S., Zhang, Y. (2013). Structural, optical and magnetic properties of Mn-doped ZnO thin films prepared by sol–gel method. Journal of Magnetism and Magnetic Materials, 334: 52–58. doi:10.1016/j.jmmm.2013.01.026

[36] Zhong, J. bo, Li, J. zhang, He, X. yang, Zeng, J., Lu, Y., Hu, W., Lin, K. (2012). Improved photocatalytic performance of Pd-doped ZnO. Current Applied Physics, 12(3): 998–1001. doi:10.1016/j.cap.2012.01.003

[37] Jilani, A., Abdel-wahab, M. S., Al-ghamdi Attieh A., Dahlan, A. sadik, Yahia, I. S. (2016). Nonlinear optical parameters of nanocrystalline AZO thin film measured at different substrate temperatures. Physica B: Condensed Matter, 481: 97–103. doi:10.1016/j.physb.2015.10.038

EUROPEAN MECHANICAL SCIENCE

Instructions for authors

All manuscripts must be in English. Pages should be numbered sequentially. The manuscript should be composed in accordance with the Article Template given above. The maximum length of contributions is 10 pages. For full instructions see the Information for Authors section on the journal's website:

http://dergipark.gov.tr/ems/page/2805

FORMAT OF THE MANUSCRIPT

The manuscript should be composed in accordance with the Article Template.

The manuscript should be written in the following format:

- A Title that adequately describes the content of the manuscript.

- A list of Authors and their affiliations.

- An Abstract that should not exceed 550 words. The Abstract should state the principal objectives and the scope of the investigation, as well as the methodology employed. It should summarize the results and state the principal conclusions.

- 4-6 significant key words should follow the abstract to aid indexing.

- An Introduction that should provide a review of recent literature and sufficient background information to allow the results of the article to be understood and evaluated.

- An Experimental section that should provide details of the experimental set-up and the methods used to obtain the results.

- A Results section that should clearly and concisely present the data, using figures and tables where appropriate.

- A Discussion section that should describe the relationships and generalizations shown by the results and discuss the significance of the results, making comparisons with previously published work. (It may be appropriate to combine the Results and Discussion sections into a single section to improve clarity.)

- A Conclusions section that should present one or more conclusions drawn from the results and subsequent discussion and should not duplicate the Abstract.

- Acknowledgement (optional) of collaboration or preparation assistance may be included. Please note the source of funding for the research.

- References must be cited consecutively in the text using square brackets [1] and collected together in a reference list at the end of the manuscript.

FIGURES

Figures (figures, graphs, illustrations digital images, photographs) must be cited in consecutive numerical order in the text and referred to in both the text and the captions as Figure 1, Figure 2, etc. Figures should be prepared without borders and on white grounding and should be sent separately in their original formats. If a figure is composed of several parts, please mark each part with a), b), c), etc. and provide an explanation for each part in Figure caption. The caption should be self-explanatory. Letters and numbers should be readable (Arial or Times New Roman, min 6 pt with equal sizes and fonts in all figures).

Graphics (submitted as supplementary files) may be exported in resolution good enough for printing (min. 300 dpi) in any common format, e.g. TIFF, BMP, GIF or JPG, PDF and should be named Fig1.jpg, Fig2.tif, etc. However, graphs and line drawings should be prepared as vector images, e.g. CDR, AI.

Multi-curve graphs should have individual curves marked with a symbol or otherwise provide distinguishing differences using, for example, different thicknesses or dashing.

TABLES

Tables should carry separate titles and must be numbered in consecutive numerical order in the text and referred to in both the text and the captions as Table 1, Table 2, etc. In addition to the physical quantities, such as t (in italics), the units (normal text) should be added in square brackets. Tables should not duplicate data found elsewhere in the manuscript. Tables should be prepared using a table editor and not inserted as a graphic.

RERERENCES

A reference list must be included using the following information as a guide. Only cited text references are to be included. Each reference is to be referred to in the text by a number enclosed in a square bracket (i.e. [3] or [2] to [4] for more references; do not combine more than 3 references, explain each).

References must be numbered and ordered according to where they are first mentioned in the paper, not alphabetically. All references must be complete and accurate. Please add DOI code when available. Examples follow.

Journal Papers:

Surname 1, Initials, Surname 2, Initials (year). Title. Journal, volume, number, pages, DOI code.

[1] Calikoz, R., Ozcanli, B., Serin, F., (2017). Simulating nonlinear materials under vertical forces by using intelligent . European Mechanical Science, 57(8): 531-538, DOI:10.5545/ems.2017.013.

Journal titles should not be abbreviated. Note that journal title is set in italics.

Books: Surname 1, Initials, Surname 2, Initials (year). Title. Publisher, place of publication.

[2] Ozgur, M.P. (2012). Fundamentals of Mechanical Engineering. Gunlubey, Ankara.

Chapters in Books:

Surname 1, Initials, Surname 2, Initials (year). Chapter title. Editor(s) of book, book title. Publisher, place of publication, pages.

[3] Akarca, G., Gelidor, M. (2016). Mechanical robotic systems. Calikca, V., Kurbetoglu, A., Merdan, M. (Eds.), Cutting Edge Robotics. Literatur Bergli, Mammendorf, 553-576.

Proceedings Papers:

Surname 1, Initials, Surname 2, Initials (year). Paper title. Proceedings title, pages.

[4] Seferci, N., Malikoglu, S., Tosun, N. (2009). Applied mechanic in process industry. IMSEC 2016 Conference Proceedings, 422-427.